

SUMMARY REPORT FOR THE HERA - LHC WORKSHOP PROCEEDINGS WORKING GROUP I: PARTON DISTRIBUTIONS

CONVENERS:

*M. Dittmar*¹, *S. Forte*², *A. Glazov*³, *S. Moch*⁴

CONTRIBUTING AUTHORS:

G. Altarelli^{5,6}, *J. Anderson*⁷, *R. D. Ball*⁸, *G. Beuf*⁹, *M. Boonekamp*¹⁰, *H. Burkhardt*¹¹, *F. Caola*²,
*M. Ciafaloni*¹², *D. Colferai*¹², *A. Cooper-Sarkar*¹³, *A. de Roeck*¹⁴, *L. Del Debbio*⁸, *J. Feltesse*^{15,16}, *F. Gelis*⁵,
*J. Grebenyuk*³, *A. Guffanti*¹⁷, *V. Halyo*¹⁸, *J. I. Latorre*¹⁹, *V. Lendermann*²⁰, *G. Li*²¹, *L. Motyka*^{22,23},
*T. Petersen*¹⁴, *A. Piccione*², *V. Radescu*³, *M. Rogal*⁴, *J. Rojo*^{2,24}, *C. Royon*¹⁰, *G. P. Salam*²⁴, *D. Šálek*²⁵,
A. M. Stašo^{26,27,28}, *R. S. Thorne*²⁹, *M. Ubiali*⁸, *J. A. M. Vermaseren*³⁰, *A. Vogt*³¹, *G. Watt*²⁹, *C. D. White*³⁰

¹ Institute for Particle Physics, ETH-Zürich Höggerberg, CH 8093 Zürich, Switzerland

² Dipartimento di Fisica, Università di Milano, INFN Sezione di Milano, Via Celoria 16, I-20133 Milan, Italy

³ DESY, Notkestrasse 85, D-22603 Hamburg, Germany

⁴ DESY, Platanenallee 6, D-15738 Zeuthen, Germany

⁵ CERN, Department of Physics, Theory Division, CH-1211 Geneva 23, Switzerland

⁶ Dipartimento di Fisica "E. Amaldi", Università Roma Tre and INFN, Sezione di Roma Tre, via della Vasca Navale 84, I-00146 Rome, Italy

⁷ School of Physics, University College Dublin, Ireland

⁸ School of Physics, University of Edinburgh, Edinburgh EH9 3JZ, UK

⁹ Institut de Physique Théorique, CEA-Saclay F-91191 Gif-sur-Yvette, France

¹⁰ IRFU, Service de Physique des Particules, CEA-Saclay F-91191 Gif-sur-Yvette, France

¹¹ CERN-AB, CH-1211 Geneva 23, Switzerland

¹² Dipartimento di Fisica, Università di Firenze and INFN, Sezione di Firenze, I-50019 Sesto Fiorentino, Italy

¹³ Department of Physics, Nuclear and Astrophysics Lab., Keble Road, Oxford, OX1 3RH, UK

¹⁴ CERN-PH, CH-1211 Geneva 23, Switzerland

¹⁵ IRFU, CEA-Saclay F-91191 Gif-sur-Yvette, France

¹⁶ University of Hamburg, Luruper Chaussee 149, Hamburg, D-22761 Germany

¹⁷ Physikalisches Institut, Albert-Ludwigs-Universität Freiburg, Hermann-Herder-Straße 3, D-79104 Freiburg i. B., Germany

¹⁸ Department of Physics, Princeton University, Princeton, NJ08544, USA

¹⁹ Departament d'Estructura i Constituents de la Matèria, Universitat de Barcelona, Diagonal 647, E 08028 Barcelona, Spain

²⁰ Kirchhoff-Institut für Physik, Universität Heidelberg, Im Neuenheimer Feld 227, D-69120 Heidelberg, Germany

²¹ Laboratoire de l'Accélérateur Linéaire, Université Paris-Sud, Orsay, France

²² II Institute for Theoretical Physics, University of Hamburg, Luruper Chaussee 149, Hamburg, D-22761 Germany

²³ Institute of Physics, Jagellonian University Reymonta 4, 30-059 Cracow, Poland

²⁴ LPTHE, UPMC – Paris 6, Paris-Diderot – Paris 7, CNRS UMR 7589, F-75005 Paris, France

²⁵ Institute of Particle and Nuclear Physics, Charles University, Prague, Czech Republic

²⁶ Physics Department, Penn State University, 104 Davey Laboratory, University Park, PA 16802, USA

²⁷ H. Niewodniczański Institute of Nuclear Physics, Polish Academy of Science, ul.Radzikowskiego 152, 31-342 Cracow, Poland

²⁸ Brookhaven National Laboratory, Upton, NY-11073, USA

²⁹ Department of Physics and Astronomy, University College, London, WC1E 6BT, UK

³⁰ NIKHEF Theory Group, Kruislaan 409, NL 1098 SJ Amsterdam, The Netherlands

³¹ Department of Mathematical Sciences, University of Liverpool, Liverpool, L69 3BX, UK

Abstract

We provide an assessment of the state of the art in various issues related to experimental measurements, phenomenological methods and theoretical results relevant for the determination of parton distribution functions (PDFs) and their uncertainties, with the specific aim of providing benchmarks of different existing approaches and results in view of their application to physics at the LHC.

We discuss higher order corrections, we review and compare different approaches to small x resummation, and we assess the possible relevance of parton saturation in the determination of PDFs at HERA and its possible study in LHC processes. We provide various benchmarks of PDF fits, with the specific aim of studying issues of error propagation, non-gaussian uncertainties, choice of functional forms of PDFs, and combination of data from different experiments and different processes. We study the impact of combined HERA (ZEUS-H1) structure function data, their impact on PDF uncertainties, and their implications for the computation of standard candle processes, and we review the recent F_L determination at HERA. Finally, we compare and assess methods for luminosity measurements at the LHC and the impact of PDFs on them.

Contents

1	INTRODUCTION	6
2	THEORETICAL ISSUES	7
2.1	Precision calculations for inclusive DIS: an update ¹	7
2.2	Small x resummation ²	10
2.2.1	The Altarelli-Ball-Forte (ABF) Approach	11
2.2.2	The Ciafaloni-Colferai-Salam-Stasto (CCSS) Approach	15
2.2.3	The Thorne-White (TW) Approach	17
2.2.4	Resummed structure functions: comparison of the ABF and TW approaches	21
2.2.5	Conclusion	23
2.3	Parton saturation and geometric scaling ³	23
2.3.1	Introduction ⁴	23
2.3.2	Phenomenology ⁵	26
2.3.3	Geometric scaling and evolution equations with saturation ⁶	28
2.3.4	DGLAP evolution and the saturation boundary conditions ⁷	29
2.3.5	Geometric scaling from DGLAP evolution ⁸	30
2.3.6	Saturation model and higher twists ⁹	31
2.3.7	Conclusions	34
3	BENCHMARKING OF PARTON DISTRIBUTIONS AND THEIR UNCERTAINTIES¹⁰	36
3.1	Introduction	36
3.1.1	Settings for the H1 benchmark	36
3.1.2	Settings for the HERA–LHC benchmark	38
3.2	Experimental Error Propagation ¹¹	39
3.2.1	Introduction	39
3.2.2	Method	39
3.2.3	Validation of the Method	41
3.2.4	Test of various assumptions for the error distributions	41
3.2.5	Conclusions	41
3.3	HERA–LHC Benchmark	41
3.3.1	MSTW approach ¹²	42
3.3.2	NNPDF approach ¹³	43

¹Contributing authors: S. Moch, M. Rogal, J. A. M. Vermaseren, A. Vogt

²Contributing authors: G. Altarelli, R. D. Ball, M. Ciafaloni, D. Colferai, G. P. Salam, A. Stařto, R. S. Thorne, C. D. White

³Contributing authors: G. Beuf, F. Caola, F. Gelis, L. Motyka, C. Royon, D. řálek, A. M. Stařto

⁴Contributing authors: F. Gelis, A. M. Stařto

⁵Contributing authors: C. Royon, D. řálek

⁶Contributing author: G. Beuf

⁷Contributing author: A. M. Stařto

⁸Contributing author: F. Caola

⁹Contributing author: L. Motyka

¹⁰Contributing authors: R. D. Ball, L. Del Debbio, J. Feltesse, S. Forte, A. Glazov, A. Guffanti, J. I. Latorre, A. Piccione, V. Radescu, J. Rojo, R. S. Thorne, M. Ubiali, G. Watt

¹¹Contributing authors: J. Feltesse, A. Glazov, V. Radescu

¹²Contributing authors: R. S. Thorne, G. Watt

¹³Contributing authors: R. D. Ball, L. Del Debbio, S. Forte, A. Guffanti, J. I. Latorre, A. Piccione, J. Rojo, M. Ubiali

3.3.3	Comparison between the Benchmark Parton Distributions	44
3.3.4	Comparison of the Benchmark Parton Distributions and Global Fits	46
3.4	H1 Benchmark	48
3.4.1	NNPDF analysis ¹⁴	49
3.4.2	Comparison between the Benchmark Parton Distributions	51
4	DETERMINATION OF PARTON DISTRIBUTIONS	52
4.1	Extraction of the proton PDFs from a combined fit of H1 and ZEUS inclusive DIS cross sections ¹⁵	52
4.1.1	Introduction	52
4.1.2	Data Combination	53
4.1.3	QCD Analysis	54
4.1.4	Results	56
4.1.5	Summary of HERAPDF0.1 results	61
4.1.6	Predictions for W and Z cross-sections at the LHC using the HERAPDF0.1	62
4.2	Measurements of the Proton Structure Function F_L at HERA ¹⁶	66
4.2.1	Introduction	66
4.2.2	Indirect F_L Extraction by H1	67
4.2.3	Details of Direct F_L Measurements	69
4.2.4	Measurements of $F_L(x, Q^2)$ by H1 and ZEUS	73
4.2.5	Summary	74
5	PROTON-PROTON LUMINOSITY, STANDARD CANDLES AND PDFS AT THE LHC¹⁷	76
5.1	Introduction	76
5.2	Luminosity relevant design of ATLAS/CMS and LHCb	77
5.2.1	Lepton triggering and W/Z identification.	78
5.3	Direct and indirect absolute pp luminosity measurements	79
5.3.1	Proton-proton luminosity from machine parameters ¹⁸	79
5.3.2	Direct measurements of the absolute luminosity at LHCb	81
5.3.3	Absolute pp luminosity from specialized detectors and from the total cross section measurement	81
5.3.4	Real time relative luminosity measurements	82
5.3.5	Proton-proton luminosity from the reaction $pp \rightarrow pp\mu\mu$	82
5.4	Indirect and relative pp luminosity measurements	83
5.4.1	Using the reaction $pp \rightarrow Z \rightarrow \ell^+\ell^-$ to measure L_{pp}	84
5.4.2	Measuring Z and W production, experimental approaches in ATLAS	84
5.4.3	Measuring Z production, experimental approach in LHCb	85
5.4.4	PDF and relative parton-parton luminosity measurements	86
5.5	Comparing the different pp luminosity measurements	86
5.5.1	Which luminosity accuracy might be achievable and when	88

¹⁴Contributing authors R. D. Ball, L. Del Debbio, S. Forte, A. Guffanti, J. I. Latorre, A. Piccione, J. Rojo, M. Ubiali

¹⁵Contributing authors: A. Cooper-Sarkar, A. Glazov, G. Li for the H1-ZEUS combination group.

¹⁶Contributing authors: J. Grebenyuk, V. Lendermann

¹⁷Contributing authors: J. Anderson, M. Boonekamp, H. Burkhardt, M. Dittmar, V. Halyo, T. Petersen

¹⁸Contributing author: H. Burkhardt

5.6 Summary and Outlook 88

6 OUTLOOK: THE PDF4LHC INITIATIVE¹⁹ 90

¹⁹Contributing author: A. de Roeck

1 INTRODUCTION

With the start of data-taking at the LHC getting closer, the importance of a detailed understanding of the physics of parton distributions (PDFs) has increased considerably, along with the awareness of the LHC community for the importance of the issues related to it. Clearly, the main reason why PDFs are important at the LHC is that at a hadron collider a detailed understanding of PDFs is needed in order to obtain accurate predictions for both signal and background processes. Indeed, for many physical processes at the LHC, PDFs are the dominant source of uncertainty. On the other hand, an accurate control of PDF uncertainties allows one to use selected processes as “standard candles”, for instance in the determination of luminosities. However, this also means that experimentation at the LHC will provide a considerable amount of new experimental information on PDFs, and it will enable us to test the adequacy of their current theoretical understanding.

The main aim of this document is to provide a state of the art assessment of our understanding of PDFs at the dawn of the LHC. Since the previous HERA-LHC workshop [1], we have witnessed several important directions of progress in the physics of PDFs. On the theoretical side there has been conclusive progress in extending the treatment of perturbative QCD beyond the current default, namely, the next-to-leading perturbative order. On the phenomenological side there has been a joint effort between experimental and theoretical groups involved in the extraction of PDFs, specifically from global fits, in agreeing on common procedures, benchmarks and standards. On the experimental side, new improved results from the HERA runs are being finalized: these include both the construction of a joint determination of structure function which combines the result of the ZEUS and H1 experiments, and the first direct measurements of the structure function F_L which have been made possible by running HERA at a reduced proton beam energy in 2007. Also, the LHC experiments (ATLAS, CMS and LHCb) are now assessing the use of standard candle processes for luminosity measurements.

All these issues are discussed in this document. In each case, our main goal has been to provide as much as possible a joint treatment by the various groups involved, as well as a comparison of different approaches and benchmarking of results. In particular, in Sect. 2, after briefly reviewing (Sect. 2.1) the current status of higher-order calculations for DIS, we provide (Sect. 2.2) detailed comparisons of techniques and results of different existing approaches to small x resummation, and then we summarize (Sect. 2.3) the current status of studies of parton saturation at HERA, their possible impact on current PDF extraction and the prospects of future studies at the LHC. In Sect. 3 we discuss methods and results for the benchmarking of PDF fits: with specific reference to two benchmark fits based on a common agreed set of data, we discuss issues related to error propagation and non-gaussian errors, to the choice of functional form and corresponding bias, to possible incompatibilities between different data sets. In Sect. 4 we turn to recent progress in the extraction of PDFs from HERA data, specifically the impact of combined ZEUS-H1 structure function data on PDF determination and the ensuing calculation of W and Z cross-sections (Sect. 4.1) and the recent first determination of the structure function F_L (Sect. 4.2). In Sect. 5 we discuss and compare luminosity measurements based on absolute proton-proton luminosity measurements to those based on the use of standard candle processes, and the impact on all of them of PDF uncertainties. Finally, in Sect. 6 we present the PDF4LHC initiative, which will provide a framework for the continuation of PDF studies for the LHC.

Note: Most of the contributions to this workshop are the result of collaboration between various groups. The common set of authors given for each section or subsection has read and approved the entire content of that section or subsection; however, when a subset of these authors is given for a specific part of the section or subsection, they are responsible for it.

2 THEORETICAL ISSUES

2.1 Precision calculations for inclusive DIS: an update²⁰

With high-precision data from HERA and in view of the outstanding importance of hard scattering cross sections at the LHC, a quantitative understanding of deep-inelastic processes is indispensable, necessitating calculations beyond the standard next-to-leading order of perturbative QCD.

In this contribution we briefly discuss the recent extension of the three-loop calculations for inclusive deep-inelastic scattering (DIS) [2–9] to the complete set of coefficient functions for the charged-current (CC) case. The new third-order expressions are too lengthy for this short overview. They can be found in Refs. [10, 11] together with the calculational methods and a more detailed discussion. Furthermore the reader is referred to Refs. [12, 13] for our first results on the three-loop splitting functions for the evolution of helicity-dependent parton distributions.

Structure functions in inclusive deep-inelastic scattering are among the most extensively measured observables. The combined data from fixed-target experiments and the HERA collider spans about four orders of magnitude in both Bjorken- x variable and the scale $Q^2 = -q^2$ given by the momentum q of the exchanged electroweak gauge boson [14]. Here we consider the W -exchange charged-current case, see Refs. [15–21] for recent data from neutrino DIS and HERA. With six structure functions, $F_2^{W^\pm}$, $F_3^{W^\pm}$ and $F_L^{W^\pm}$, this case has a far richer structure than, for example, electromagnetic DIS with only two independent observables, F_2 and F_L .

Even taking into account a forthcoming combined H1/ZEUS final high- Q^2 data set from HERA, more detailed measurements are required to fully exploit the resulting potential, for instance at a future neutrino factory, see Ref. [22], and the LHeC, the proposed high-luminosity electron-proton collider at the LHC [23]. Already now, however, CC DIS provides important information on the parton structure of the proton, e.g., its flavour decomposition and the valence-quark distributions. Moreover, present results are also sensitive to electroweak parameters of the Standard Model such as $\sin^2 \theta_W$, see Ref. [24], and the space-like W -boson propagator [25]. As discussed, for example, in Refs. [26–29], a reliable determination of $\sin^2 \theta_W$ from neutrino DIS requires a detailed understanding of non-perturbative and perturbative QCD effects.

Previous complete results on unpolarized DIS include the three-loop splitting functions [5, 6] as well as the 3-loop coefficient functions for the photon-exchange structure functions $F_{2,L}$ [7, 8]. However, most coefficient functions for CC DIS were not fully computed to three loops so far.

For this case it is convenient to consider linear combinations of the structure functions $F_a^{W^\pm}$ with simple properties under crossing, such as $F_a^{\nu p \pm \bar{\nu} p}$ ($a = 2, 3, L$) for neutrino DIS. For all these combinations either the even or odd moments can be calculated in Mellin- N space in the framework of the operator product expansion (OPE), see Ref. [30]. The results for the third-order coefficient functions for the even- N combinations $F_{2,L}^{\nu p + \bar{\nu} p}$ can be taken over from electromagnetic DIS [7, 8]. Also the coefficient function for the odd- N based charged-current structure function $F_3^{\nu p + \bar{\nu} p}$ is completely known at three-loop accuracy, with the results only published via compact parameterizations so far [9]. For the remaining combinations $F_{2,L}^{\nu p - \bar{\nu} p}$ and $F_3^{\nu p - \bar{\nu} p}$, on the other hand, only recently the first six odd or even integer moments of the respective coefficient functions have been calculated to third order in Ref. [10] following the approach of Refs. [2–4] based on the MINCER program [31, 32].

The complete results of Refs. [7–9] fix all even and odd moments N . Hence already the present knowledge of fixed Mellin moments for $F_{2,L}^{\nu p - \bar{\nu} p}$ and $F_3^{\nu p - \bar{\nu} p}$ is sufficient to determine also the lowest six moments of the differences of corresponding even- N and odd- N coefficient functions and to address a theoretical conjecture [33] for these quantities, see Ref. [11]. Furthermore these moments facilitate x -space approximations in the style of, e.g. Ref. [34] which are sufficient for most phenomenological purposes, including the determination of the third-order QCD corrections to the Paschos-Wolfenstein relation [35] used for the extraction of $\sin^2 \theta_W$ from neutrino DIS.

The even-odd differences of the CC coefficient functions C_a for $a = 2, 3, L$ can be defined by

$$\delta C_{2,L} = C_{2,L}^{\nu p + \bar{\nu} p} - C_{2,L}^{\nu p - \bar{\nu} p}, \quad \delta C_3 = C_3^{\nu p - \bar{\nu} p} - C_3^{\nu p + \bar{\nu} p}. \quad (1)$$

²⁰Contributing authors: S. Moch, M. Rogal, J. A. M. Vermaseren, A. Vogt

The signs are chosen such that the differences are always ‘even – odd’ in the moments N accessible by the OPE [30], and it is understood that the $d^{abc}d_{abc}$ part of $C_3^{\nu p + \bar{\nu} p}$ [4, 9] is removed before the difference is formed. With $a_s = \alpha_s/(4\pi)$ these non-singlet quantities can be expanded as

$$\delta C_a = \sum_{l=2} a_s^l \delta c_a^{(l)}. \quad (2)$$

There are no first-order contributions to these differences, hence the above sums start at $l = 2$.

We start the illustration of these recent results by looking at the approximations for the $\nu p - \bar{\nu} p$ odd- N coefficient functions $c_{2,L}^{(3)}(x)$ (see Ref. [11] for a detailed discussion). These are compared in Fig. 1 to their exact counterparts [7, 8] for the even- N non-singlet structure functions. The dashed lines represent the uncertainty band due to the limited number of known moments. The third-order even-odd differences remain noticeable to larger values of x than at two loops, e.g., up to $x \simeq 0.3$ for F_2 and $x \simeq 0.6$ for F_L for the four-flavour case shown in the figure. The moments $N = 1, 3, \dots, 9$ constrain $\delta c_{2,L}^{(3)}(x)$ very well at $x \gtrsim 0.1$, and approximately down to $x \approx 10^{-2}$.

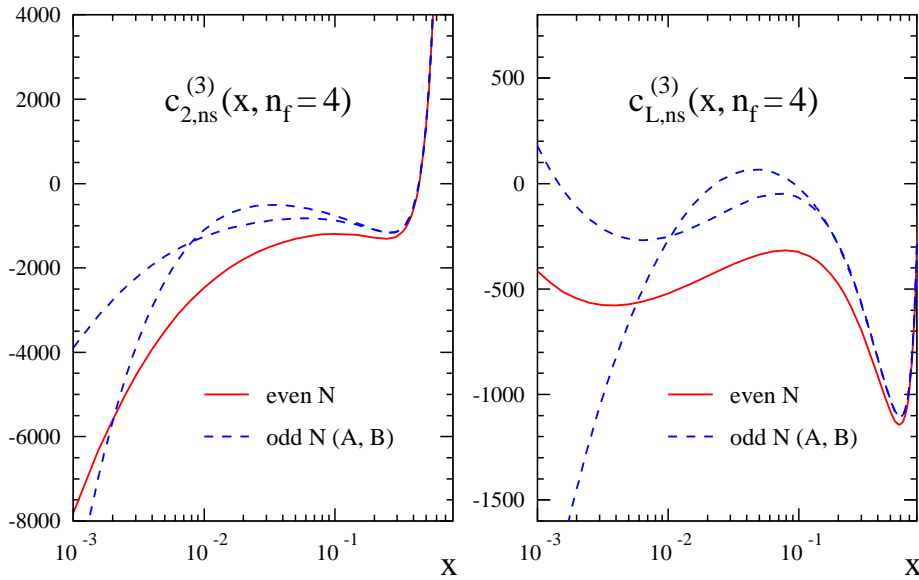


Fig. 1: The exact third-order coefficient functions of the even- N structure functions $F_{2,L}^{\nu p + \bar{\nu} p}$ for four massless flavours, and the approximate odd-moment quantities for $\nu p - \bar{\nu} p$ combination.

Concerning low values of Bjorken- x one should recall that the uncertainty bands shown by the dashed lines in Fig. 1 do not directly indicate the range of applicability of these approximations, since the coefficient functions enter observables only via smoothening Mellin convolutions with non-perturbative initial distributions. In Fig. 2 we therefore present the convolutions of all six third-order CC coefficient functions with a characteristic reference distribution. It turns out that the approximations of the previous figure can be sufficient down to values even below $x = 10^{-3}$, which is amply sufficient for foreseeable applications to data. The uncertainty of $\delta c_3^{(3)}(x)$, on the other hand, becomes relevant already at larger values, $x \lesssim 10^{-2}$, as the lowest calculated moment of this quantity, $N = 2$, has far less sensitivity to the behaviour at low x .

The three-loop corrections to the non-singlet structure functions are rather small even well below the x -values shown in the figure – recall our small expansion parameter a_s : the third-order coefficient are smaller by a factor $2.0 \cdot 10^{-3}$ if the expansion is written in powers of α_s . Their sharp rise for $x \rightarrow 1$ is understood in terms of soft-gluon effects which can be effectively resummed, if required, to next-to-next-to-next-to-leading logarithmic accuracy [36]. Our even-odd differences $\delta c_a^{(3)}(x)$, on the other hand, are irrelevant at $x > 0.1$ but have a sizeable impact at smaller x in particular on the corrections for F_2 and F_L . The approximate results for $\delta c_a^{(3)}(x)$ facilitate a first assessment of the perturbative stability of the even-odd differences (1). In Fig. 3 we

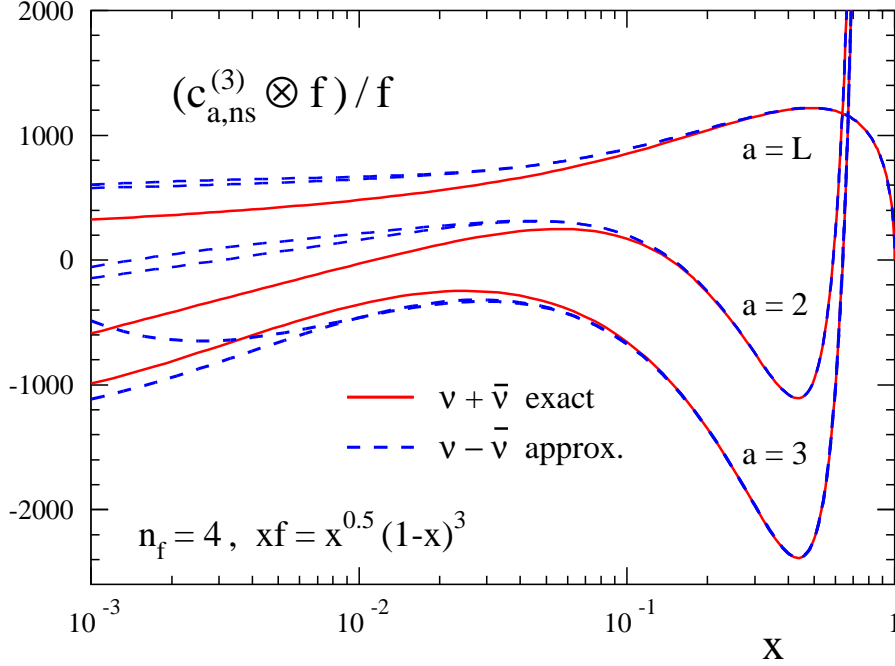


Fig. 2: Convolution of the six third-order CC coefficient functions for $F_{2,3,L}$ in $\nu p + \bar{\nu} p$ and $\nu p - \bar{\nu} p$ DIS with a schematic but typical non-singlet distribution f . All results have been normalized to $f(x)$, suppressing the large but trivial variation of the absolute convolutions.

illustrate the known two orders for F_2 and F_L for $\alpha_s = 0.25$ and $n_f = 4$ massless quark flavours, employing the same reference quark distribution as in Fig. 2.

Obviously our new α_s^3 corrections are important wherever these coefficient-function differences are non-negligible. On the other hand, our results confirm that these quantities are very small, and thus relevant only when a high accuracy is required. These conditions are fulfilled for the calculation of QCD corrections for the so-called Paschos-Wolfenstein relation. This relation is defined in terms of a ratio of neutral-current and charged-current cross sections for neutrino-nucleon DIS [35],

$$R^- = \frac{\sigma(\nu_\mu N \rightarrow \nu_\mu X) - \sigma(\bar{\nu}_\mu N \rightarrow \bar{\nu}_\mu X)}{\sigma(\nu_\mu N \rightarrow \mu^- X) - \sigma(\bar{\nu}_\mu N \rightarrow \mu^+ X)}. \quad (3)$$

The asymmetry R^- directly measures $\sin^2 \theta_W$ if the up and down valence quarks in the target carry equal momenta, and if the strange and heavy-quark sea distributions are charge symmetric. Beyond the leading order this asymmetry can be presented as an expansion in α_s and inverse powers of the dominant isoscalar combination $u^- + d^-$, where $q^- = \int_0^1 dx x (q(x) - \bar{q}(x))$ is the second Mellin moment of the valence quark distributions. Using the results for differences $\delta c_a^{(3)}(x)$, $a = 2, L, 3$ one can present it in a numeric form,

$$R^- = \frac{1}{2} - \sin^2 \theta_W + \frac{u^- - d^- + c^- - s^-}{u^- + d^-} \left\{ 1 - \frac{7}{3} \sin^2 \theta_W + \left(\frac{1}{2} - \sin^2 \theta_W \right) \right. \\ \left. + \frac{8 \alpha_s}{9 \pi} \left[1 + 1.689 \alpha_s + (3.661 \pm 0.002) \alpha_s^2 \right] \right\} + \mathcal{O}((u^- + d^-)^{-2}) + \mathcal{O}(\alpha_s^4), \quad (4)$$

where the third term in the square brackets is determined by the α_s^3 corrections $\delta c_a^{(3)}(x)$, $a = 2, L, 3$. The perturbation series in the square brackets appears reasonably well convergent for relevant values of the strong coupling constant, with the known terms reading, e.g., $1 + 0.42 + 0.23$ for $\alpha_s = 0.25$. Thus the α_s^2 and α_s^3 contributions correct the NLO estimate by 65% in this case. On the other hand, due to the small prefactor of this expansion, the new third-order term increases the complete curly bracket in Eq. (4) by only about 1%, which can therefore be considered as the new uncertainty of this quantity due to the truncation of the perturbative expansion. Consequently previous NLO estimates of the effect of, for instance, the (presumably

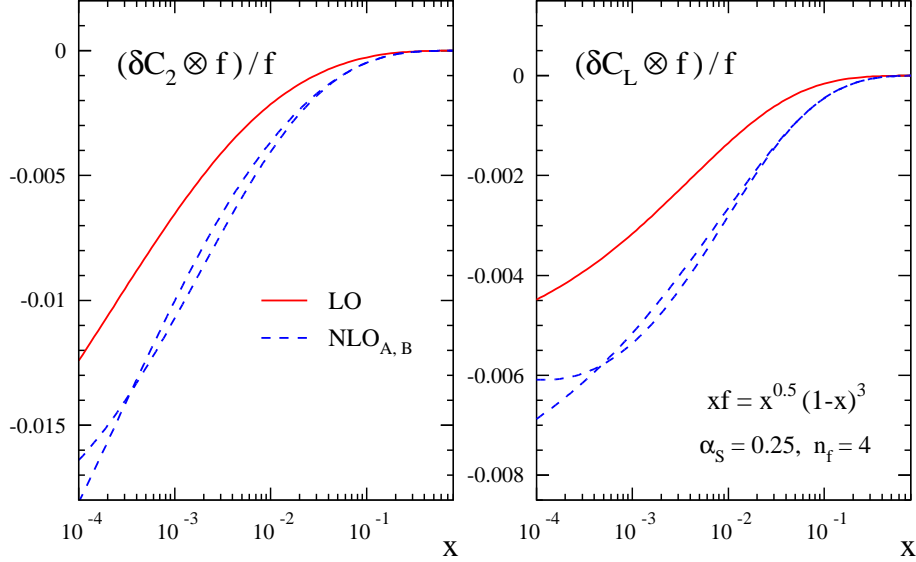


Fig. 3: The first two approximations, denoted by LO and NLO, of the differences (1) for F_2 and F_L in charged-current DIS. The results are shown for representative values of α_s and n_f after convolution with the reference distribution $f(x)$ also employed in Fig. 2. The dashed curves correspond to the two approximation uncertainties for the new α_s^3 contributions.

mainly non-perturbative, see Refs. [37–39]) charge asymmetry of the strange sea remain practically unaffected by higher-order corrections to the coefficient functions.

To summarize, we have extended the fixed- N three-loop calculations of inclusive DIS [2–4] to all charged-current cases not covered by the full (all- N) computations of Refs. [7–9]. The region of applicability of these new results is restricted to Bjorken- x values above about 10^{-3} , a range amply sufficiently for any fixed-target or collider measurements of those charged-current structure functions in the foreseeable future. Except for the longitudinal structure function F_L , the present coefficient functions are part of the next-to-next-to-next-to-leading order (N^3 LO) approximation of massless perturbative QCD. Analyses at this order are possible outside the small- x region since the corresponding four-loop splitting functions will have a very small impact here, cf. Ref. [40].

2.2 Small x resummation ²¹

The splitting functions which govern the evolution of the parton distributions (PDFs), together with the hard cross sections which relate those partons to hadronic physical observables, are potentially unstable at high energy due to logarithmically enhanced contributions. In particular, parametrizing observables such as deep-inelastic structure (DIS) functions or Drell-Yan (DY) or Higgs production cross section in hadronic collisions in terms of a dimensionful scale Q^2 (photon virtuality or invariant mass of the final state in DIS and DY respectively) and a dimensionless ratio x (the Bjorken variable or $\frac{Q^2}{s}$ in DIS and DY respectively), when $x \rightarrow 0$ there are logarithmically enhanced contributions to the perturbation expansion of the form $x^{-1} \alpha_s^n(Q^2) \log^m(1/x)$ ($n \geq m - 1$). When x is sufficiently small, one must resum such terms, reordering the perturbation expansion in terms of leading logarithmic (LL) terms followed by next-to-leading logarithmic (NLL) terms and so on.

The problem can be traced to ladders of t -channel gluon exchanges at LL order, with some quark mixing at NLL order and beyond. The underlying framework for the resummation procedure is the BFKL equation [41, 42], an integral equation for the unintegrated gluon $f(k^2, Q_0^2)$ that is currently known up to full NLL order [43–45], and approximate NNLL order [46]. This has the schematic form (up to NLL):

$$Nf(k^2, Q_0^2) = Nf_I(Q_0^2) + \bar{\alpha}_S(k^2) \int dk'^2 \left[\mathcal{K}_0(k^2, k'^2, Q_0^2) + \bar{\alpha}_S(k^2) \mathcal{K}_1(k^2, k'^2, Q_0^2) \right] f(k'^2), \quad (5)$$

where $f_I(Q_0^2)$ is a non-perturbative initial condition at some initial scale Q_0 , $\bar{\alpha}_S = 3\alpha_S/\pi$ and $\mathcal{K}_{0,1}$ are the

²¹Contributing authors: G. Altarelli, R. D. Ball, M. Ciafaloni, D. Colferai, G. P. Salam, A. Staśto, R. S. Thorne, C. D. White

LL and NLL BFKL kernels. Different choices for the argument of the running coupling are possible, leading to accordingly modified \mathcal{K}_1 [47, 48].

The solution of the BFKL equation can be used to extract leading and subleading singular contributions to singlet DGLAP splitting functions. The BFKL equation can either be solved numerically in its form given by Eq. (5), or else analytically by performing a double Mellin transform with respect to x and k^2 :

$$f(\gamma, N) = \int_0^\infty (k^2)^{-\gamma-1} \int_0^1 dx x^N f(x, k^2), \quad (6)$$

whereby the BFKL equation becomes a differential equation, with kernels $\chi_{0,1}(\gamma)$ defined respectively as the Mellin transforms of $\mathcal{K}_{0,1}$. Furthermore, by using the k_t -factorisation theorem [49], one may determine leading small x contributions to all orders to hard partonic cross sections for physical processes such as heavy quark electroproduction [49] and deep-inelastic scattering [50]. Approximate subleading results are also available [51, 52].

These results for splitting functions and hard partonic cross sections can then be combined with fixed-order results to obtain resummed predictions for physical observables. However, it has now been known for some time that the LL BFKL equation is unable to describe scattering data well, even when matched to a fixed order expansion. Any viable resummation procedure must then, at the very least, satisfy the following requirements:

1. Include a stable solution to the BFKL equation with running coupling up to NLL order.
2. Match to the standard DGLAP description at moderate and high x values (where this is known to describe data well).
3. Provide the complete set of splitting and coefficient functions for F_2 and F_L in a well defined factorisation scheme.

Over the past few years, three approaches have emerged which, to some extent, aim at fulfilling these conditions. Here we call these the ABF [53–60], CCSS [48, 61–67] and TW [68–73] approaches. In the ABF scheme all three requirements are met, and resummed splitting functions in the singlet sector have been determined. Furthermore, a complete control of the scheme dependence at the resummed level has been achieved, thereby allowing for a consistent determination of resummed deep-inelastic coefficient functions, and thus of resummed structure functions. However, the results obtained thus have not been fit to the data yet. In the CCSS formalism, resummed splitting functions have also been determined. However, results are given in a scheme which differs from the $\overline{\text{MS}}$ scheme at the resummed level; furthermore, resummed coefficient functions and physical observables haven't been constructed yet. The TW approach, instead, has already been compared to the data in a global fit. However, this approach makes a number of simplifying assumptions and the ensuing resummation is thus not as complete as that which obtains in other approaches: for example, this approach does not include the full collinear resummation of the BFKL kernel.

A comparison of resummed splitting functions and solution of evolution equations determined in the ABF and CCSS approaches with $n_f = 0$ was presented in Ref. [1]; the main features and differences of these approaches were also discussed. Here, we extend this comparison to the case of $n_f \neq 0$ resummation, and also to the TW approach. First, we will briefly summarize the main features of each approach, and in particular we display the matrix of splitting functions determined in the ABF and CCSS approaches. Then, we will compare K -factors for physical observables determined using the ABF and TW approach.

Note that there are some difference in notations between various groups, which are retained here in order to simplify comparison to the original literature. In particular, the variable N in Eq. (6) will be referred to as ω in the CCS approach of Section 2.2.2, and the variable γ in the same equation will be referred to as M in the ABF approach of Section 2.2.1.

2.2.1 The Altarelli-Ball-Forte (ABF) Approach

In the ABF approach [53–60, 74–77] one concentrates on the problem of obtaining an improved anomalous dimension (splitting function) for DIS which reduces to the ordinary perturbative result at large N (large x),

thereby automatically satisfying renormalization group constraints, while including resummed BFKL corrections at small N (small x), determined through the renormalization-group improved (i.e. running coupling) version of the BFKL kernel. The ordinary perturbative result for the singlet anomalous dimension is given by:

$$\gamma(N, \alpha_s) = \alpha_s \gamma_0(N) + \alpha_s^2 \gamma_1(N) + \alpha_s^3 \gamma_2(N) \dots \quad (7)$$

The BFKL corrections at small N (small x) are determined by the BFKL kernel $\chi(M, \alpha_s)$:

$$\chi(M, \alpha_s) = \alpha_s \chi_0(M) + \alpha_s^2 \chi_1(M) + \dots, \quad (8)$$

which is the Mellin transform, with respect to $t = \ln \frac{k^2}{k_0^2}$, of the $N \rightarrow 0$ angular averaged BFKL kernel.

The ABF construction is based on three ingredients.

1. *The duality relation* between the kernels χ and γ

$$\chi(\gamma(N, \alpha_s), \alpha_s) = N, \quad (9)$$

which is a consequence of the fact that at fixed coupling the solutions of the BFKL and DGLAP equations should coincide at leading twist [53, 74, 78]. By using duality, one can use the perturbative expansions of γ and χ in powers of α_s to improve (resum) each other: by combining them, one obtains a "double leading" (DL) expansion which includes all leading (and subleading, at NLO) logs of x and Q^2 . In particular, the DL expansion automatically resums the collinear poles of χ at $M = 0$. This eliminates the alternating sign poles $+1/M, -1/M^2, \dots$ that appear in χ_0, χ_1, \dots , and make the perturbative expansion of χ unreliable. This result is a model independent consequence of momentum conservation $\gamma(1, \alpha_s) = 0$, whence, by duality:

$$\chi(0, \alpha_s) = 1. \quad (10)$$

2. *The symmetry of the BFKL kernel* upon gluon interchange. In Mellin space, this symmetry implies that at the fixed-coupling level the kernel χ for evolution in $\ln \frac{s}{k k_0}$ must satisfy $\chi(M) = \chi(1 - M)$. By exploiting this symmetry, one can use the collinear resummation of the region $M \sim 0$ which was obtained using the double-leading expansion to also improve the BFKL kernel in the anti-collinear $M \simeq 1$ region. This leads to a symmetric kernel which is an entire function for all M , and has a minimum at $M = \frac{1}{2}$. The symmetry is broken by the DIS choice of variables $\ln \frac{1}{x} = \ln \frac{s}{Q^2}$ and by the running of the coupling; however these symmetry breaking contribution can be determined exactly. This then leads to a stable resummed expansion of the resummed anomalous dimension at the fixed coupling level.
3. *The running-coupling resummation* of the BFKL solution. Whereas running coupling corrections to evolution equations are automatically included when solving the DGLAP evolution equation with resummed anomalous dimensions, the duality relation Eq. (9) itself undergoes corrections when the running coupling is included in the BFKL equation (5). Running coupling corrections can then be derived order by order, and turn out to be affected by singularities in Mellin M space. This implies that after Mellin inversion the associate splitting functions is enhanced as $x \rightarrow 0$: their contribution grows as $(\alpha_s \beta_0 \ln \frac{1}{x})^n$ with the perturbative order. However the series of leading enhanced contribution can be summed at all orders in closed form, because it corresponds to the asymptotic expansion in powers of α_s of the solution to the running coupling BFKL equation (5) when the kernel χ is approximated quadratically about its minimum. This exact solution can be expressed in terms of Airy functions [54, 79] when the kernel is linear in α_s and in terms of Bateman [56] functions for generic kernels. Because both the exact solution and its asymptotic expansion are known, this BFKL running coupling resummation can be combined with the DGLAP anomalous dimension, already resummed at the BFKL fixed coupling level, with full control of overlap (double counting terms). Schematically, the result has the following form:

$$\begin{aligned} \gamma_{\Sigma NLO}^{rc}(\alpha_s(t), N) &= \gamma_{\Sigma NLO}^{rc, pert}(\alpha_s(t), N) + \gamma^B(\alpha_s(t), N) - \gamma_s^B(\alpha_s(t), N) - \gamma_{ss}^B(\alpha_s(t), N) \\ &\quad - \gamma_{ss,0}^B(\alpha_s(t), N) + \gamma_{\text{match}}(\alpha_s(t), N) + \gamma_{\text{mom}}(\alpha_s(t), N), \end{aligned} \quad (11)$$

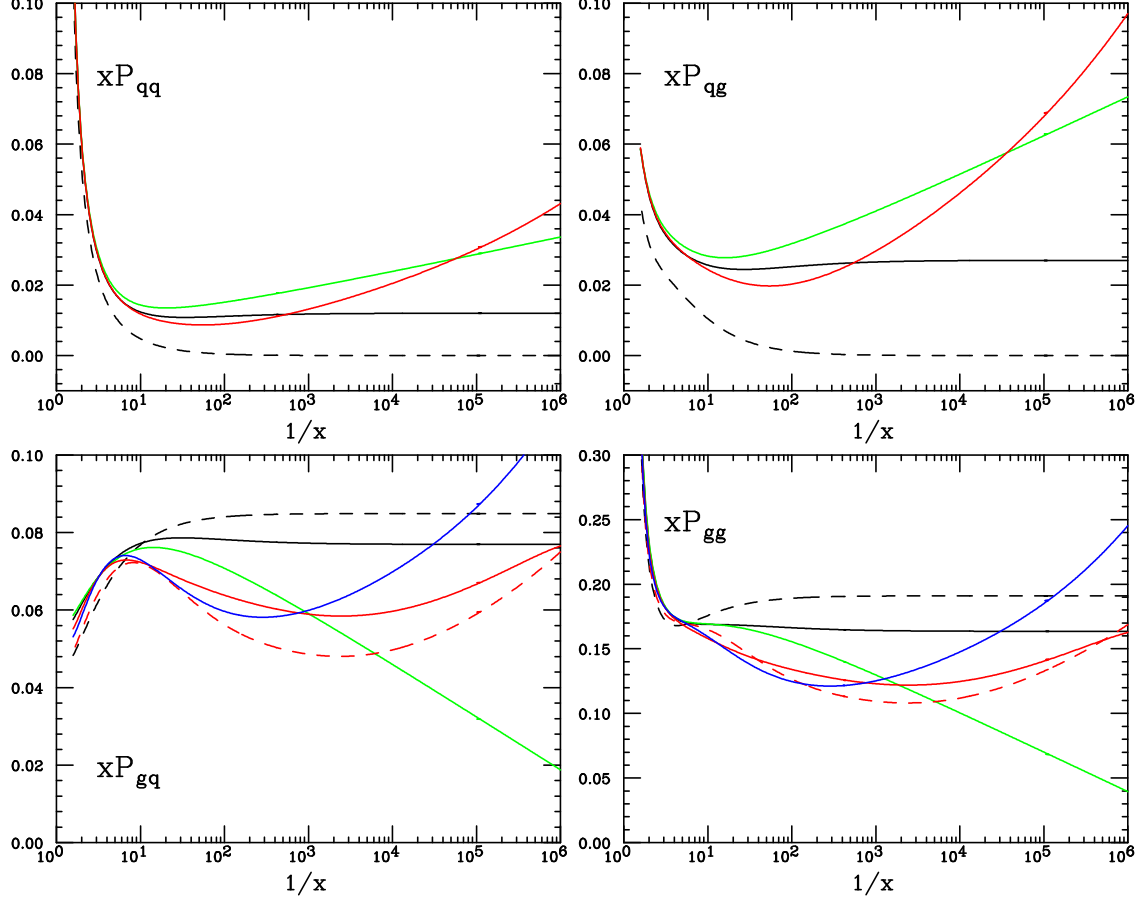


Fig. 4: The resummed splittings functions P_{qq} , P_{qg} , P_{gq} and P_{gg} in the ABF approach, all for $n_f = 4$ and $\alpha_s = 0.2$: LO DGLAP (dashed black), NLO DGLAP (solid black), NNLO DGLAP (solid green), LO resummed (red dashed), NLO resummed in the $\overline{\text{MS}}$ scheme (red) and in the $\overline{\text{MS}}$ scheme (blue).

where $\gamma_{\Sigma NLO}^{rc, pert}(\alpha_s(t), N)$ contains all terms which are up to NLO in the double-leading expansion of point 1, symmetrized as discussed in point 2 above so that its dual χ has a minimum; $\gamma^B(\alpha_s(t), N)$ resums the series of singular running coupling corrections using the aforementioned exact BFKL solution in terms of a Bateman function; $\gamma_s^B(\alpha_s(t), N)$, $\gamma_{ss}^B(\alpha_s(t), N)$, $\gamma_{ss,0}^B(\alpha_s(t), N)$ are double counting subtractions between the previous two contributions; γ_{mom} subtracts subleading terms which spoil exact momentum conservation; γ_{match} subtracts any contribution which deviates from NLO DGLAP and at large N doesn't drop at least as $\frac{1}{N}$.

The anomalous dimension obtained through this procedure has a simple pole as a leading small- N (i.e. small x) singularity, like the LO DGLAP anomalous dimension. The location of the pole is to the right of the DGLAP pole, and it depends on the value of α_s . Thanks to the softening due to running of the coupling, this value is however rather smaller than that which corresponds to the leading BFKL singularity: for example, for $\alpha_s = 0.2$, when $n_f = 0$ the pole is at $N = 0.17$.

The splitting function obtained by Mellin inversion of the anomalous dimension eq. (11) turns out to agree at the percent level to that obtained by the CCSS group by numerical resolution of the BFKL equation for all $x \lesssim 10^{-2}$; for larger values of x (i.e. in the matching region) the ABF result is closer to the NLO DGLAP result.

In order to obtain a full resummation of physical observables, specifically for deep-inelastic scattering, the resummation discussed so far has to be extended to the quark sector and to hard partonic coefficients. This, on top of various technical complications, requires two main conceptual steps:

- A factorization scheme must be defined at a resummed level. Because only one of the two eigenvectors

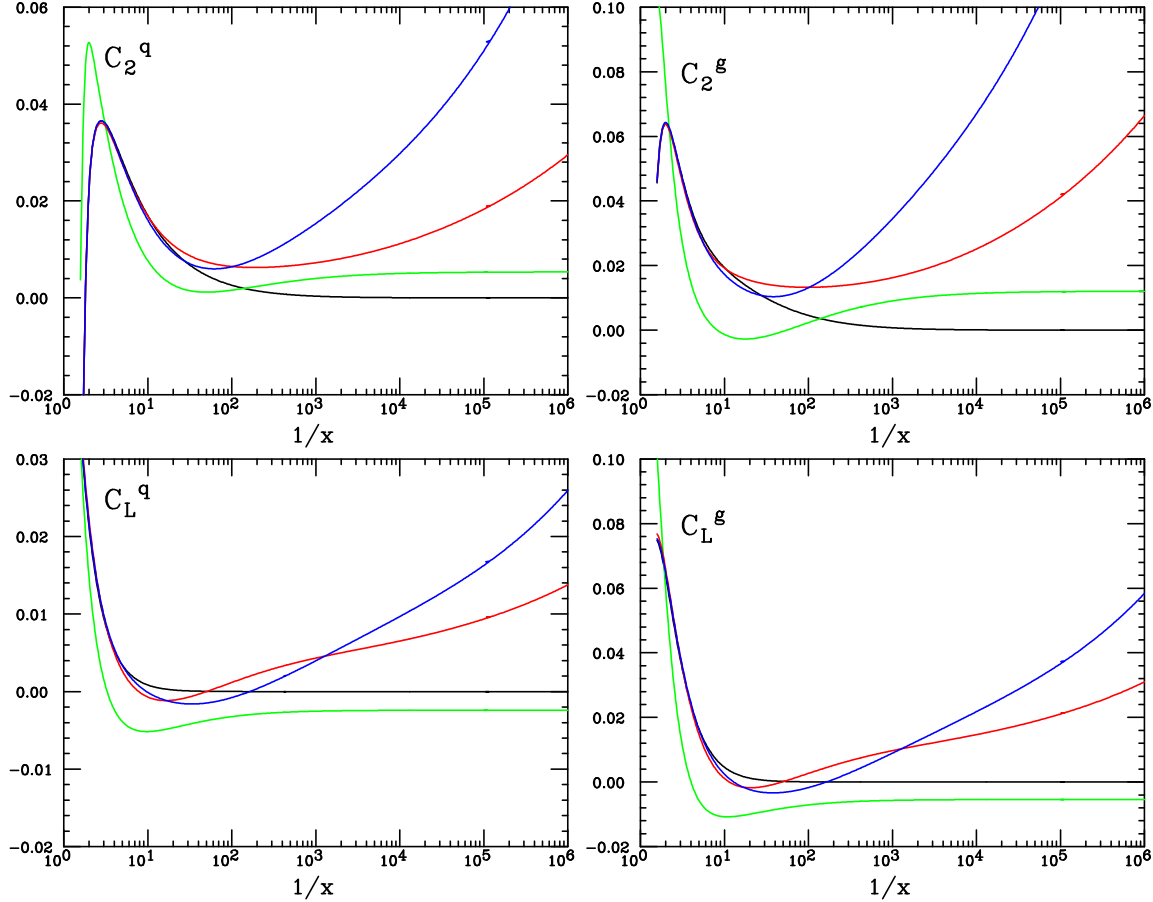


Fig. 5: The resummed DIS coefficient functions C_{2q} , C_{2g} , C_{Lq} and C_{Lg} in the ABF approach, all for $n_f = 4$ and $\alpha_s = 0.2$. The curves are labelled as in the previous figure.

of the matrix of anomalous dimensions is affected by resummation, once a scheme is chosen, the resummation discussed above determines entirely the two-by-two matrix of splitting functions in the singlet sector. The only important requirement is that the relation of this small x scheme choice to standard large x schemes be known exactly, since this enables one to combine resummed results with known fixed order results.

- PDFs evolved using resummed evolution equations must be combined with resummed coefficient functions. These are known, specifically for DIS [50], but are also known [80] to be affected by singularities, analogous to the running coupling singularities of the resummed anomalous dimension discussed above, which likewise must be resummed to all orders [58]. This running coupling resummation of the coefficient function significantly softens the small x growth of the coefficient function and substantially reduces its scheme dependence [59].

These steps have been accomplished in Ref. [59], where resummed anomalous dimensions (see fig. 4), coefficient functions (see fig.5) and structure functions (see section 2.2.4 below) have been determined. The scheme dependence of these results can be studied in detail: results have been produced and compared in both the $\overline{\text{MS}}$ and $\text{Q}_0\overline{\text{MS}}$ schemes, and furthermore the variation of results upon variation of factorization and renormalization scales has been studied.

Calculations of resummation corrections not only of deep inelastic processes, but also of benchmark hadronic processes such as Drell-Yan, vector boson, heavy quark and Higgs production are now possible and should be explored.

2.2.2 The Ciafaloni-Colferai-Salam-Stasto (CCSS) Approach

The Ciafaloni-Colferai-Salam-Stasto (CCSS) resummation approach proposed in a series of papers [48, 61–67] is based on the few general principles:

- We impose the so-called kinematical constraint [81–83] onto the real gluon emission terms in the BFKL kernel. The effect of this constraint is to cut out the regions of the phase space for which $k_T'^2 \geq k_T^2/z$ where k_T, k_T' are the transverse momenta of the exchanged gluons and z is the fraction of the longitudinal momentum.
- The matching with the DGLAP anomalous dimension is done up to the next-to-leading order.
- We impose the momentum sum rule onto the resummed anomalous dimensions.
- Running coupling is included with the appropriate choice of scale. We take the argument of the running coupling to be the transverse momentum squared of the emitted gluon in the BFKL ladder in the BFKL part. For the part which multiplies the DGLAP terms in the eigenvalue equation we choose the scale to be the maximal between k_T^2 and $k_T'^2$.
- All the calculations are performed directly in momentum space. This in particular enables easy implementation of the running of the coupling with the choice of the arguments as described above.

The implementation at the leading logarithmic level in BFKL and DGLAP (and in the single gluon channel case) works as follows. It is convenient to go to the Mellin space representation where we denote by γ and ω the Mellin variables conjugated to $\ln k_T$ and $\ln 1/x$ respectively. The full evolution kernel can be represented as a series $\mathcal{K} = \sum_n \alpha_s^{n+1} \mathcal{K}_n(\gamma, \omega)$. We take the resummed kernel at the lowest order level to be

$$\mathcal{K}_0(\gamma, \omega) = \frac{2C_A}{\omega} \chi_0^\omega(\gamma) + [\gamma_0^{gg}(\omega) - \frac{2C_A}{\omega}] \chi_c^\omega(\gamma). \quad (12)$$

The terms in (12) are the following

$$\chi_0^\omega(\gamma) = 2\psi(1) - \psi(\gamma) - \psi(1 - \gamma + \omega),$$

is the leading logarithmic BFKL kernel eigenvalue with the kinematical constraint imposed. This is reflected by the fact that the singularities in the γ plane at $\gamma = 1$ are shifted by the ω . This ensures the compatibility with the DGLAP collinear poles, in the sense that we have only single poles in γ . The function $\chi_c(\gamma)$ is the collinear part of the kernel

$$\chi_c^\omega(\gamma) = \frac{1}{\gamma} + \frac{1}{1 - \gamma + \omega},$$

which includes only the leading collinear poles at $\gamma = 0$ or 1 . All the higher twist poles are neglected for this part of the kernel. This kernel eigenvalue is multiplied by the non-singular (in ω) part of the DGLAP anomalous dimension $\gamma_0^{gg}(\omega) - 2C_A/\omega$ where $\gamma_0^{gg}(\omega)$ is the full anomalous dimension at the leading order. The next-to-leading parts both in BFKL and DGLAP are included in the second term in the expansion, i.e. kernel \mathcal{K}_1

$$\mathcal{K}_1(\gamma, \omega) = \frac{(2C_A)^2}{\omega} \tilde{\chi}_1^\omega(\gamma) + \tilde{\gamma}_1^{gg}(\omega) \chi_c^\omega(\omega) \quad (13)$$

where $\tilde{\chi}_1^\omega(\gamma)$ is the NLL in x part of the BFKL kernel eigenvalue with subtractions. These subtractions are necessary to avoid double counting: we need to subtract the double and triple collinear poles in γ which are already included in the resummed expression (12) and which can be easily identified by expanding this expression in powers of ω and using the LO relation $\omega = \bar{\alpha}_s \chi_0(\gamma)$. The term $\tilde{\gamma}_1^{gg}(\omega)$ in Eq. (13) is chosen so that one obtains the correct DGLAP anomalous dimension at a fixed next-to-leading logarithmic level. The formalism described above has been proven to work successfully in the single channel case, that is for evolution of gluons only. The solution was shown to be very stable with respect to the changes of the resummation scheme.

The quarks are included in the CCSS approach by a matrix formalism. The basic assumptions in this construction are:

- Consistency with the collinear matrix factorization of the PDFs in the singlet evolution.

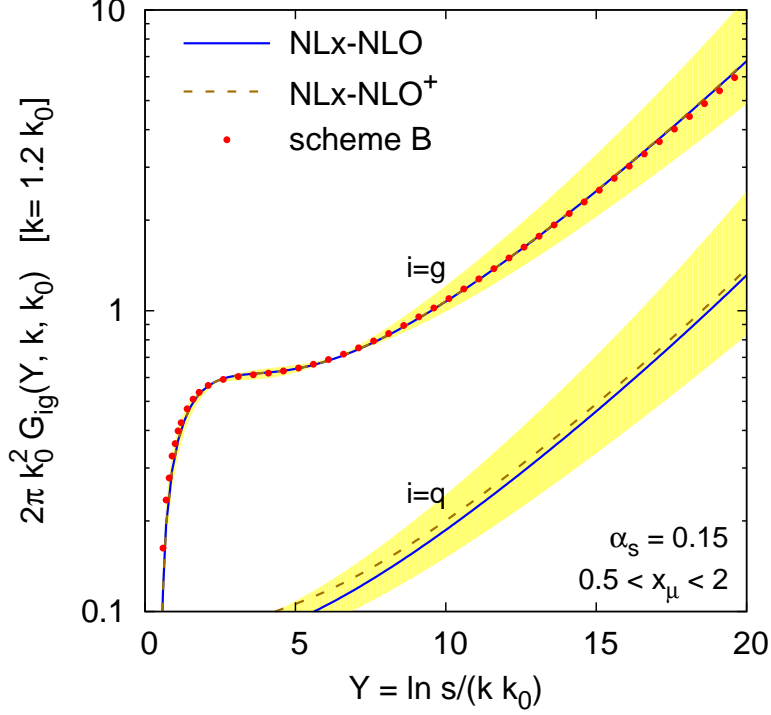


Fig. 6: Gluon-induced part of the Green function for the NLx-NLO and NLx-NLO⁺ models, compared to the results the single channel approach. For the models of this paper both gluon-gluon and quark-gluon Green's function are shown. The value chosen for the coupling, $\alpha_s = 0.15$, corresponds to $k_0 \simeq 20$ GeV. The band indicates the spread in the result for the NLx-NLO model when varying the renormalization scale in the range $0.5 < x_\mu < 2$.

- Requirement that only single pole singularities in both in γ and ω are present in the kernel eigenvalues. This assumption allows for the natural consistency with DGLAP and BFKL respectively. Higher order singularities can be generated at higher orders only through the subleading dependencies on these two variables.
- Ability to compute all the anomalous dimensions which can be directly compared with the DGLAP approach. This can be done by using set of recursive equations which allow to calculate the anomalous dimensions order by order from the kernel eigenvalues.
- Impose the collinear-anticollinear symmetry of the kernel matrix via the similarity transformation.
- Incorporate NLLx BFKL and DGLAP up to NLO (and possibly NNLO).

The direct solutions to the matrix equations are the quark and gluon Green's functions. These are presented in Fig. 6 for the case of the gluon-gluon and quark-gluon part. The resulting gluon-gluon part is increasing exponentially with the logarithm of energy $\ln s$ with an effective intercept of about ~ 0.25 . It is much suppressed with respect to the leading logarithmic order. We also note that the single channel results and the matrix results for the gluon-gluon Green's function are very similar to each other. In Fig. 6 we also present the quark-gluon channel which is naturally suppressed in normalization with respect to the gluon-gluon one by a factor of the strong coupling constant. This can be intuitively understood as the (singlet) quarks are radiatively generated from the gluons, and therefore this component follows the gluon density very closely. The yellow bands indicate the change of the Green's functions with respect to the change of the scale.

In Fig. 7 we present all four splitting functions for fixed value of scale Q^2 . Here, again the results are very close to the previous single channel approach in the case of the gluon-gluon splitting function. The gluon-quark channel is very close to the gluon-gluon one, with the characteristic dip of this function at about $x \sim 10^{-3}$. The dip delays the onset of rise of the splitting function only to values of x of about 10^{-4} . The scale dependence grows with decreasing x but it is not larger than in the fixed NLO case. The quark-gluon and quark-quark splitting functions tend to have slightly larger uncertainty due to the scale change but are also slightly closer to the plain NLO calculation. They also tend to have a less pronounced dip structure.

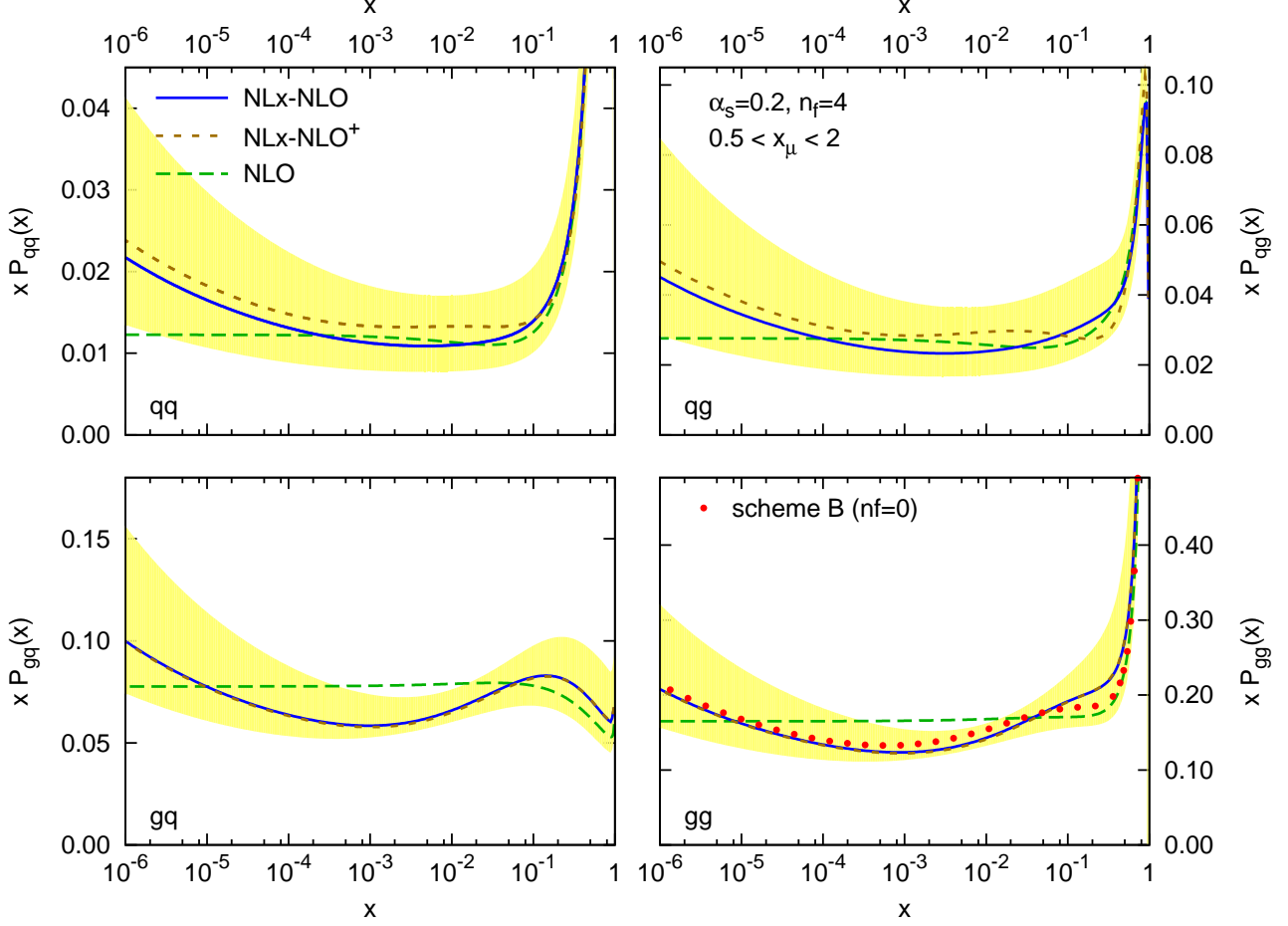


Fig. 7: The matrix of NLx-NLO (and NLx-NLO⁺) splitting functions together with their scale uncertainty and the NLO splitting functions for comparison. In the gg channel, we also show the old scheme B result ($n_f = 0$, no NLO contributions, 1-loop coupling). The band corresponds to the span of results (NLx-NLO) obtained if one chooses $x_\mu = 0.5$ and $x_\mu = 2.0$.

2.2.3 The Thorne-White (TW) Approach

Substituting the LO running coupling $\bar{\alpha}_S(k^2)$ into equation (5) and performing a double Mellin transform according to equation (6), the BFKL equation 5, as mentioned in Section 2.2, becomes a differential equation:

$$\frac{d^2 f(\gamma, N)}{d\gamma^2} = \frac{d^2 f_I(\gamma, Q_0^2)}{d\gamma^2} - \frac{1}{\bar{\beta}_0 N} \frac{d(\chi_0(\gamma)f(\gamma, N))}{d\gamma} + \frac{\pi}{3\bar{\beta}_0^2 N} \chi_1(\gamma)f(\gamma, N), \quad (14)$$

where $\chi_{0,1}(\gamma)$ are the Mellin transforms of $\mathcal{K}_{0,1}$. The solution for $f(N, \gamma)$ of Eq. (14) has the following form [62, 84]:

$$f(N, \gamma) = \exp\left(-\frac{X_1(\gamma)}{\bar{\beta}_0 N}\right) \int_\gamma^\infty A(\tilde{\gamma}) \exp\left(\frac{X_1(\tilde{\gamma})}{\bar{\beta}_0 N}\right) d\tilde{\gamma}. \quad (15)$$

Up to power-suppressed corrections, one may shift the lower limit of the integral $\gamma \rightarrow 0$, so that the gluon distribution factorises into the product of a perturbative and a non-perturbative piece. The nonperturbative piece depends on the bare input gluon distribution and an in principle calculable hard contribution. However, this latter part is rendered ambiguous by diffusion into the infrared, and in this approach is contaminated by infrared renormalon-type contributions. The perturbative piece is safe from this and is sensitive to diffusion into the ultraviolet region of weaker coupling. Substituting equation (15) into (14), one finds that the perturbative piece is given (after transforming back to momentum space):

$$\mathcal{G}_E^1(N, t) = \frac{1}{2\pi i} \int_{1/2-i\infty}^{1/2+i\infty} \frac{f\beta_0}{\gamma} \exp[\gamma t - X_1(\gamma, N)/(\bar{\beta}_0 N)] d\gamma, \quad (16)$$

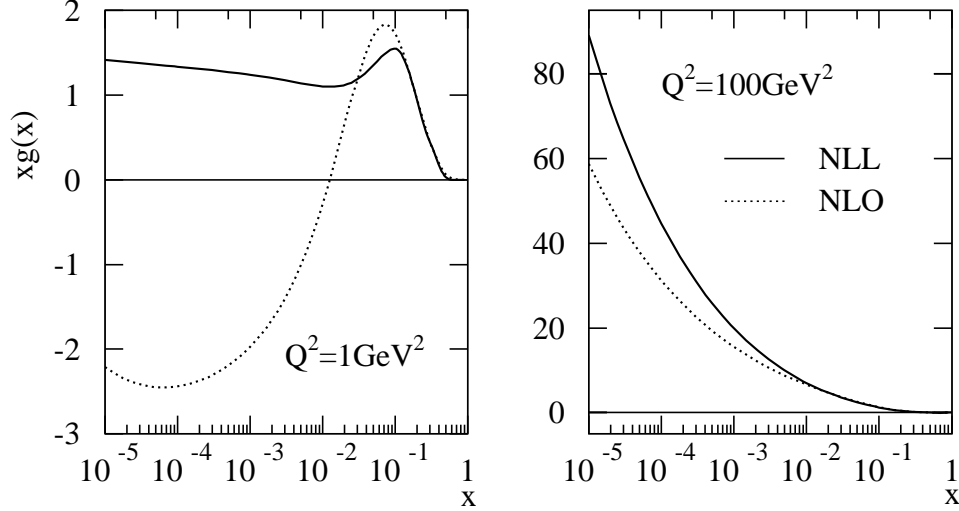


Fig. 8: Gluons arising from a global fit to scattering data including NLL small x resummations in the DIS(x) factorisation scheme (solid). Also shown is the result from an NLO DGLAP fit in the same scheme.

where:

$$X_1(\gamma, N) = \int_{\frac{1}{2}}^{\gamma} \left[\chi_0(\tilde{\gamma}) + N \frac{\chi_1(\tilde{\gamma})}{\chi_0(\tilde{\gamma})} \right] d\tilde{\gamma}. \quad (17)$$

Structure functions F_i also factorize, and the perturbative factors have a similar form to Eq. (16), but involve an additional impact factor $h_i(\gamma, N)$ in the integrand according to the k_t -factorisation theorem [50]. Crucially, coefficient functions and anomalous dimensions involve ratios of the above quantities, such that the non-perturbative factor cancels. Thus, once all the impact factors are known, the complete set of coefficient and splitting functions can be disentangled. Finally they can be combined with the standard NLO DGLAP results (which are known to describe data well at higher x values) using the simple prescription:

$$P^{tot.} = P^{NLL} + P^{NLO} - \left[P^{NLL(0)} + P^{NLL(1)} \right], \quad (18)$$

where P is a splitting or coefficient function, and $P^{NLL(i)}$ the $\mathcal{O}(\alpha_s^i)$ contribution to the resummed result which is subtracted to avoid double-counting. It should be noted that the method of subtraction of the resummed contribution in the matching is different to that for the ABF approach outlined after Eq. (11). For example, at NLO in the resummation the BFKL equation provides both the α_S/N part of P_{gg} and the part at $\mathcal{O}(\alpha_S)$ constant as $N \rightarrow \infty$. Hence we choose to keep all terms constant as $N \rightarrow \infty$ generated by Eq. (16), with similar considerations for other splitting functions and coefficient functions, though these can contain terms $\propto N$. Hence, we include terms which will have some influence out to much higher x than in the ABF approach.

In the TW manner of counting orders LL is defined as the first order at which contributions appear, so while for the gluon splitting function this is for $\bar{\alpha}_S^n \ln^m(1/x)$ for $m = n - 1$ for impact factors this is for $m = n - 2$. A potential problem therefore arises in that the NLL impact factors are not known exactly. However, the LL impact factors with conservation of energy of the gluon imposed are known in cases of both massless and massive quarks [51, 52], and are known to provide a very good approximation to the full $\mathcal{O}(\alpha_S^2)$ and $\mathcal{O}(\alpha_S^3)$ quark-gluon splitting functions and coefficient functions [85], implying that they must contain much of the important higher-order information. These can then be used to calculate NLL coefficient and

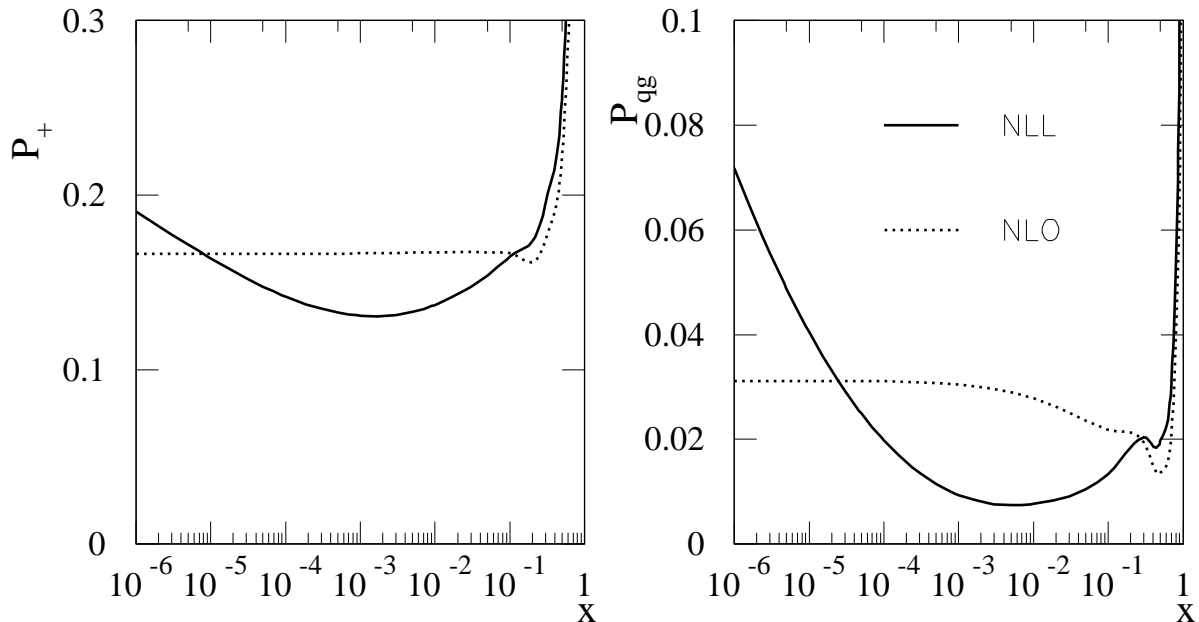


Fig. 9: The resummed splitting functions (solid) $P_+ \approx P_{gg}$ and P_{qg} in the TW approach, both for $n_f = 4$ and $\alpha_S = 0.16$, compared to the corresponding NLO forms (dotted).

splitting functions within a particular factorisation scheme. One must also specify a general mass variable number scheme for consistent implementation of heavy quark mass effects. Such a scheme (called the DIS(χ) scheme) has been given in [72, 73] up to NLL order in the high energy expansion, and NLO order in the fixed order expansion.

The form of the resummed splitting functions shown in fig. 9 are qualitatively consistent with those from the ABF approach, fig. 4, and CCSS approach fig. 7 (note however that in these plots the value of α_s is a little larger, and the scheme is different). This is despite the fact that the approach does not include the explicit collinear resummation of the BFKL kernel adopted in the other two approaches. It was maintained in [70, 71] that the diffusion into the ultraviolet, effectively making the coupling weaker, hastens the perturbative convergence for splitting functions, and the kernel near $\gamma = 0$, making this additional resummation less necessary. There is no particular obstruction to including this resummation in the approach, it is simply cumbersome. Indeed, in Ref. [71] the effect was checked, and modifications found to be no greater than generic NNLO corrections to the resummation, so it was omitted. (Note that any process where there are two hard scales, sensitive to $\gamma \approx 0.5$, or attempted calculation of the hard input for the gluon distribution, sensitive to $\gamma = 1$, would find this resummation essential.) The main feature of the resummed splitting functions is a significant dip below the NLO DGLAP results, followed by an eventual rise at very low $x \simeq 10^{-5}$. This behaviour drives a qualitative change in the gluon distribution, when implemented in a fit to data.

The combined NLO+NLL splitting and coefficient functions (in the TW approach) have been implemented in a global fit to DIS and related data in the DIS(χ) scheme, thus including small x resummations in both the massless and massive quark sectors [73]. The overall fit quality was better than a standard NLO fit in the same factorisation scheme, and a similar NLO fit in the more conventional $\overline{\text{MS}}$ factorisation scheme. The principal reason for this is the dip in the resummed evolution kernels, which allows the gluon distribution to increase at both high and low values of x . This reduces a tension that exists between the high x jet data

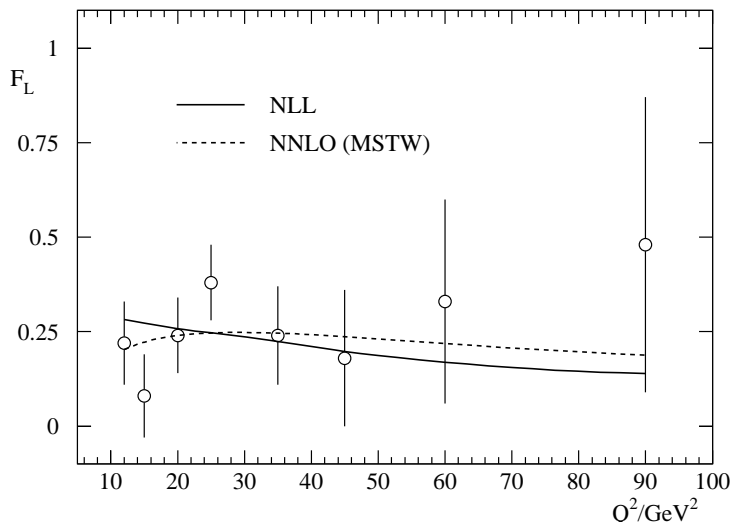


Fig. 10: Recent H1 data on the longitudinal structure function F_L , together with the NLL resummed prediction from the TW approach, and a recent NNLO result from the MSTW group.

of [86, 87] and the low x HERA data [18, 88–91]. The gluon distributions arising from the NLL and NLO fits are shown in figure 8, for the starting scale $Q^2 = 1\text{GeV}^2$ and also for a higher value of Q^2 . One sees that whilst the NLO gluon wants to be negative at low x and Q^2 , the resummed gluon is positive definite and indeed growing slightly as $x \rightarrow 0$. The gluons agree well for higher x values (where the DGLAP description is expected to dominate), but deviate for $x \leq 10^{-2}$. This can therefore be thought of as the value of x below which resummation starts to become relevant.

The qualitatively different gluon from the resummed fit (together with the decreased evolution kernels w.r.t. the fixed order description) has a number of phenomenological implications:

1. The longitudinal structure function F_L is sensible at small x and Q^2 values, where the standard DGLAP description shows a marked instability [92].
2. As a result of the predicted growth of F_L at small x the resummed result for the DIS reduced cross-section shows a turnover at high inelasticity y , in agreement with the HERA data. This behaviour is not correctly predicted by some fixed order fits.
3. The heavy flavour contribution (from charm and bottom) to F_2 is reduced at higher Q^2 in the resummed approach, due mainly to the decreased evolution, as already noted in a full analysis in the fixed-order expansion at NNLO [93]. Nevertheless, it remains a significant fraction of the total structure function at small x .

Other resummation approaches should see similar results when confronted with data, given the qualitative (and indeed quantitative) similarities between the splitting functions. It is the decreased evolution with respect to the DGLAP description that drives the qualitative change in the gluon distribution. This is then the source of any quantitative improvement in the description of data, and also the enhanced description of the longitudinal structure function and reduced cross-section.

The resummed prediction for F_L is shown alongside the recent H1 data [94] in figure 10, and compared with an up-to-date NNLO fixed order result [95]. One sees that the data cannot yet tell apart the predictions, but that they are starting to diverge at low x and Q^2 , such that data in this range may indeed be sensitive to the differences between resummed and fixed order approaches.

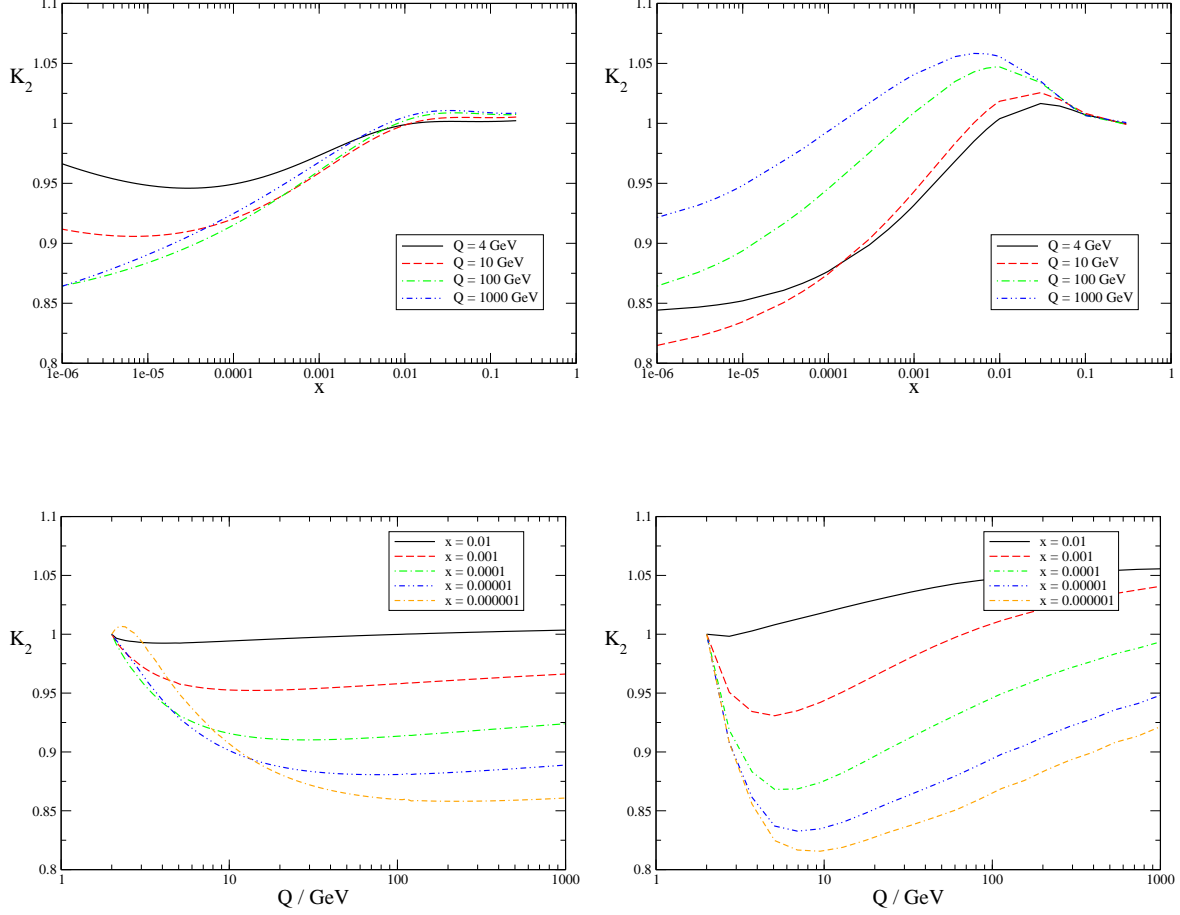


Fig. 11: The ratio F_2^{NLL}/F_2^{NLO} in the ABF approach (left) and the TW approach (right), using toy PDFs, given in eq. 20, calculated as function of x at fixed for Q^2 (upper), and as a function of Q^2 at fixed x (lower).

2.2.4 Resummed structure functions: comparison of the ABF and TW approaches

In this section, we present an application of the ABF and TW approaches to the resummed determination of the F_2 and F_L deep-inelastic structure functions. The corresponding exercise for the CCSS approach has not yet been finalised. A direct comparison of the two approaches is complicated by issues of factorisation scheme dependence: whereas in the ABF approach results may be obtained in any scheme, and in particular the $\overline{\text{MS}}$ and closely related $Q_0\text{-}\overline{\text{MS}}$ scheme, in the TW formalism splitting functions and coefficient functions beyond NLO in α_S are resummed in the $Q_0\text{-DIS}$ scheme [66, 96], which coincides with the standard DIS scheme at large x but differs from it at the resummed level; the scheme change needed in order to obtain the coefficient functions from the DIS-scheme ones is performed exactly up to NLO and approximately beyond it. Thus, without a more precise definition of the relation of this scheme to $\overline{\text{MS}}$, one cannot compare splitting and coefficient functions, which are factorisation scheme dependent.

A useful compromise is to present the respective results for the ratio of structure function predictions:

$$K_i = \frac{F_i^{NLL}(x, Q^2)}{F_i^{NLO}(x, Q^2)}, \quad (19)$$

where $i \in 2, L$, and the F_i are calculated by convoluting the relevant coefficients with PDFs obtained by perturbative evolution of a common set of partons, defined at a starting scale of $Q_0^2 = 4\text{GeV}^2$. The number of flavors is fixed to three, to avoid ambiguities due to heavy quark effects. The initial PDFs are assumed to be fixed (i.e., the same at the unresummed and resummed level) in the DIS factorization scheme at the scale Q_0 . Of course, in a realistic situation the data are fixed and the PDFs are determined by a fit to the data: hence they are not the same at the resummed and unresummed level (compare Fig. 8 above). However, in the DIS

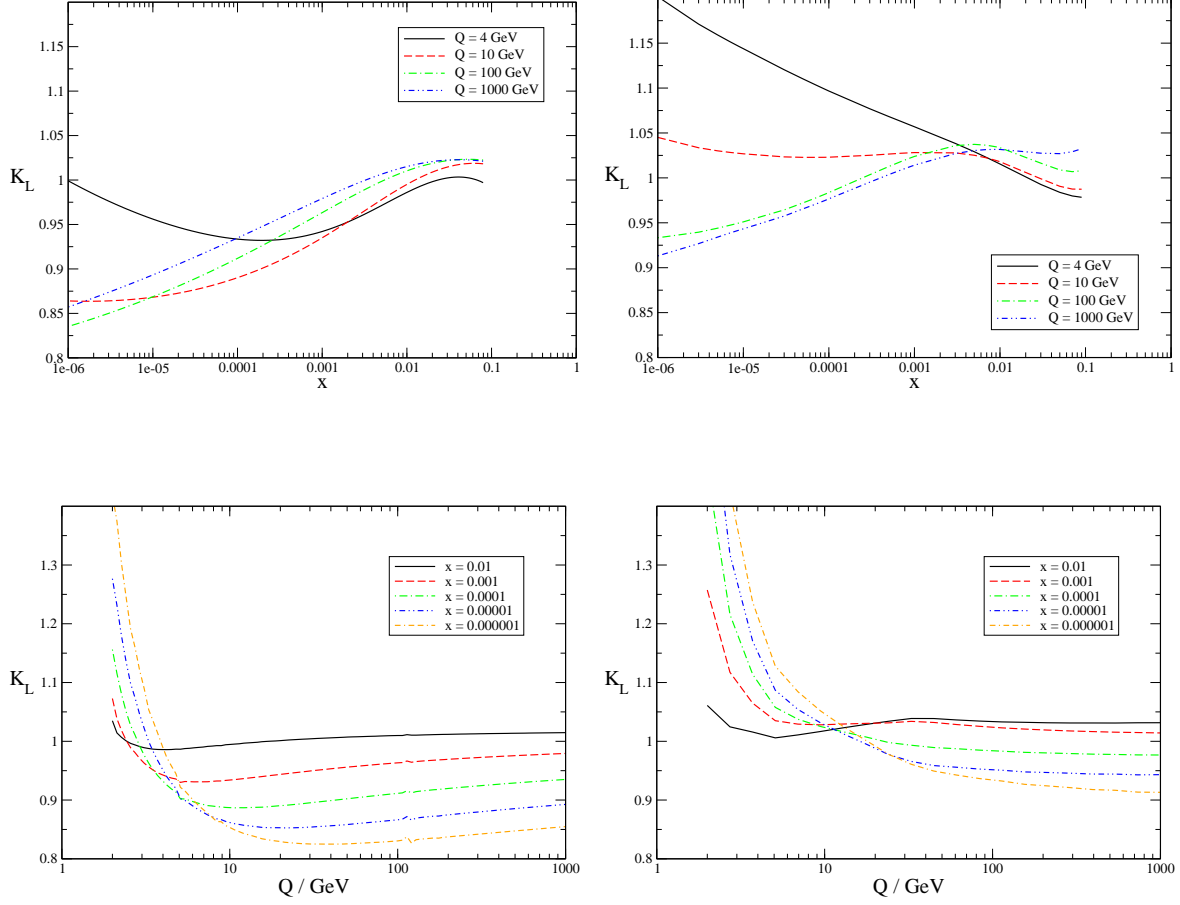


Fig. 12: The ratio F_L^{NLL}/F_L^{NLO} in the ABF approach (left) and the TW approach (right), using toy PDFs, given in eq. 20, calculated as function of x at fixed for Q^2 (upper), and as a function of Q^2 at fixed x (lower).

factorization scheme the structure function F_2 is simply proportional to the quark distribution, hence by fixing the PDFs in this scheme one ensures that F_2 is fixed at the starting scale.

This starting PDFs are constructed as follows: the quark and gluon distributions are chosen to have the representative form also used in Ref. [59]

$$xg(x) = k_s x S(x) = k_g x^{-0.18} (1-x)^5; \quad xq_v = k_q x^{0.5} (1-x)^4, \quad (20)$$

in the $\overline{\text{MS}}$ scheme, where $g(x)$ is the gluon, $S(x)$ the sea quark distribution, and $xq_v(x)$ denotes a valence quark distribution. We choose $k_s = 3$, and then all other parameters are fixed by momentum and number sum rules. Note that the gluon is the same as that used in the previous comparison of Ref. [1]. The PDFs eq. (20) are then transformed to the DIS factorization scheme [97] using the NLO (unresummed) scheme change at the scale Q_0 . The result is then used as a fixed boundary condition for all (unresummed and resummed, ABF and TW) calculations. In the TW approach, the DIS scheme for unresummed quantities and Q_0 DIS scheme as discussed above is then used throughout. In the ABF approach, the fixed DIS-scheme boundary condition is transformed to the $Q_0\overline{\text{MS}}$ scheme [59, 98] (which at the unresummed level coincides with standard $\overline{\text{MS}}$) by using the unresummed or resummed scheme change function as appropriate, and then all calculations are performed in $Q_0\overline{\text{MS}}$. One might hope that most of the residual scheme dependence cancels upon taking the ratio of the NLL and NLO results, at least for schemes that are well defined and without unphysical singularities.

The results for K_2 and K_L are shown in figures 11 for F_2 in the ABF and TW procedures respectively and similarly in figures 12 for F_L . One sees that for x sufficiently small, and for Q not too large, the resummed F_2 is consistently lower than its fixed order counterpart in both approaches, due to the decreased evolution of the gluon, and also (in the $\overline{\text{MS}}$ scheme) due to the fact that resummed coefficient functions are much larger

than the NLO ones at small x and low Q^2 . Similarly the resummed F_L is larger than the fixed order at low Q and small enough x , but falls rapidly as Q increases. However despite these superficial similarities, the two approaches differ quantitatively in several respects:

- the ABF resummed F_2 matches well to the NLO for $x \gtrsim 10^{-2}$ at all scales, while the TW F_2 shows a rise around $x \simeq 10^{-2}$, which is largest at low Q . This may be due to the significant differences between resummed and NLO splitting functions at very high x in fig. 9. A similar mismatch may be seen at $x \sim 0.1$ in the F_L K-factor.
- at large scales the ABF resummation stabilises, due to the running of the coupling, so the K-factors becomes rather flat: they grow only logarithmically in $\ln Q$. By contrast the TW F_2 K-factor still shows a marked Q^2 dependence. This may be related to the fact that the TW resummation does not resum the collinear singularities in the BFKL kernel, and to the TW choice (see Sect. 2.2.3) not to include subtraction of terms induced by the resummation which do not drop at large x . This choice induces a change in the PDFs at higher x in the TW approach, which results in effects which persist to higher Q^2 at smaller x .
- at the initial scale Q_0 the TW resummed F_L grows much more strongly as x decreases than the ABF resummed F_L . This is likely to be due to the different treatment of the coefficient functions: in this respect, the fully consistent treatment of the factorization scheme, the effect of collinear resummation, and the different definitions of what is called resummed NLO used by the two groups all play a part.

2.2.5 Conclusion

The problem of understanding the small x evolution of structure functions in the domain of x and Q^2 values of relevance for HERA and LHC physics has by now reached a status where all relevant physical ingredients have been identified, even though not all groups have quite reached the stage at which the formalism can be transformed into a practical tool for a direct connection with the data.

In this report we summarised the status of the three independent approaches to this problem by ABF, CCSS and TW, we discussed the differences in the adopted procedures and finally we gave some recent results. The most complete formalisms are those by ABF and CCSS while the TW approach is less comprehensive but simpler to handle, and thus has been used in fit to data. We recall that, at the level of splitting functions the ABF and CCSS have been compared in ref. [1] and found to be in very good agreement. The singlet splitting function obtained by TW was also compared with ABF and CCSS in ref. [73] and also found to be in reasonable agreement, at least at small x .

Here we have shown the results of an application to the structure functions F_2 and F_L of the ABF and TW methods. The same input parton densities at the starting scale Q_0 were adopted by these two groups and the K -factors for resummed versus fixed NLO perturbative structure functions were calculated using the respective methods. The results obtained are in reasonable qualitative agreement for F_2 , less so for F_L . Discrepancies may in part be due to the choice of factorization scheme, but our study suggests that the following are also likely to make a quantitative difference: whether or not a resummation of collinear singularities in the BFKL kernel is performed, whether contributions from the resummation which persist at large x are subtracted and whether the factorization scheme is consistently defined in the same way at resummed and NLO levels.

2.3 Parton saturation and geometric scaling²²

2.3.1 Introduction²³

The degrees of freedom involved in hadronic collisions at sufficiently high energy are partons, whose density grows as the energy increases (i.e., when x , their momentum fraction, decreases). This growth of the number of gluons in the hadronic wave functions is a phenomenon which has been well established at HERA. One expects however that it should eventually “saturate” when non linear QCD effects start to play a role.

²²Contributing authors: G. Beuf, F. Caola, F. Gelis, L. Motyka, C. Royon, D. Šálek, A. M. Stašo

²³Contributing authors: F. Gelis, A. M. Stašo

An important feature of partonic interactions is that they involve only partons with comparable rapidities. Consider the interaction between a hadron and some external probe (e.g. a virtual photon in Deep Inelastic Scattering) and consider what happens when one boosts the hadron, increasing its rapidity in successive steps. In the first step, the valence constituents become Lorentz contracted in the longitudinal direction while the time scale of their internal motions is Lorentz dilated. In addition, the boost reveals new vacuum fluctuations coupled to the boosted valence partons. Such fluctuations are not Lorentz contracted in the longitudinal direction, and represent the dynamical degrees of freedom; they are the partons that can interact with the probe. Making an additional step in rapidity would freeze these fluctuations, while making them Lorentz contracted as well. But the additional boost also produces new quantum fluctuations, which become the new dynamical variables. This argument can be repeated, and one arrives at the picture of a high-energy projectile containing a large number of frozen, Lorentz contracted partons (the valence partons, plus all the quantum fluctuations produced in the previous boosts), and partons which have a small rapidity, are not Lorentz contracted and can interact with the probe. This space-time description was developed before the advent of QCD (see for instance [99]; in Bjorken's lectures [100], one can actually foresee the modern interpretation of parton evolution as a renormalization group evolution).

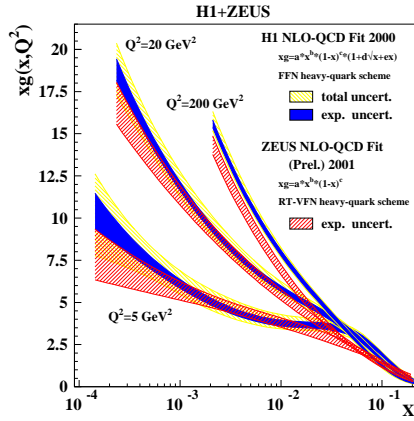


Fig. 13: The gluon structure function in a proton measured at HERA.

not the recombination processes that could reduce the number of gluons (like $gg \rightarrow g$). While it may be legitimate to neglect the recombination process when the gluon density is small, this cannot remain so at arbitrarily high density: a saturation mechanism of some kind must set in. Treating the partons as ordinary particles, one can get a crude estimate of the onset of saturation, which occurs at:

$$Q^2 = Q_s^2, \quad \text{with } Q_s^2 \sim \alpha_s(Q_s^2) \frac{xG(x, Q_s^2)}{\pi R^2}. \quad (21)$$

The momentum scale that characterizes this new regime, Q_s , is called the saturation momentum [107]. Partons with transverse momentum $Q > Q_s$ are in a dilute regime; those with $Q < Q_s$ are in the saturated regime. The saturation momentum increases as the gluon density increases. This comes from an increase of the gluon structure function as x decreases. The increase of the density may also come from the coherent contributions of several nucleons in a nucleus. In large nuclei, one expects $Q_s^2 \propto A^{1/3}$, where A is the number of nucleons in the nucleus.

Note that at saturation, naive perturbation theory breaks down, even though $\alpha_s(Q_s)$ may be small if Q_s is large: the saturation regime is a regime of weak coupling, but large density. At saturation, the gluon occupation number is proportional to $1/\alpha_s$. In such conditions of large numbers of quanta, classical field approximations become relevant to describe the nuclear wave-functions.

Once one enters the saturated regime, the evolution of the parton distributions can no longer be described by a linear equation such as the BFKL equation. The color glass condensate formalism (for a review, see

This space-time picture, which was deduced from rather general considerations, can now be understood in terms of QCD. In fact, shortly after QCD was established as the theory of strong interaction, quantitative equations were established, describing the phenomenon outlined above [42, 101–105]. In particular, the equation derived by Balitsky, Fadin, Kuraev and Lipatov [42, 101] describes the growth of the non-integrated gluon distribution in a hadron as it is boosted towards higher rapidities. Experimentally, an important increase of the number of gluons at small x has indeed been observed in the DIS experiments performed at HERA (see Fig. 13), down to $x \sim 10^{-4}$. Such a growth raises a problem: if it were to continue to arbitrarily small x , it would induce an increase of hadronic cross-sections as a power of the center of mass energy, in violation of known unitarity bounds.

However, as noticed by Gribov, Levin and Ryskin in [106], the BFKL equation includes only branching processes that increase the number of gluons ($g \rightarrow gg$ for instance), but

[108]), which relies on the separation of the degrees of freedom in a high-energy hadron into frozen partons and dynamical fields, as discussed above, provides the non linear equations that allow us to follow the evolution of the partonic systems from the dilute regime to the dense, saturated, regime. For instance, the correlator $\text{tr}\langle U^\dagger(\mathbf{x}_\perp)U(\mathbf{y}_\perp)\rangle$ of two Wilson lines –which enters in the discussion of DIS– evolves according to the Balitsky-Kovchegov [109, 110] equation:

$$\begin{aligned} \frac{\partial \text{tr}\langle U^\dagger(\mathbf{x}_\perp)U(\mathbf{y}_\perp)\rangle_x}{\partial \ln(1/x)} &= -\frac{\alpha_s}{2\pi^2} \int_{\mathbf{z}_\perp} \frac{(\mathbf{x}_\perp - \mathbf{y}_\perp)^2}{(\mathbf{x}_\perp - \mathbf{z}_\perp)^2(\mathbf{y}_\perp - \mathbf{z}_\perp)^2} \\ &\times \left[N_c \text{tr}\langle U^\dagger(\mathbf{x}_\perp)U(\mathbf{y}_\perp)\rangle_x - \text{tr}\langle U^\dagger(\mathbf{x}_\perp)U(\mathbf{z}_\perp)\rangle_x \text{tr}\langle U^\dagger(\mathbf{z}_\perp)U(\mathbf{y}_\perp)\rangle_x \right]. \end{aligned} \quad (22)$$

(This equation reduces to the BFKL equation in the low density limit.)

The geometric scaling phenomenon was first introduced in the context of the dipole picture of the deep inelastic electron-proton scattering [111]. The process of the scattering of the virtual photon on a proton at very small values of x can be conveniently formulated in the dipole model. In this picture the photon fluctuates into the quark-antiquark pair (dipole) and subsequently interacts with the target. In the small x regimes these two processes factorize and they can be encoded into the dipole formula for the total γ^*p cross section

$$\sigma_{T,L}(x, Q^2) = \int d^2\mathbf{r} \int dz |\Psi_{T,L}(r, z, Q^2)|^2 \hat{\sigma}(x, r) \quad (23)$$

where $\Psi_{T,L}$ is the wave function for the photon and $\hat{\sigma}$ is the dipole cross section. r is the dipole size and z is the light-cone fraction of the longitudinal momentum carried by the quark (or antiquark). The photon wave functions Ψ are known, the dipole cross section can be expressed in terms of the correlator of Wilson lines whose evolution is driven by Eq. (22) :

$$\hat{\sigma}(x, r) = \frac{2}{N_c} \int d^2\mathbf{X} \text{tr} \left\langle 1 - U(\mathbf{X} + \frac{\mathbf{r}}{2})U^\dagger(\mathbf{X} - \frac{\mathbf{r}}{2}) \right\rangle. \quad (24)$$

Alternatively, it can be modeled or extracted from the data. In the GBW model it was assumed that the dipole cross section has a form

$$\hat{\sigma} = \sigma_0 \left[1 - \exp(-r^2/R_0(x)^2) \right] \quad (25)$$

where $R_0(x) = (x/x_0)^{-\lambda}$ is a saturation radius (its inverse is usually called the saturation scale $Q_s(x)$) and σ_0 a normalisation constant. One of the key properties of the model was the dependence on the dipole size and the Bjorken x through only one combined variable $r^2 Q_s^2(x)$. This fact, combined with the property of the dipole formula, allows to reformulate the total cross section as a function of $Q^2/Q_s^2(x)$ only. This feature is known as the geometric scaling of the total γ^*p cross section. Initially postulated as a property of the GBW model, it was then shown that the experimental data do indeed exhibit the aforementioned regularity in a rather wide range of Q^2 and for small values of Bjorken x .

Although it is a postulate in the GBW model, this property can be derived from the small- x behavior of the solutions of Eq. (22) [112] : for a wide class of initial conditions, the BK equation drives its solution towards a function that obeys this scaling. Note also that the saturation scale, introduced by hand in the GBW model, is dynamically generated by the non linear evolution described by Eq. (22). This suggested that the regularity seen in the data could be explained by the scaling property of the solutions to the nonlinear equations in the saturated regime - and thus may provide some indirect evidence for gluon saturation.

Nevertheless, several important questions remained. One of them, is the problem of the compatibility of the DGLAP evolution with the property of the geometric scaling. It is known from the global fits that the standard DGLAP evolution works quite well for the description of the of the deep inelastic data even in the very low x and Q^2 regime. That suggests that the saturation should be confined to the very tight kinematic regime, and it is therefore questionable whether the observed regularity could be attributed to the saturation at all. In the present contribution we discuss several approaches to this problem.

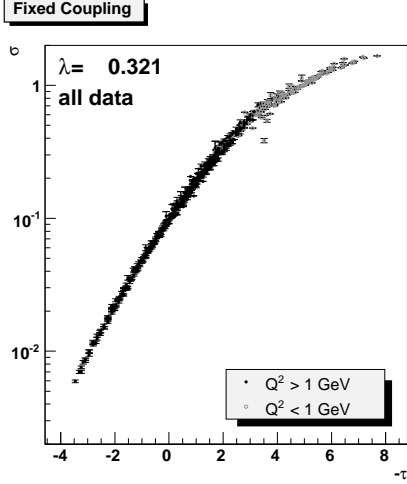


Fig. 14: F_2 data: Scaling curve $\sigma = \sigma(\tau)$ for “Fixed Coupling”. A $Q^2 > 1 \text{ GeV}^2$ cut was applied to the data.

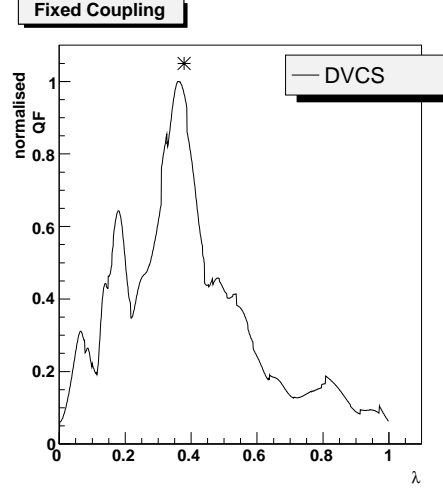


Fig. 15: DVCS data: Quality factor normalised to 1 plotted against the parameter λ . Star denotes the fit result for F_2 data.

2.3.2 Phenomenology²⁴

In order to compare the quality of different scaling laws, it is useful to use a quantity called *quality factor* (QF). It is also used to find the best parameters for a given scaling. In the following, this method is used to compare the scaling results for the proton structure function F_2 and F_2^c , the deeply virtual Compton scattering, the diffractive structure function, and the vector meson cross section data measured at HERA.

Quality Factor Given a set of data points $(Q^2, x, \sigma = \sigma(Q^2, x))$ and a parametric scaling variable $\tau = \tau(Q^2, Y, \lambda)$ (with $Y = \ln 1/x$) we want to know whether the cross-section can be parametrised as a function of the variable τ only. Since the function of τ that describes the data is not known, the QF has to be defined independently of the form of that function.

For a set of points (u_i, v_i) , where u_i 's are ordered and normalised between 0 and 1, we introduce QF as follows [113]

$$QF(\lambda) = \left[\sum_i \frac{(v_i - v_{i-1})^2}{(u_i - u_{i-1})^2 + \epsilon^2} \right]^{-1}, \quad (26)$$

where ϵ is a small constant that prevents the sum from being infinite in case of two points have the same value of u . According to this definition, the contribution to the sum in (26) is large when two successive points are close in u and far in v . Therefore, a set of points lying close to a unique curve is expected to have larger QF (smaller sum in (26)) compared to a situation where the points are more scattered.

Since the cross-section in data differs by orders of magnitude and τ is more or less linear in $\log(Q^2)$, we decided to take $u_i = \tau_i(\lambda)$ and $v_i = \log(\sigma_i)$. This ensures that low Q^2 data points contribute to the QF with a similar weight as higher Q^2 data points.

Fits to F_2 and DVCS Data We choose to consider all available data from H1, ZEUS, NMC and E665 experiments [18, 89–91, 114–117] with Q^2 in the range $[1; 150] \text{ GeV}^2$ and $x < 0.01^{25}$. We exclude the data with $x > 10^{-2}$ since they are dominated by the valence quark densities, and the formalism of saturation does not apply in this kinematical region. In the same way, the upper Q^2 cut is introduced while the lower Q^2 cut ensures that we stay away from the soft QCD domain. We will show in the following that the data points with $Q^2 < 1 \text{ GeV}^2$ spoil the fit stability. Two kinds of fits to the scaling laws are performed, either in the

²⁴Contributing authors: C. Royon, D. Šálek

²⁵The data in the last ZEUS paper include contributions for F_L and $x F_3$ but those can be neglected within the kinematical domain we consider.

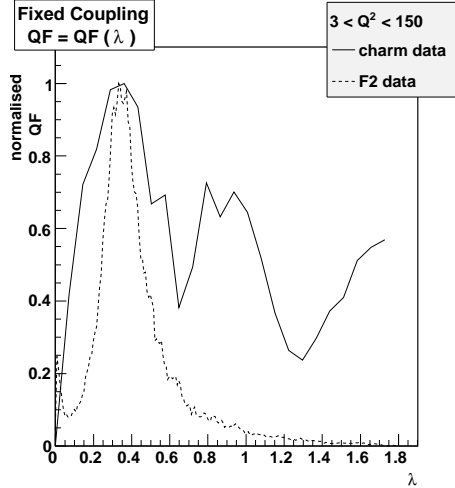


Fig. 16: F_2^c data: Comparison of the λ parameter for F_2 and F_2^c data for $Q^2 > 3 \text{ GeV}^2$.

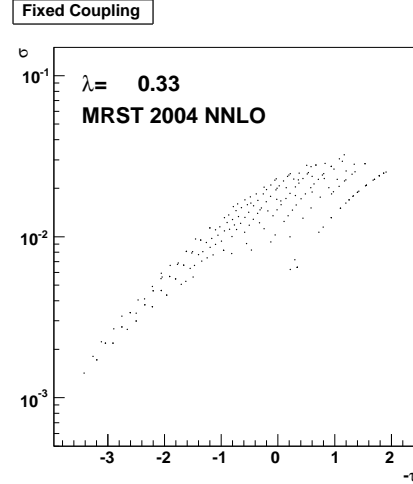


Fig. 17: F_2^c parametrisation: Scaling curve $\sigma = \sigma(\tau)$ for fixed coupling using the MRST 2004 NNLO parametrisation for $\lambda = 0.33$ as obtained in the fit to experimental data. No scaling is observed for $Q^2 > 3 \text{ GeV}^2$.

full mentioned Q^2 range, or in a tighter Q^2 range $[3; 150] \text{ GeV}^2$ to ensure that we are in the domain where perturbative QCD applies.

Figure 14 shows the scaling plot for “Fixed Coupling” in the Q^2 range $[1; 150] \text{ GeV}^2$, which shows that the lowest Q^2 points in grey have a tendency to lead to worse scaling. The QF values are similar for the “Fixed Coupling”, “Running Coupling I”, and “Running Coupling IIbis” — with a tendency to be slightly better for “Running Coupling IIbis” — and worse for diffusive scaling [118].

The amount of the DVCS data [119, 120] measured by H1 and ZEUS is smaller (34 points for H1 and ZEUS requiring $x \leq 0.01$ as for F_2 data), therefore the precision on the λ parameter is weaker. The kinematic coverage of the DVCS data covers smaller region in x and Q^2 than F_2 : $4 < Q^2 < 25 \text{ GeV}^2$ and $5 \cdot 10^{-4} < x < 5 \cdot 10^{-3}$. The DVCS data lead to similar λ values as in the F_2 data (see Fig. 15), showing the consistency of the scalings. The values of the QF show a tendency to favour “Fixed Coupling”, but all different scalings (even “Diffusive Scaling”) lead to reasonable values of QF.

Implications for Diffraction and Vector Mesons We used the values of the parameters obtained from the fit to F_2 data to test the various scaling variables on the diffractive cross section and vector meson data [121–123]. We tested both the fixed β scaling behaviour in x_P and the fixed x_P scaling behaviour in β . At fixed β , we find a scaling behaviour up to $\beta = 0.65$. At fixed x_P , the scaling behaviour of the diffractive cross section as a function of β and Q^2 is far less obvious. This is not a surprise, as not enough data is available in the genuine small β region. A sign of scaling is however observed for the $x_P = 0.03$ bin.

Concerning ρ , J/Ψ , and ϕ production [124–126], we found a reasonable scaling behaviour for all tested scaling variables, with the hard scale $Q^2 + M_V^2$, borrowed from vector mesons wave function studies. Surprisingly, the best scaling is for all three vector mesons the “Diffusive scaling”.

Fits to F_2 and F_2^c in QCD Parametrisations First we test the scaling properties using experimental F_2^c data. The requirements on the kinematical domain remain the same as in the case of F_2 studies. The lower $Q^2 > 3 \text{ GeV}^2$ cut also allows to remove eventual charm mass effects. We use the charm F_2^c measurements from the H1 and ZEUS experiments [127–130]. Only 25 data points lie in the desired kinematical region.

Since the statistics in the data is low, the fit results are not precise. Nevertheless, they still lead to clear results that are comparable to F_2 fits. The results are found similar between F_2 and F_2^c (see Fig. 16). All λ parameters are similar for F_2 and F_2^c except for “Diffusive Scaling”. As in the case of the F_2 scaling

analysis, “Fixed Coupling”, “Running Coupling I” and “Running Coupling II” give similar values of QF , and “Diffusive Scaling” is disfavoured.

The QCD parametrisations [131–133] of the structure function have been tested using CTEQ, MRST, GRV. The same Q^2 and x points as in the experimental data were taken into account. Parametrisations of F_2 are able to reproduce the scaling results seen in the experimental data. However, they are not successful in describing the scaling properties in case of F_2^c . Fig. 17 shows the scaling curve of “Fixed Coupling” in the MRST NNLO 2004 parametrisation of F_2^c where the value of $\lambda = 0.33$ is imposed (as seen in the experimental data). The scaling curve is plotted with all the points used in the F_2 study. Therefore the fact that there is not just a single scaling curve in F_2^c parametrisation is not in direct disagreement with the data — with 25 point only, the curves in parametrisation and data look similar. However the fit values of λ are different.

The CTEQ, MRST or GRV parametrisations are unable to reproduce the scaling properties in F_2^c . It seems a sea-like intrinsic charm component like the one used in CTEQ 6.6 C4 helps to get results closer to a single scaling curve [134]. Scaling is not present at all in the MRST or GRV parametrisations at low Q^2 .

2.3.3 Geometric scaling and evolution equations with saturation²⁶

Let us now recall how scaling properties arise from saturation, as shown in [112], using methods and results from non-linear physics (see [135, 136] for alternative demonstrations). Our discussion, independent of the precise saturation formalism, is valid *e.g.* for the JIMWLK and BK equations (see [108] and references therein), at LL, NLL or even higher order in $\log(1/x)$. We will discuss separately the fixed and the running α_s cases, as running coupling is the main effect which can modify the discussion.

Saturation amounts to add a non-linear damping contribution to the BFKL evolution. One writes formally the evolution equation at LL for the dipole-proton cross section $\hat{\sigma}$ (23)

$$\partial_Y \hat{\sigma}(Y, L) = \bar{\alpha} \chi(-\partial_L) \hat{\sigma}(Y, L) - \text{non-linear terms in } \hat{\sigma}(Y, L), \quad (27)$$

where $Y \equiv \log(1/x)$, $L \equiv -\log(r^2 \Lambda_{QCD}^2)$ and $\chi(\gamma)$ is the characteristic function of the BFKL kernel. The nonlinear damping ensures that, for any Y , $\hat{\sigma}(Y, L)$ grows at most as a power of $|L|$ for $L \rightarrow -\infty$ (*i.e.* $r \rightarrow +\infty$). The color transparency property of the dipole cross section implies $\hat{\sigma}(Y, L) \propto e^{-L}$ for $L \rightarrow +\infty$. Using a double Laplace transform with partial waves $e^{-\gamma L + \omega Y}$, the linear part of (27) reduces to the BFKL dispersion relation $\omega = \bar{\alpha} \chi(\gamma)$, which gives the partial waves solutions $e^{-\gamma[L - \bar{\alpha} \chi(\gamma)Y/\gamma]}$. In the relevant interval $0 < \gamma < 1$, the phase velocity $\lambda(\gamma) = \bar{\alpha} \chi(\gamma)/\gamma$ has one minimum, for the critical value $\gamma = \gamma_c \simeq 0.63$ which is the solution of $\chi(\gamma_c) = \gamma_c \chi'(\gamma_c)$. In the presence of saturation terms in the evolution equation, the wave with $\gamma = \gamma_c$ is selected dynamically.

In order to understand the dynamics of the problem, let us consider an arbitrary initial condition, at some rapidity $Y = Y_0$. With the definition $\gamma_{eff}(L, Y) \equiv -\partial_L \log(\hat{\sigma}(Y, L))$, $\gamma_{eff}(L, Y_0)$ gives the exponential slope of the initial condition in the vicinity of L . That vicinity will then propagates for $Y \geq Y_0$ at a velocity $\lambda(\gamma_{eff}(L, Y)) = \bar{\alpha} \chi(\gamma_{eff}(L, Y))/\gamma_{eff}(L, Y)$. One finds easily that, if $\gamma_{eff}(L, Y_0)$ is a growing function of L , the regions of smaller velocity will spread during the Y evolution, and invade the regions of larger velocity. Restricting ourselves to initial conditions verifying the saturation at $L \rightarrow -\infty$ and the color transparency at $L \rightarrow +\infty$ as discussed previously, one obtains that $\gamma_{eff}(L, Y_0)$ goes from 0 at low L to 1 at large L . At intermediate L , $\gamma_{eff}(L, Y_0)$ will cross the value γ_c , corresponding to the minimal velocity $\lambda_c = \lambda(\gamma_c)$. Hence, one conclude that, as Y grows, there is a larger and larger domain in L where $\gamma_{eff}(L, Y) = \gamma_c$ and thus $\lambda = \lambda_c$. In that domain, one has $\hat{\sigma}(Y, L) \propto e^{-\gamma_c(L - \lambda_c Y)}$, and hence the geometric scaling $\hat{\sigma}(Y, L) \equiv f(L - \lambda_c Y) = f(-\log(r^2 Q_s^2(x)))$, with a saturation scale $Q_s^2(x) = e^{\lambda_c Y} \Lambda_{QCD}^2 = x^{-\lambda_c} \Lambda_{QCD}^2$. One finds that the geometric scaling window is limited to $L < \lambda_c Y + \sqrt{\bar{\alpha} \chi''(\gamma_c) Y}/2$, and separated from the region still influenced by the initial condition by a cross-over driven by BFKL diffusion. So far, we discussed only scaling properties of the dipole cross section $\hat{\sigma}$. As explained in the introduction, they imply similar scaling properties of the virtual photon-proton cross section, with the replacement $r \mapsto 1/Q$.

The mechanism of wave selection explained above happens mainly in the linear regime²⁷, *i.e.* for small

²⁶Contributing author: G. Beuf

²⁷We call linear (non-linear) regime the (Y,L) domain where the explicit value of the non-linear terms in (27) is (is not) negligible compared to the value of the linear terms.

$\hat{\sigma}$, or equivalently r smaller than $Q_s^2(x)$. However, the geometric scaling property stays also valid in the non-linear regime, *i.e.* for r larger than $Q_s^2(x)$, which is reached after a large enough evolution in Y . The only, but decisive, role of saturation in the linear domain is to provide the following dynamical boundary condition in the IR to the linear BFKL evolution: when $\hat{\sigma}$ is large, it should be quite flat ($\gamma_{eff}(L) \simeq 0$). Indeed, one can simulate successfully the impact of saturation on the solution in the linear regime by studying the BFKL evolution in the presence of an absorptive wall [136], set at a Y -dependent and selfconsistently determined position near the saturation scale.

At NLL and higher order level, the terms different from running coupling ones do not affect the previous discussion. They just change the kernel eigenvalues $\chi(\gamma)$ and thus shift the selected parameters γ_c and λ_c . On the contrary, going from fixed to running coupling brings important changes. As the mechanism of spreading of smaller velocity regions of the solution towards larger velocity ones is local, one expect that it holds in the running coupling case. But it selects coupling-dependent velocity and shape of the front, the coupling itself being L -dependent. Hence, the picture is the following. We still have the formation of a specific traveling wave front solution, which progressively loses memory of its initial condition. However, the selected values of the velocity and shape of the front drift as the front propagate towards larger L (smaller r), due to asymptotic freedom. So far, this running coupling case has been solved analytically [112, 136] only at large L and large Y , keeping the relevant geometric scaling variable $-\log(r^2 Q_s^2(x))$ finite. One finds that the evolution is slower than in the fixed coupling case, as the large Y behavior of the saturation scale is now $Q_s^2(x) \sim e^{\sqrt{v_c Y/b}} \Lambda_{QCD}^2$, with $b \equiv (33 - 2N_f)/36$ and $v_c \equiv 2\chi(\gamma_c)/\gamma_c$. In addition, the geometric scaling window is narrower: asymptotically in Y , it is expected to hold only for²⁸ $L < \sqrt{v_c Y/b} + (|\xi_1|/4) (\chi''(\gamma_c))^{1/3} Y^{1/6} / (2b\gamma_c\chi(\gamma_c))^{1/6}$. The convergence of the selected front towards this asymptotic solution seems rather slow, which may weaken its phenomenological relevance. The whole theoretical picture is nevertheless consistent with numerical simulations [137, 138]. Both leads to a universal traveling wave front structure of the solution, implying scaling properties also subasymptotically.

In order to do phenomenological studies, one can try to extrapolate to finite L and Y the scaling behavior found asymptotically. However, this extrapolation is not unique [139]. There is indeed an infinite family of scaling variables

$$\tau_\delta \equiv \left[1 - \left(\frac{v_c Y}{b L^2} \right)^\delta \right] L, \quad (28)$$

parameterized by δ , which are different from each other at finite L and Y but all converge to the same asymptotic scaling previously mentioned. The parameter δ seems quite unconstrained, both from the theory and from the DIS data, as shown in the phenomenological section of the present contribution. We considered as benchmark points in that family two specific choices of δ . The choice $\delta = 1/2$ leads to the only scaling variable of the family which is a genuine geometric scaling variable, *i.e.* is equivalent to a scaling with $r^2 Q_s^2(x)$. It is named *running coupling I* in the phenomenological section. The choice $\delta = 1$ leads to the scaling variable obtained by substitution of the fixed coupling by the running coupling directly in the original fixed coupling geometric scaling variable. It is called *running coupling II*.

Finally, one expects scaling properties in any case from evolution equations with saturation, both in the non-linear regime, and in a scaling window in the linear regime. In the linear regime, the solution still obey the linearized equation, and saturation play only the role of a dynamically generated boundary condition. Hence, geometric scaling there, although generated by saturation, is not a hint against the validity of PDF fits. However, geometric scaling occurs also in the non-linear regime, where the scaling function is no more a solution of the linear BFKL or DGLAP equations.

2.3.4 DGLAP evolution and the saturation boundary conditions²⁹

One of the issues that could be studied in the context of the geometric scaling versus DGLAP evolution is the possibility of the different boundary conditions for the DGLAP evolution equations. These boundary conditions would incorporate the saturation effects and posses the scaling property. Typically, in the standard

²⁸ $\xi_1 \simeq -2.34$ is the rightmost zero of the Airy function.

²⁹Contributing author: A. M. Stašo

approach, to obtain the solution to the linear DGLAP evolution equations, one imposes the initial conditions onto the parton densities at fixed value of Q_0^2 and then performs the evolution into the region of larger values of Q^2 . However, in the presence of saturation these might not be the correct boundary conditions for DGLAP equations. As mentioned earlier the saturation regime is specified by the critical line, the saturation scale $Q_s(x)$ which is a function of x Bjorken and its value increases as the Bjorken x decreases (or as we go to yet higher energies). In that case it seems legitimate to ask, what is the behavior of the DGLAP solutions when evolved from the saturation boundary $Q^2 = Q_s^2(x)$ rather than from the fixed scale $Q^2 = Q_0^2$. To answer this question we imposed [140] the boundary condition for the gluon density at the saturation scale $Q^2 = Q_s^2$ which possesses the scaling property namely $\frac{\alpha_s}{2\pi} xg(x, Q^2 = Q_s^2(x)) = \frac{\alpha_s}{2\pi} r^0 x^{-\lambda}$ (in the fixed coupling case). The solution for the gluon density at small x (at fixed coupling) which can be derived from solving the DGLAP equations with this boundary is given by

$$\frac{\alpha_s}{2\pi} \frac{xg(x, Q^2)}{Q^2} \sim \frac{\alpha_s}{2\pi} \left(\frac{Q^2}{Q_s^2(x)} \right)^{(\alpha_s/2\pi)\gamma_{gg}(\omega_0)-1} \quad (29)$$

where γ_{gg} is the gluon-gluon DGLAP anomalous dimension. This solution clearly has the geometrical scaling property as it is only a function of $Q^2/Q_s^2(x)$. It is interesting to note that there exists a critical value of the exponent λ of the saturation scale which determines the existence of scaling. For example in the double leading logarithmic approximation the scaling is present for rather large values of the exponent $\lambda \geq 4\alpha_s\pi/3$ whereas there is no scaling for smaller values of λ . The formula shown above is however only approximate, as in the derivation we included only the leading behavior which should be dominant at asymptotically small values of x . At any finite value of x the scaling will be mildly violated by the nonleading terms. We checked numerically that this is indeed the case, though the violation was very small. This analysis was extended for the case of the more realistic DGLAP evolution with the running coupling. As expected the presence of the scale violation due to the running coupling will lead to the violation of the scaling. In this case the geometric scaling is only approximate with the solution for the gluon density given by

$$\frac{\alpha_s(Q^2)}{2\pi} \frac{xg(x, Q^2)}{Q^2} \sim \frac{Q_s^2(x)}{Q^2} \left[1 + \frac{\alpha_s(Q_s^2(x))}{2\pi b} \ln[Q^2/Q_s^2(x)] \right]^{b\gamma_{gg}(\lambda)-1},$$

with b being the beta function of the QCD running coupling. The scaling here is present provided we have $\alpha_s(Q_s(x)) \ln[Q^2/Q_s^2(x)]/(2\pi b) \ll 1$. Thus the geometric scaling violating term can be factored out.

In summary, this analysis shows that the geometric scaling property can be build into the DGLAP initial conditions, and that the solution to the linear evolution equation which do not include the parton saturation effects can preserve the scaling even in the regime of high Q^2 values, outside the saturation region.

2.3.5 Geometric scaling from DGLAP evolution³⁰

From the DGLAP point of view there is another possible explanation for geometric scaling: the scaling behaviour can be generated by the evolution itself, rather than being a preserved boundary condition. In fact, it is possible to show [141] both analytically and numerically that in the relevant HERA region approximate geometric scaling is a feature of the DGLAP evolution. In order to see this, one has first to rewrite the DGLAP solution as a function of $t - \lambda(t, x) \log 1/x$ (“fixed-coupling scaling”) or $t - \lambda(t, x) \sqrt{\log 1/x}$ (“running-coupling scaling”)³¹. Then from the explicit form of the DGLAP solution it follows that in the relevant kinematic region $\lambda(t, x)$ is approximatively constant, leading to $\sigma_{DGLAP}(t, x) \approx \sigma_{DGLAP}(t - t_s(x))$. Hence approximate geometric scaling in the HERA region is a feature of the DGLAP evolution. Interestingly enough, this DGLAP-generated geometric scaling is expected to hold also at large Q^2 and relatively large x (say $x \lesssim 0.1$), in contrast with the saturation-based geometric scaling which should be a small x , small (or at least moderate) Q^2 effect.

In order to make more quantitative statements, one can use the quality factor method introduced in Sec. 2.3.2. As a starting point, one can consider the leading-order small x DGLAP evolution of a flat boundary

³⁰Contributing author: F. Caola

³¹The labels “fixed-coupling” or “running-coupling” are here a bit misleading. In fact, all the results shown here are obtained with the full running-coupling DGLAP solution. We kept this notation only for comparison with saturation-based approaches.

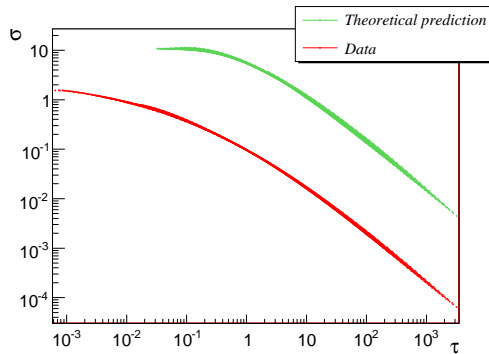


Fig. 18: Scaling plot with $x < 0.1$. For the theoretical DGLAP curve, only points with $Q^2 > 1 \text{ GeV}^2$ were kept. Curves are offset for clarity.

condition. At the level of accuracy of geometric scaling, this approximation should be accurate enough in a wide kinematic region, say $Q^2 \gtrsim 10 \text{ GeV}^2$, $x \lesssim 0.1$ at HERA. Now, a quality-factor analysis shows that in this region the leading-order small x DGLAP solution has an excellent scaling behaviour, even better than the scaling behaviour observed in HERA data. Also the DGLAP predictions for the geometric slope λ perfectly agree with the phenomenological values: from the DGLAP solution we obtain $\lambda_{fix}^{DGLAP} = 0.32 \pm 0.05$ ("fixed-coupling" scaling) and $\lambda_{run}^{DGLAP} = 1.66 \pm 0.34$ ("running-coupling" scaling), to be compared with $\lambda_{fix}^{exp} = 0.32 \pm 0.06$, $\lambda_{run}^{exp} = 1.62 \pm 0.25$. Moreover, data exhibit geometric scaling also for larger x , larger Q^2 (say $x \lesssim 0.1$ at HERA), as predicted by the DGLAP evolution. All these results are summarized in Fig. 18, where we plot the theoretical and phenomenological³² reduced cross sections in function of the "fixed-coupling" scaling variable $\ln \tau = t - \lambda \ln 1/x$, with $\lambda = 0.32$, in the HERA region with the cut $x < 0.1$. An analogous plot can be obtained for the "running-coupling" scaling [141]. We interpret these results as striking evidence that for $Q^2 > 10 \text{ GeV}^2$ the geometric scaling seen at HERA is generated by the DGLAP evolution itself, without need of a peculiar saturation ansatz or of a suitable scaling boundary condition.

For $Q^2 < 10 \text{ GeV}^2$ the leading-order DGLAP solution exhibits violations of geometric scaling at small x . However, in this region any fixed-order DGLAP calculation fails because it does not resum small x logarithms. If one consider the DGLAP evolution at the resummed level, geometric scaling reappears quite naturally, both in the "fixed-coupling" and "running-coupling" forms [141]. Hence, small x resummation extends the region where geometric scaling is expected to values of Q^2 lower than 10 GeV^2 . However at low Q^2 sizeable higher twist and non perturbative effects can spoil the universal behaviour of the DGLAP solution. In this region hence the HERA scaling could still be generated by some DGLAP evolution, but, differently from the $Q^2 > 10 \text{ GeV}^2$ region, here there is no strong evidence that this is in fact the case.

2.3.6 Saturation model and higher twists³³

The QCD description of hard scattering processes within the Operator Product Expansion (OPE) approach leads to the twist expansion of matrix elements of process-dependent composite operators. Contributions of emerging local operators with the increasing twists, τ , are suppressed by increasing inverse powers of the hard scale, Q^2 . In DIS, at the lowest order (i.e. when the anomalous dimensions vanish), the twist- τ contribution to the DIS cross section scales as $Q^{-\tau}$. Therefore, at sufficiently large Q^2 it is justified to neglect higher twist effects, and retain only the leading twist-2 contribution. This leads to the standard collinear factorisation approach with universal parton density functions evolving according to the DGLAP evolution equation. It should be kept in mind, however, that the higher twist effects do not vanish completely and that they introduce corrections to theoretical predictions based on the DGLAP approach. Thus, the higher twist corrections may affect the determination of parton density functions. The importance of these corrections depends on the level of precision required and on the kinematic domain. In particular, in the region of very small x the

³²In fact, in order to make a more flexible analysis, we didn't use the actual HERA data but a neural network interpolation of world DIS data [142]. As long as one stays in the HERA region the output of the net is totally reliable.

³³Contributing author: L. Motyka

higher twist effects are expected to be enhanced, so that they may become significant at moderate Q^2 . Thus, it should be useful to obtain reliable estimates of higher twist effects at small x . In this section we shall present higher twist corrections to F_T , F_L and F_2 structure functions following from the DGLAP improved saturation model [143]. The results presented in this section have been obtained in the course of an ongoing study [144, 145]. The method applied to perform the twist decomposition of the DGLAP improved saturation model is a generalisation of the Mellin space approach proposed in Ref. [146].

A rigorous QCD analysis of the higher twist contributions to DIS at high energies is a complex task. So far it has been performed for the $q\bar{q}gg$ operators [147], but the evolution of twist 4 purely gluonic operators has not been resolved, — even the proper complete basis of the operators has not been found yet. The collinear evolution is known at all twists, however, for so called *quasi-partonic operators*, for which the twist index is equal to the number of partons in the t -channel [148]. Such operators should receive the strongest enhancement from the QCD evolution. At the leading logarithmic approximation the collinear evolution of quasi-partonic operators is relatively simple — it is given by pair-wise interactions between the partons in the t -channel. The interactions are described by the non-forward DGLAP kernel [148]. Within this formalism, the evolution of four-gluon quasi-partonic operators was investigated in Ref. [149, 150] in the double logarithmic approximation. At small x the scattering amplitudes are driven by exchange of gluons in the t -channel, and the quark exchanges are suppressed by powers of x . Thus we shall focus on the dominant contribution of the multi-gluon exchanges in the t -channel. In the large N_c -limit, the dominant singularities of the four gluon operator are those corresponding to states in which gluons get paired into colour singlet states. In other words, the four-gluon operator evolves like a product of two independent gluon densities. In general, for $1/N_c \rightarrow 0$, the $2n$ -gluon (twist- $2n$) operator factorizes into the product of n twist-2 gluon densities. After suitable inclusion of the AGK cutting rules and the symmetry factors of $1/n!$, one arrives at the eikonal picture of n -ladder exchange between the probe and the target. This is to be contrasted with the Balitsky-Kovchegov picture of Pomeron fan diagrams, which was obtained as a result of resummation of the terms enhanced by powers of large $\ln(1/x)$ rather than by powers of $\ln Q^2$.

The eikonal form of the multiple scattering was assumed in the saturation model proposed by Golec-Biernat and Wüsthoff (GBW) [151, 152]. The dipole cross-section given by Eq. 25 has a natural interpretation in terms of a resummation of multiple scattering amplitudes. The scatters are assumed to be independent of each other, and the contribution of n scatterings is proportional to $[r^2/R_0^2(x)]^n$. The connection of the saturation model to the QCD evolution of quasi-partonic operators is further strengthened by the DGLAP improvement of the dipole cross section [143]. In the DGLAP improved saturation model the dipole cross section depends on the collinear gluon density,

$$\hat{\sigma}(x, r) = \sigma_0 \left[1 - \exp \left(-\frac{\pi^2 r^2}{N_c \sigma_0} \alpha_s(\mu^2) x g(x, \mu^2) \right) \right], \quad (30)$$

where the scale μ^2 depends on the dipole size, $\mu^2 = C/r^2$ for $C/r^2 > \mu_0^2$, and $\mu^2 = \mu_0^2$ for $C/r^2 < \mu_0^2$. The gluon density applied has been obtained from the LO DGLAP evolution without quarks, with the input assumed at the scale μ_0^2 ³⁴. Clearly, in Eq. (30) one sees an exact matching between the power of r^2 and the power of $xg(x, \mu^2)$ suggesting a correspondence between the term $\sim [r^2 \alpha_s(\mu^2) xg(x, \mu^2)]^n$ in the expansion of $\hat{\sigma}(x, r)$ and the twist- $2n$ contribution to the dipole cross section. Thus, we expect that the saturation model approximately represents higher twist contributions in the deep inelastic scattering generated by the gluonic quasi-partonic operators.

The twist analysis of the DIS cross-section must include a treatment of the quark box that mediates the coupling of the virtual photon, γ^* , to the t -channel gluons. In the dipole model the $\gamma^*g \rightarrow q\bar{q}$ amplitude, computed within QCD, is Fourier transformed (w.r.t. the transverse momentum of the quark) to the coordinate representation and appears as the photon wave function, compare Eq. (25). In more detail, one uses the γ^*g amplitude computed within the k_T -factorisation framework. This amplitude receives contributions from all twists. The twist structure of the quark box is transparent in the space of Mellin moments, and the same is true

³⁴In the original DGLAP-improved model [143] a different definition of the scale was adopted, $\mu^2 = C/r^2 + \mu_0^2$, but this choice is less convenient for the QCD analysis.

for the dipole cross-section. Thus we define,

$$\tilde{H}_{T,L}(\gamma, Q^2) = \int_0^1 dz \int_0^\infty dr^2 r^2 |\Psi_{T,L}(r, z, Q^2)|^2 r^{2(\gamma-1)}, \quad (31)$$

$$\tilde{\sigma}(x, \gamma) = \int_0^\infty dr^2 \hat{\sigma}(x, r^2) r^{2(\gamma-1)}. \quad (32)$$

It then follows from the Parsival formula that,

$$\sigma_{T,L}(x, Q^2) = \int_{\mathcal{C}} \frac{d\gamma}{2\pi i} \tilde{H}_{T,L}(-\gamma, Q^2) \tilde{\sigma}(x, \gamma). \quad (33)$$

For the massless quark case one has $\tilde{H}_{T,L}(\gamma, Q^2) = \tilde{H}_{T,L}(\gamma) Q^{-2\gamma}$. The contour of integration, \mathcal{C} , in Eq. 33 belongs to the fundamental Mellin strip, $-1 < \text{Re } \gamma < 0$.

In order to obtain the twist expansion of σ , one extends the contour \mathcal{C} in the complex γ -plane into a contour \mathcal{C}' closed from the left-hand side. The Mellin integral in Eq. 33 may be then decomposed into contributions coming from singularities of $\tilde{H}_{T,L}(-\gamma, Q^2) \tilde{\sigma}(x, \gamma)$. The function $\tilde{H}_T(-\gamma)$ ($\tilde{H}_L(-\gamma)$) has simple poles at all negative integer values of γ , except of $\gamma = -2$ ($\gamma = -1$), where \tilde{H}_T (\tilde{H}_L) is regular. The singularity structure of the dipole cross section, $\tilde{\sigma}(\gamma)$, depends on the specific form of $\hat{\sigma}(x, r^2)$. For $\hat{\sigma}(x, r^2)$ used in the GBW model, the $\tilde{\sigma}(x, \gamma)$ has simple poles at all negative integers γ 's. For the DGLAP improved form of $\hat{\sigma}$ given by (31), $\tilde{\sigma}(x, \gamma)$ has cut singularities that extend to the left from $\gamma = k$ where $k = -1, -2, \dots$. The leading behaviour of $\tilde{\sigma}$ around a branch point at $\gamma = k$ is given by $\sim (\gamma - k)^{p(k)}$, where the exponent $p(k)$ is generated by the DGLAP evolution. As the cuts extend to the left from the branch points, the dominant contribution to the cross section at the given twist comes from the vicinity of the corresponding branch point.

The singularity structure of the quark box part $\tilde{H}_{T,L}(\gamma)$ plays the crucial role in understanding the strength of the subleading twist effects. To see that one expands $\tilde{H}_{T,L}(\gamma)$ around the singular points, $\gamma = 1$ and $\gamma = 2$ (recall that the argument of $\tilde{H}_{T,L}$ is $-\gamma$ in the Parsival formula (33)):

$$\tilde{H}_T(\gamma) = \frac{a_T^{(2)}}{\gamma - 1} + b_T^{(2)} + \mathcal{O}(\gamma - 1), \quad H_L(\gamma) = b_L^{(2)} + \mathcal{O}(\gamma - 1), \quad (34)$$

for twist-2, and

$$\tilde{H}_T(\gamma) = b_T^{(4)} + \mathcal{O}(\gamma - 2), \quad H_L(\gamma) = \frac{a_L^{(4)}}{\gamma - 2} + b_L^{(4)} + \mathcal{O}(\gamma - 2), \quad (35)$$

for twist-4. The singular $1/(\gamma - 1)$ and $1/(\gamma - 2)$ terms in (34) and (35) generate an additional enhancement, $\sim \ln(Q^2)$, of the corresponding twist-2 and twist-4 contributions to the DIS cross-section. The constant pieces, proportional to $b_{T,L}^{(2)}$ and $b_{T,L}^{(4)}$, produce no new logarithms (thus they are interpreted as the next-to-leading order (NLO) QCD corrections) and the higher terms in the Laurent expansion give yet higher orders in the perturbative expansion of the $g \rightarrow q$ splitting functions and to the coefficient functions. We summarize this discussion by displaying below the most leading contributions to $\sigma_{T,L}$ at twist-2 ($\sigma_{T,L}^{(2)}$) and at twist-4 ($\sigma_{T,L}^{(4)}$) obtained in the DGLAP improved saturation model:

$$\sigma_T^{(2)} \sim \frac{a_T^{(2)}}{Q^2} \int_{\mu_0^2}^{Q^2} \frac{dQ'^2}{Q'^2} \alpha_s(Q'^2) xg(x, Q'^2), \quad \sigma_L^{(2)} \sim \frac{b_L^{(2)}}{Q^2} \alpha_s(Q^2) xg(x, Q^2), \quad (36)$$

for twist-2, and

$$\sigma_T^{(4)} \sim \frac{b_T^{(4)}}{Q^4} [\alpha_s(Q^2) xg(x, Q^2)]^2, \quad \sigma_L^{(4)} \sim \frac{a_L^{(4)}}{Q^4} \int_{\mu_0^2}^{Q^2} \frac{dQ'^2}{Q'^2} [\alpha_s(Q'^2) xg(x, Q'^2)]^2, \quad (37)$$

for twist-4. These results imply that the the relative twist-4 correction to F_T is strongly suppressed w.r.t. the twist-2 contribution, as the subleading twist-4 term in F_T appears only at the NLO. On the contrary, for F_L ,

the leading twist term enters only at the NLO, and the twist-4 correction enters at the leading order. So, the relative twist-4 effects in F_L are expected to be enhanced. Note, that both in the case of F_T and F_L the twist-4 effects are enhanced w.r.t. the twist-2 contribution by an additional power of the gluon density, $xg(x, Q^2)$. For the structure function $F_2 = F_T + F_L$ we expect small relative corrections from the higher twists because of the opposite sign of coefficients $a_L^{(4)}$ and $b_T^{(4)}$, that leads to cancellations between the twist-4 contributions from F_T and F_L at moderate Q^2 . These conclusions about the importance of the higher twist corrections are expected to be quite general, because they follow directly from the twist structure of the quark box and do not depend on the detailed form of the twist-4 gluon distribution.

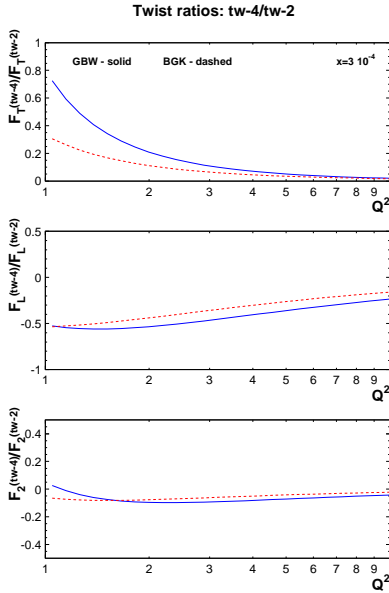


Fig. 19: The ratio of twist-4 to twist-2 components of F_T , F_L and F_2 at $x = 3 \cdot 10^{-4}$ in the GBW model (continuous lines) and in the DGLAP improved saturation model (dashed lines).

to F_2 is 2–4% at $Q^2 = 10 \text{ GeV}^2$, and smaller than 10% for all Q^2 down to 1 GeV^2 . For F_L , the relative correction is $\sim 20\%$ at $Q^2 = 10 \text{ GeV}^2$, and strongly increases with the decreasing scale, reaching $\sim 50\%$ at $Q^2 = 1 \text{ GeV}^2$. It implies that the determination of parton densities from twist-2 F_2 data is safe even at small x and moderate Q^2 . On the other hand F_L at small x may provide a sensitive probe of higher twist effects and parton saturation.

2.3.7 Conclusions

There are many possible explanations for the scaling properties of HERA data, some of them based on saturation effects and some others based on pure linear evolution. In order to separate between these different explanations, it is fundamental to specify a kinematic window.

In particular, for large enough Q^2 and not too small x (say $Q^2 \gtrsim 10 \text{ GeV}^2$ in the HERA region) the observed geometric scaling is determined by the DGLAP evolution, irrespective of the boundary condition. For smaller values of Q^2 , the evolution of parton densities is still linear, but is sensitive to a boundary condition. In an evolution toward smaller x , like BFKL, this boundary condition is dynamically generated by saturation, and it leads to the geometric scaling window. It is possible to take these effects into account also in a Q^2 evolution, like DGLAP, by imposing as initial condition the same boundary condition. We have seen that, in this case, even the LO DGLAP equation is able to propagate geometric scaling towards larger Q^2 . In that domain, although geometric scaling may arise as saturation effect, the evolution is still linear, and thus compatible with standard PDFs analysis. However, at yet lower Q^2 and x standard linear evolution is no longer reliable. In particular, for Q^2 smaller than a x dependent saturation scale $Q_s(x)$, the evolution of parton densities becomes fully nonlinear, and this spoils the actual determination of the PDFs. Results from

We performed [144, 145] an explicit numerical evaluation of the twist-4 corrections to F_T , F_L and F_2 in the DGLAP improved saturation model, and compared the results to results obtained [146] within the GBW model without the DGLAP evolution. The parameters of the DGLAP model were fitted to describe all F_2 data at small x . In the model we took into account three massless quark flavours and the massive charm quark. The twist analysis, however, has been, so far, performed only for the massless quark contribution. The obtained relative twist-4 corrections to F_T , F_L and F_2 are displayed in Fig. 2.3.6, as a function of Q^2 , for $x = 3 \cdot 10^{-4}$. The continuous curves correspond to the GBW model [146], and the dashed ones have been obtained [144, 145] in the DGLAP improved saturation model. Although there are some quantitative differences between the models, the qualitative picture is quite consistent and confirms the results of the analytic analysis outlined above. Thus, the higher twist corrections are strongest in F_L , and much weaker in F_T . In F_2 there occurs a rather fine cancellation between the twist-4 contributions to F_T and F_L , at all Q^2 , down to 1 GeV^2 . Although an effect of this kind was expected, it still remains somewhat surprising that this cancellation works so well. We estimate that, for $x = 3 \cdot 10^{-4}$, the twist-4 relative correction

inclusive diffraction and vector meson exclusive production at HERA, and from dA collisions at RHIC all suggest that in the kinematic accessible x region $Q_s \sim 1 - 2$ GeV.

In conclusion, we can say that for large enough $Q^2 \gtrsim 10$ GeV² geometric scaling is fully compatible with linear DGLAP evolution. For smaller Q^2 the situation becomes more involved. For $Q^2 \gtrsim 5$ GeV² the HERA scaling is still compatible with DGLAP, maybe with some small x resummation or some suitable boundary condition. However, other effects may be relevant in this region. For yet lower Q^2 and x the linear theory becomes unreliable and saturation could be the right explanation for geometric scaling. Unfortunately at HERA we have too few data for a definitive explanation of geometric scaling in the very small x region, since many different approaches lead approximatively to the same results and it is very difficult to separate among them. For example, in the low x region both saturation and perturbative resummations lead to a decrease of the gluon and to geometric scaling. At the LHC, where higher center-of-mass energy is available, the x region is significantly extended down to very small values. Especially in the fragmentation region the typical values of x which can be probed can reach down to 10^{-6} for partons with transverse momenta of about few GeV. This fact combined with the very wide rapidity coverage of the main LHC detectors opens up a completely new window for the study of parton saturation, and its relations with geometric scaling and linear evolution will possibly be clarified.

3 BENCHMARKING OF PARTON DISTRIBUTIONS AND THEIR UNCERTAINTIES³⁵

3.1 Introduction

The proper treatment of uncertainties associated to the fit of Parton Distribution Functions (PDF) has become a subject of great interest in the last few years. A simple way of understanding differences between available approaches to parton fits is to fix some hypothesis (say, experimental data, QCD parameters, input parameterizations, error treatment), and check what is the effect of the remaining assumptions. Such studies were previously done in the framework of the first HERA–LHC workshop [1].

In the following we will discuss three benchmark fits. The first one is presented in Sect. 3.2. It is based on the H12000 parton fit [18], and it compares a new version of this fit, in which uncertainty bands are determined [153, 154] using a Monte Carlo method, to the reference fit, where uncertainty bands are obtained using the standard Hessian method. The main motivation of this benchmark is to study the impact of possible non-Gaussian behaviour of the data and, more generally, the dependence on the error treatment.

The second benchmark is presented in Sect. 3.3. It is based on the study performed by S. Alekhin and R. Thorne in Ref. [1], which compared the fits by their respective groups to a common reduced set of data with common assumptions, and also to their respective reference (global) fits. This comparison is extended here in two ways. First, the comparison is extended to include an NNPDF fit to the same reduced set of data with the same assumptions, and the NNPDF1.0 reference fit [155]. Second, results are also compared to a fit based on the recent MSTW 2008 [39, 156] analysis. As in the Thorne benchmark fit, this uses slightly different data sets and assumptions; it is furthermore modified to use the same input parameterization and improved treatment of uncertainties as MSTW. The main purpose of these comparisons is to answer the questions (a) to which extent fit results from various groups obtained using different methodologies still differ from each other when common or similar assumptions and a common or similar reduced dataset are used and (b) how the fits to the reduced dataset by each group compare to the fit to the full dataset.

The third benchmark, discussed in Sect. 3.4, is a further elaboration on the benchmark presented in Sect. 3.2, extended to include the NNPDF fit, which also uses a Monte Carlo approach. The main purpose of this benchmark is to compare two fits (H1 and NNPDF) which have the same error treatment but different parton parameterizations. The inclusion in this benchmark of the NNPDF fit is also interesting because it allows a comparison of a fit based on a very consistent set of data coming from the H1 collaboration only, to fits which include all DIS data sets, which are less compatible than the H1 sets alone.

3.1.1 Settings for the H1 benchmark

This analysis is based on all the DIS inclusive data by the H1 collaboration from the HERA-I run. A kinematic cut of $Q^2 > 3.5 \text{ GeV}^2$ is applied to avoid any higher twist effect. The data points used in the analysis are summarized in Table 1 and Fig. 20.

The theoretical assumptions are:

- NLO perturbative QCD in the $\overline{\text{MS}}$ renormalization and factorization scheme;
- zero-mass variable flavour number scheme with quark masses $m_c = 1.4 \text{ GeV}$ and $m_b = 4.5 \text{ GeV}$;
- the strong coupling fixed to $\alpha_s(M_Z) = 0.1185$;
- momentum and valence sum rules enforced;
- starting scale for the evolution at $Q_0^2 = 4 \text{ GeV}^2$;
- strange contribution fixed as

$$s(x, Q_0^2) = \bar{s}(x, Q_0^2) = f_s \bar{D}(x, Q_0^2) = \frac{f_s}{1 - f_s} \bar{d}(x, Q_0^2), \quad (38)$$

with $U = u + c$ and $D = d + s + b$ and with $f_s = 0.33$;

- charm contribution fixed as

$$c(x, Q_0^2) = \bar{c}(x, Q_0^2) = f_c \bar{U}(x, Q_0^2) = \frac{f_c}{1 - f_c} \bar{u}(x, Q_0^2), \quad (39)$$

³⁵Contributing authors: R. D. Ball, L. Del Debbio, J. Feltesse, S. Forte, A. Glazov, A. Guffanti, J. I. Latorre, A. Piccione, V. Radescu, J. Rojo, R. S. Thorne, M. Ubiali, G. Watt

Data Set	Data points	Observable	Ref.
H197mb	35	$\tilde{\sigma}^{NC,+}$	[89]
H197lowQ2	80	$\tilde{\sigma}^{NC,+}$	[89]
H197NC	130	$\tilde{\sigma}^{NC,+}$	[157]
H197CC	25	$\tilde{\sigma}^{CC,+}$	[157]
H199NC	126	$\tilde{\sigma}^{NC,-}$	[88]
H199CC	28	$\tilde{\sigma}^{CC,-}$	[88]
H199NChy	13	$\tilde{\sigma}^{NC,-}$	[88]
H100NC	147	$\tilde{\sigma}^{NC,+}$	[18]
H100CC	28	$\tilde{\sigma}^{CC,+}$	[18]
Total	612		

Table 1: Data points used in the H1 benchmark after kinematic cuts of $Q^2 > 3.5 \text{ GeV}^2$.

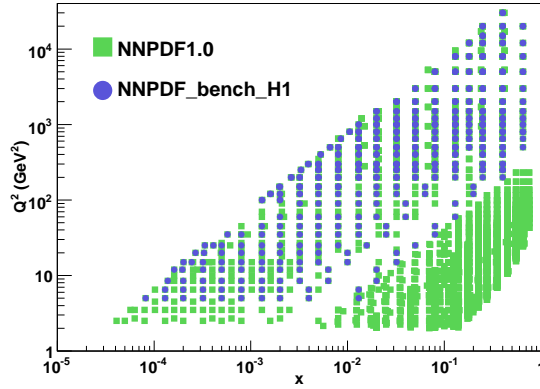


Fig. 20: The data used in the H1 benchmark and in the NNPDF reference fit.

with $f_c = 0.15$;

- five independent PDFs: gluon and U , D , \bar{U} , \bar{D} (see definition above);
- iterated solution for evolution (see, e.g. [158], Sect. 1.3).

Both the H1 and NNPDF methodologies are based on

- Monte Carlo method to determine uncertainties. This method will be discussed in detail in Sect. 3.2.2 below.

They differ in the way PDFs are parameterized:

- H1 parameterizes PDFs as

$$\begin{aligned}
 xg(x, Q_0^2) &= A_g x^{B_g} (1-x)^{C_g} [1 + D_g x], \\
 xU(x, Q_0^2) &= A_U x^{B_U} (1-x)^{C_U} [1 + D_U x + F_U x^3], \\
 xD(x, Q_0^2) &= A_D x^{B_D} (1-x)^{C_D} [1 + D_D x], \\
 x\bar{U}(x, Q_0^2) &= A_{\bar{U}} x^{B_{\bar{U}}} (1-x)^{C_{\bar{U}}}, \\
 x\bar{D}(x, Q_0^2) &= A_{\bar{D}} x^{B_{\bar{D}}} (1-x)^{C_{\bar{D}}},
 \end{aligned} \tag{40}$$

which yields 10 free parameters after sum rules are imposed;

- NNPDF parameterizes PDFs with a 2-5-3-1 neural network, which implies 185 free parameters to be fitted.

Because of the large number of parameters, the minimum of the NNPDF fit is determined using the stopping criterion discussed in Sect. 3.3.2 below, while the minimum of the H1 fit is determined as the standard minimum χ^2 (or maximum likelihood) point of parameter space.

3.1.2 Settings for the HERA–LHC benchmark

This benchmark was first presented in Ref. [1], where its settings were defined. In order to have a conservative ensemble of experimental data and observables, only structure function DIS data are used. Large kinematic cuts are applied to avoid any higher twist effect. The data points used in the Alekhin analysis are summarized in Table 2 and Fig. 21.

Data Set	Data points	Observable	Ref.
ZEUS97	206	F_2^p	[91]
H1lowx97	77	F_2^p	[89]
NMC	95	F_2^p	[116]
NMC_pd	73	F_2^d/F_2^p	[159]
BCDMS	322	F_2^p	[160]
Total	773		

Table 2: Data points used in the HERA–LHC benchmark after kinematic cuts of $Q^2 > 9 \text{ GeV}^2$ and $W^2 > 15 \text{ GeV}^2$ are applied.

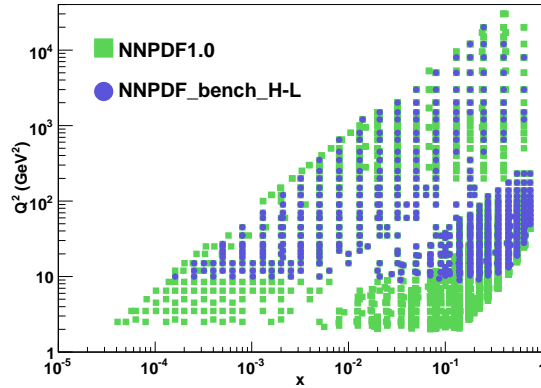


Fig. 21: The data used in the HERA–LHC benchmark and in the NNPDF reference fit.

The theoretical assumptions are:

- NLO perturbative QCD in the $\overline{\text{MS}}$ renormalization and factorization scheme;
- zero-mass variable flavour number scheme with quark masses $m_c = 1.5 \text{ GeV}$ and $m_b = 4.5 \text{ GeV}$;
- $\alpha_s(M_Z)$ fitted: the best-fit values are 0.1110 ± 0.0012 (Alekhin) and 0.1132 ± 0.0015 (Thorne);
- momentum and valence sum rules imposed;
- starting scale for evolution $Q_0^2 = 1 \text{ GeV}^2$;
- four independent input PDFs (u and d valence, the sea and the gluon);
- no light sea asymmetry: $\bar{u} = \bar{d}$;
- no independent strange PDF:

$$s(x, Q_0^2) + \bar{s}(x, Q_0^2) = 0.5(\bar{u}(x, Q_0^2) + \bar{d}(x, Q_0^2)); \quad (42)$$

- iterated solution of evolution equations;

The NNPDF analysis presented here is based on the same data set and theoretical assumptions, the only difference being that the strong coupling is fixed to $\alpha_s(M_Z) = 0.112$, i.e. the average of the fitted values of S. Alekhin and R. Thorne.

The Thorne benchmark used somewhat different data sets and assumptions. Namely:

Data Set	Data points	Observable	Ref.
ZEUS97	206	$\tilde{\sigma}^{\text{NC},+}$	[91]
H1lowx97	86	$\tilde{\sigma}^{\text{NC},+}$	[89]
NMC	67	F_2^p	[116]
NMC_pd	73	F_2^d/F_2^p	[159]
BCDMS	157	F_2^p	[160]
Total	589		

Table 3: Data points used in the MSTW benchmark fit after kinematic cuts of $Q^2 > 9 \text{ GeV}^2$ and $W^2 > 15 \text{ GeV}^2$ are applied.

- A somewhat different dataset is used, as displayed in Table 3. This differs from the dataset of Table 2 and Figure 2 because the NMC and BCDMS fixed-target data on F_2^p used are averaged over different beam energies, and also, HERA reduced cross sections rather than structure function data are used, resulting in an additional nine H1 points. Note that the Thorne benchmark in Ref. [1] also included the F_2^d BCDMS deuterium data.
- All correlations between systematics are neglected, and statistical and systematic errors are added in quadrature.
- Normalizations of individual data sets are fitted with a rescaling of uncertainties to avoid systematic bias.
- The F_2^d/F_2^p data are corrected for nuclear shadowing effects [161].

The MSTW analysis presented here makes the same choices as the Thorne benchmark, but with $\alpha_s(M_Z) = 0.112$, and additionally

- a global correction of -3.4% is applied to the luminosity of the published H1 MB 97 data [89] following a luminosity reanalysis [162].
- a quartic penalty term in the χ^2 definition is given to normalizations which deviate from the central value.

3.2 Experimental Error Propagation³⁶

3.2.1 Introduction

Standard error estimation of proton parton distribution functions (PDFs) relies on the assumption that all errors follow Gaussian (or normal) statistics. However, this assumption may not always be correct. Some systematic uncertainties such as luminosity and detector acceptance follow rather a log-normal distribution (see Section 4.1). Compared to the Gaussian case, the lognormal distribution which has the same mean and root mean square (RMS), is asymmetric and has a shifted peak, as shown illustratively in Figure 22. Therefore, the non-Gaussian behaviour of the experimental uncertainties could lead to an additional uncertainty of the resulting PDFs. An alternative to the standard error propagation is a toy Monte Carlo (MC) method. Here, an implementation of the MC method is presented for estimation of the PDF uncertainties with various assumptions for the error distribution. In addition, this MC method provides an independent cross check of the standard error propagation when assuming the Gaussian error distributions.

3.2.2 Method

The Monte Carlo technique consists firstly in preparing replicas of the initial data sets which have the central value of the cross sections, σ_i , fluctuating within its systematic and statistical uncertainties taking into account all point to point correlations. Various assumptions can be considered for the error distributions. When dealing with the statistical and point to point uncorrelated errors, one could allow each data point to randomly fluctuate within its uncorrelated uncertainty assuming either Gauss, lognormal, or any other desired form of the error distribution. For example, for Gaussian errors

$$\sigma_i \longrightarrow \sigma_i (1 + \delta_i^{\text{uncorr}} \cdot R_i), \quad (43)$$

³⁶Contributing authors: J. Feltesse, A. Glazov, V. Radescu

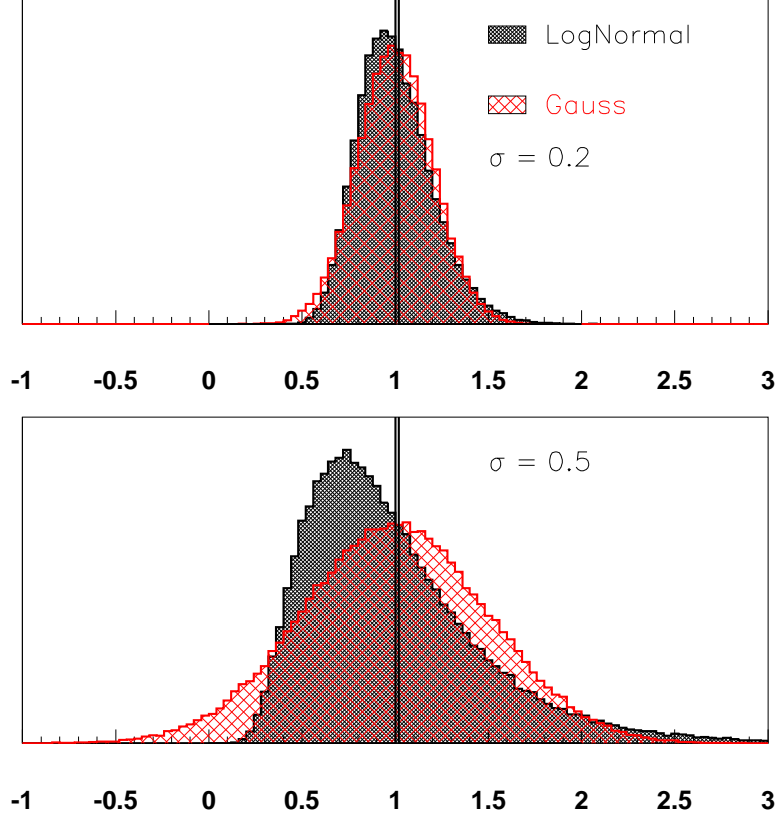


Fig. 22: Comparison of the lognormal (black, darker hatching) and Gaussian (red, lighter hatching) probability distributions. The distributions are shown with mean equal to one, and two different choices for the RMS (for both distribution): $\sigma = 0.2$ (top) and $\sigma = 0.5$.

where δ_i^{uncorr} corresponds to the uncorrelated uncertainties and R_i is a random number chosen from a normal distribution with a mean of 0 and a standard deviation of 1. Hence, the central value of each cross section point i is shifted by $\delta_i^{uncorr} \cdot R_i$.

For the systematic errors, the treatment is a bit more complicated than above. This is due to the correlation between data points and that, in general, the data points are sensitive to the systematic sources with a different strength δ_{ij} , where index i (j) runs over all the cross section points (all systematic sources). In order to take this into account, for each systematic source j a uniformly distributed *fluctuation probability* P_j is selected. Then, for each data point i the central value of cross section is shifted such that probability of this shift, which depends on δ_{ij} and the exact form of the probability distribution function, is equal P_j (for positive δ_{ij}) or $(1 - P_j)$ (for negative δ_{ij}). In other words, each central value of the cross section is shifted with the same probability of the corresponding systematic shift. For example for the Gaussian errors, this procedure is equivalent to

$$\sigma_i \longrightarrow \sigma_i \left(1 + \delta_i^{uncorr} \cdot R_i + \sum_j^{N_{sys}} \delta_{ij}^{corr} \cdot R_j \right), \quad (44)$$

where in addition to the shifts for the uncorrelated errors previously explained, R_j corresponds to another random number chosen from a normal distribution with mean of 0 and standard deviation of 1 as a fluctuation for the systematic source j . Hence, the central values of the cross sections are shifted in addition by $\delta_{ij}^{corr} \cdot R_j$ for each systematic shift.

This preparation of the data is repeated for N times, where high statistics is desirable for more accurate results. For this study we used $N > 100$ which proved to suffice. For each replica, a next to leading order (NLO) QCD fit is performed to extract the PDFs. The errors on the PDFs are estimated from the RMS of the

spread of the N lines corresponding to the N individual fits to extract PDF.

A fit to the published H1 HERA-I data of neutral and charged current $e^\pm p$ scattering cross sections [18] using the settings discussed in Sect. 3.1.1 has been performed, using the QCDNUM program [163].

3.2.3 Validation of the Method

The MC method is tested by comparing the standard error estimation of the PDF uncertainties with the MC techniques by assuming that all the errors (statistical and systematic) follow Gaussian (normal) distribution. Figure 23 shows good agreement between the methods.

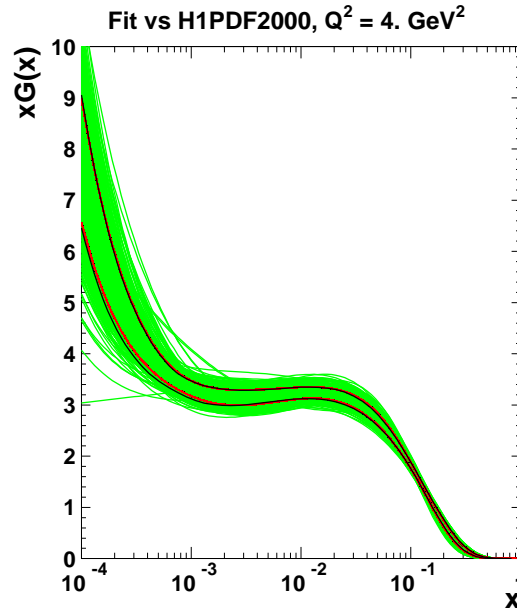


Fig. 23: Comparison between the standard error calculations and the Gauss error distribution is shown for the gluon PDF. Green lines represent the spread of Monte Carlo generated allowances for the errors, and the red lines are the RMS of this spread. The black lines correspond to the standard error calculations of the PDF errors.

3.2.4 Test of various assumptions for the error distributions

Two cases are considered which may represent most likely the error distributions: (1) the lognormal distribution for the luminosity uncertainty and the rest of the errors are set to follow the Gauss shape, (2) the lognormal distributions for all the systematic errors and the statistical errors are set to follow the Gauss distributions. The results for the first case (1) are shown in Figure 24. The results of the tests for the case when lognormal distributions for all the systematic uncertainties are assumed is shown in Figure 24. We observe that for the precise H1 HERA-1 data the effect of using lognormal distribution, which is considered for some systematic uncertainties more physical, is similar to the pure gauss distribution case.

3.2.5 Conclusions

A simple method to estimate PDF uncertainties has been built within QCD Fit framework. Assuming only gauss distribution of all errors, the results agree well with the standard error estimation. This method allows to check the effect of non- gauss assumptions for distributions of the experimental uncertainties. For the H1 data, results are similar to the gauss case when using lognormal. The method could be extended for other physical variables (i.e. cross sections) for cross checks with the standard error evaluation.

3.3 HERA–LHC Benchmark

This benchmark is based on the Alekhin/Thorne benchmark of Ref. [1], whose settings has been given in Sect. 3.1.2. Both the Alekhin and Thorne fits had the following features:

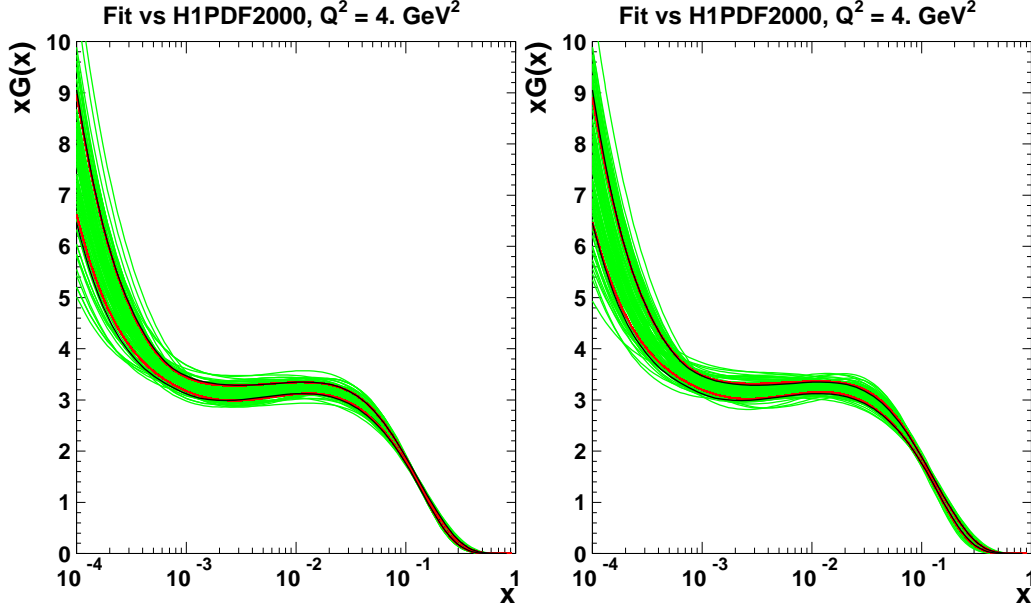


Fig. 24: Comparison between errors on PDFs obtained via standard error calculation (black) where Gauss assumption is used, and errors obtained via Monte Carlo method (red) where luminosity uncertainty is allowed to fluctuate according to lognormal distributions and all the other uncertainties follow the Gaussian distribution (left), and where all the systematic uncertainties are allowed to fluctuate according to lognormal distributions (right). Only the gluon PDF is shown, where the errors are larger. The green lines show the spread of the N individual fits.

- uncertainties determined using the Hessian method with $\Delta\chi^2 = 1$;
- input PDFs are parameterized using the following functional form:

$$x f_i(x, Q_0^2) = A_i (1-x)^{b_i} (1 + \epsilon_i x^{0.5} + \gamma_i x) x^{a_i}. \quad (45)$$

with ϵ_i and γ_i set to zero for the sea and gluon distributions. Hence, there were a total of 13 free PDF parameters plus $\alpha_s(M_Z)$ after imposing sum rules.

Here, we reanalyze it within the MSTW and NNPDF approaches. First, we summarize the respective MSTW and NNPDF approaches, and especially their differences when compared to the previous HERALHC benchmark fits of Ref. [1]. Then, results for benchmark fits obtained with the various different approaches are compared to each other. Finally, we compare each benchmark fit to its counterpart based on a wider range of data, i.e. the NNPDF1.0 [155] reference and the MRST01 [164] and MSTW08 [39, 156] PDFs.

3.3.1 MSTW approach³⁷

The benchmark analysis is now much more closely aligned to the global analysis than was the case for the Thorne benchmark compared to the MRST global analysis. It follows the general approach taken by the MRST (or more recently, MSTW) group, and is similar to that described in Ref. [164]. There are some new features which are explained below.

- *Input parameterization.* We take the input PDF parameterization at $Q_0^2 = 1 \text{ GeV}^2$ to be:

$$x u_v(x, Q_0^2) = A_u x^{\eta_1} (1-x)^{\eta_2} (1 + \epsilon_u \sqrt{x} + \gamma_u x), \quad (46)$$

$$x d_v(x, Q_0^2) = A_d x^{\eta_3} (1-x)^{\eta_4} (1 + \epsilon_d \sqrt{x} + \gamma_d x), \quad (47)$$

$$x S(x, Q_0^2) = A_S x^{\delta_S} (1-x)^{\eta_S} (1 + \epsilon_S \sqrt{x} + \gamma_S x), \quad (48)$$

$$x g(x, Q_0^2) = A_g x^{\delta_g} (1-x)^{\eta_g} (1 + \epsilon_g \sqrt{x} + \gamma_g x) + A_{g'} x^{\delta_{g'}} (1-x)^{\eta_{g'}}, \quad (49)$$

³⁷Contributing authors: R. S. Thorne, G. Watt

where $S = 2(\bar{u} + \bar{d} + \bar{s})$, $s = \bar{s} = 0.1 S$ and $\bar{d} = \bar{u}$. The parameters A_u , A_d and A_g are fixed by sum rules, leaving potentially 19 free parameters. In practice, to reduce the number of highly correlated parameters, making linear error propagation unreliable, we determine the central value of the benchmark fit by freeing all 19 parameters, then fix 6 of those at the best-fit values when calculating the Hessian matrix used to determine the PDF uncertainties, giving a total of 13 eigenvectors. This is the same procedure as used in the MSTW 2008 global fit [39, 156], where there are an additional 3 free parameters associated with $\bar{d} - \bar{u}$ and an additional 4 free parameters associated with strangeness, giving a total of 20 eigenvectors. Note that the parameterization used in the previous Alekhin/Thorne benchmark fits was considerably more restrictive, where the ϵ_S , γ_S , ϵ_g and γ_g parameters were set to zero, and the second (negative) gluon term was omitted entirely. In addition, ϵ_u was held fixed for the Thorne benchmark fit, leaving a total of 12 eigenvectors. We find that the more flexible gluon parameterization, allowing it to go negative at very small x , is very highly correlated with the value obtained for α_s , and a value of $\alpha_s(M_Z) = 0.105$ is obtained if it is allowed to go free at the same time as the other parameters, therefore we instead choose to fix it at $\alpha_s(M_Z) = 0.112$ as in the NNPDF benchmark fit.

- *Error propagation.* Apart from the more flexible input parameterization, the other major difference in the new MSTW version of the HERA–LHC benchmark fit, with respect to the previous Thorne (MRST) version, is the choice of tolerance, $T = \sqrt{\Delta\chi^2}$. The MRST benchmark fit used the standard choice $T = 1$ for one-sigma uncertainties. More precisely, the distance t along each normalized eigenvector direction was taken to be 1, and ideal quadratic behaviour about the minimum was assumed, giving $T \approx t = 1$. The MRST global fit used $T = \sqrt{50}$ for a 90% confidence level (C.L.) uncertainty band; however, this is not appropriate when fitting a smaller number of data sets. Recently, a new procedure has been developed [39, 156] which enables a *dynamic* determination of the tolerance for each eigenvector direction, by demanding that each data set must be described within its one-sigma (or 90%) C.L. limits according to a hypothesis-testing criterion, after rescaling the χ^2 for each data set so that the value at the global minimum corresponds to the most probable value. Application of this procedure to the MSTW benchmark fit gives $T \sim 3$ for one-sigma uncertainties and $T \sim 5$ for 90% C.L. uncertainties. For the MSTW global fit, the typical values of T required are slightly larger, with more variation between different eigenvector directions. The increase in T in the global fit is mainly due to the inclusion of some less compatible data sets, while the greater variation in T between eigenvectors is due to the fact that some parameters, particularly those associated with s and \bar{s} , are constrained by far fewer data sets than others. In the MSTW fits, the data set normalizations are allowed to vary, with the aforementioned penalty term, when determining the PDF uncertainties. For global fits this automatically leads to a small increase in uncertainty compared to the MRST determinations, where data set normalisations were held fixed when calculating the Hessian matrix used for error propagation. In the MRST benchmark fit the data set normalizations were allowed to vary. To calculate the uncertainty bands from the eigenvector PDF sets, we use the formula for asymmetric errors given, for example, in Eq. (13) of Ref. [164].

3.3.2 NNPDF approach³⁸

The NNPDF approach was proposed in Ref. [165], and it was applied there and in Ref. [142] to the parameterization of the structure function $F_2(x, Q^2)$ with only two or more experimental data sets respectively. In Ref. [166] it was first used for the determination of a single PDF (the isotriplet quark distribution), and in Ref. [155] a full set of PDFs fit based on DIS data (NNPDF1.0) was presented. Because the method has been discussed extensively in these references, here we only summarize briefly its main features.

- *Error propagation.* We make a Monte Carlo sample of the probability distribution of the experimental data by generating an ensemble of N replicas of artificial data following a multi-gaussian distribution centered on each data point with full inclusion of the experimental covariance matrix. Each replica is used to construct a set of PDFs, thereby propagating the statistical properties of the data Monte Carlo sample to a final Monte Carlo sample of PDFs. Here we shall take $N = 100$. The method is the same as discussed in Sect. 3.2.2, the only difference being the treatment of normalization errors: relative

³⁸Contributing authors: R. D. Ball, L. Del Debbio, S. Forte, A. Guffanti, J. I. Latorre, A. Piccione, J. Rojo, M. Ubiali

normalizations are fitted in the H1 approach, while they are included among the systematic errors in the Monte Carlo data generation in the NNPDF approach (see Refs. [18, 155] for details of the respective procedures) .

- *Input parameterization.* Each PDF is parameterized with a functional form provided by a neural network. The architecture for the neural network is the same for all PDFs, and yields a parameterization with 37 free parameters for each PDF. This is a very redundant parameterization, it is chosen in order to avoid parameterization bias; neural networks are a particularly convenient way of dealing with redundant parameterizations. Note that sum rules are also imposed.
- *Minimization.* A redundant parameterization allows for fitting not only the underlying physical behaviour, but also statistical noise. Therefore, the minimization is stopped not at the absolute minimum of the χ^2 , but rather before one starts fitting noise. This optimal stopping point is determined as follows: the data in each replica are randomly assigned either to a training or to a validation set. The fit is performed on data of the training set only, while the validation set is used as a monitor. The fit is stopped when the quality of the fit to the training set keeps improving, but the quality of the fit to the validation set deteriorates.

3.3.3 Comparison between the Benchmark Parton Distributions

Data Set	$\chi_{\text{bench}}^2/N_{\text{data}}$	$\chi_{\text{global}}^2/N_{\text{data}}$
ZEUS97	1.09	1.18
H1lowx97	1.03	1.00
NMC	1.40	1.45
NMC_pd	1.24	1.32
BCDMS	1.21	1.98
Total	1.19	1.53

Table 4: NNPDF χ^2 for the total and each single data set, both for the benchmark and global fit.

Data set	$\chi_{\text{bench}}^{\text{diag } 2}/N_{\text{data}}$	$\chi_{\text{global}}^{\text{diag } 2}/N_{\text{data}}$
ZEUS97	0.76	0.79
H1lowx97	0.53	0.54
NMC	1.08	1.11
NMC_pd	0.78	0.89
BCDMS	0.74	1.13
Total	0.76	0.89

Table 5: MSTW χ^2 for the total and each single data set, both for the benchmark and global fit. Notice that statistical and systematic errors are added in quadrature and that relative data set normalizations are fitted.

The χ^2 per data point for the NNPDF and MSTW fits are shown in Table 4 and 5 respectively. Note that in the MSTW fit statistical and systematic errors are added in quadrature, so the quantity shown is the diagonal contribution to the χ^2 . The quality of the NNPDF is seen to be uniformly good. The quality of the MSTW is also uniform, though it cannot be compared directly because of the different way systematics are treated. The comparison of each benchmark fit to the corresponding global fit will be discussed in Sect. 3.3.4 below.

In Fig. 25 the PDFs from the NNPDF and MSTW benchmark fits presented here are compared to those by Thorne from Ref. [1] at the same reference scale of $Q^2 = 20 \text{ GeV}^2$ used there (denoted as MRST01 in the figure). The benchmark fit by Alekhin [1] is not shown as the PDFs are very close to the those by Thorne displayed in Fig. 25.

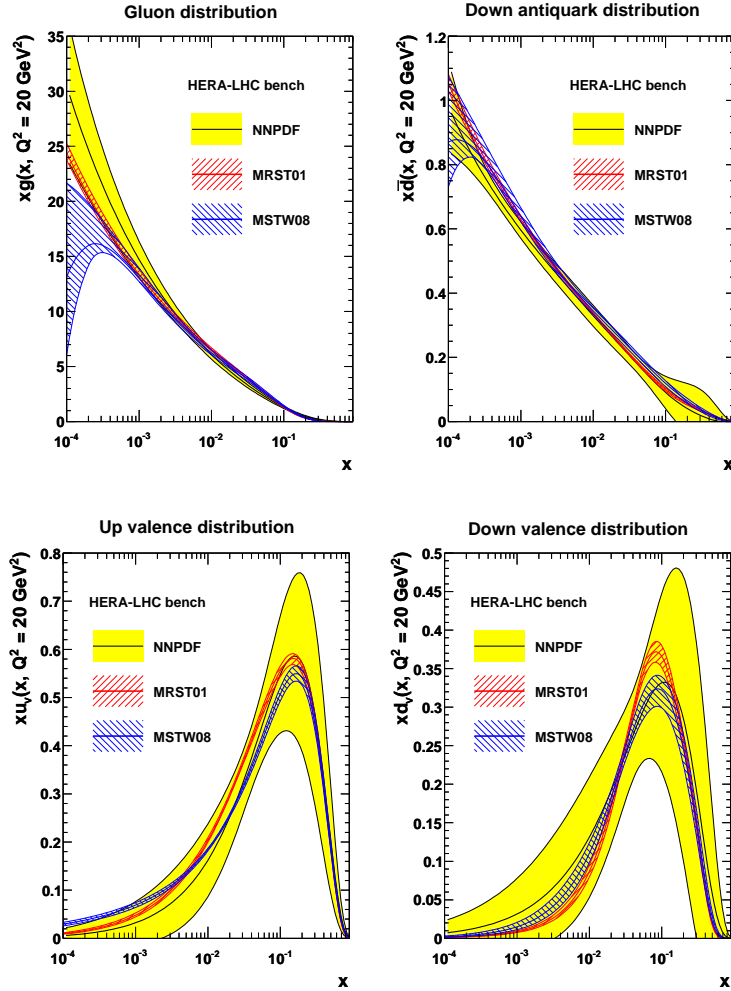


Fig. 25: Comparison of the NNPDF, MRST and MSTW benchmark fits for the gluon, d -sea, u -valence and d -valence at $Q^2 = 20 \text{ GeV}^2$. All uncertainties shown correspond to one- σ bands.

For PDFs and kinematical regions where data are available, namely the small- x gluon and sea quark and the large- x u_v distributions, the central values of the NNPDF fit are quite close to those of the MRST and MSTW fits, despite the differences in methodology. The central values of the PDFs are slightly different for the MRST and MSTW benchmark fits due to the use of BCDMS F_2^d data in the former, which affects mainly valence quarks. Where extrapolation is needed, such as for the d_v distribution, which is constrained only by the small amount of data on the ratio F_2^d/F_2^p , or the large- x sea quark, central values are rather more different (though the Alekhin/MRST/MSTW benchmark central values are within the NNPDF error band). The exception is the smallest- x gluon, where the form of the MSTW parameterization results in a very sharp turn-over. However, even here the uncertainty bands are close to overlapping.

Differences are sizeable in the estimation of uncertainties. Firstly, uncertainty bands for NNPDF benchmark are significantly larger than for the MSTW benchmark, which in turn are in general somewhat larger than those for the MRST benchmark. The difference between MRST and MSTW, which are based on similar methodology, is due to use of a dynamic tolerance and a more flexible gluon parameterization in MSTW (see Sect. 3.3.1). Secondly, the width of the uncertainty band for NNPDF benchmark varies rather more than that of the MRST benchmark according to the PDF and the kinematic region, though this is not quite so much the case comparing to MSTW benchmark. Indeed, the NNPDF uncertainties are quite small in the region between $x = 0.01$ and $x = 0.1$ (where there is the bulk of HERA and fixed-target data), while they blow up in the large- x region for the sea quark or the small- x gluon, where there is less or no experimental information. The smallness of the uncertainty band for MSTW for the small- x valence quarks may be partially due to the lack of flexibility in the parameterization: note that because of sum rules, the size of uncertainties in the data and

extrapolation region are correlated.

Finally, the MRST/MSTW central value generally falls within the NNPDF uncertainty band, but the NNPDF central value tends to fall outside the MRST/MSTW uncertainty band whenever the central values differ significantly.

3.3.4 Comparison of the Benchmark Parton Distributions and Global Fits

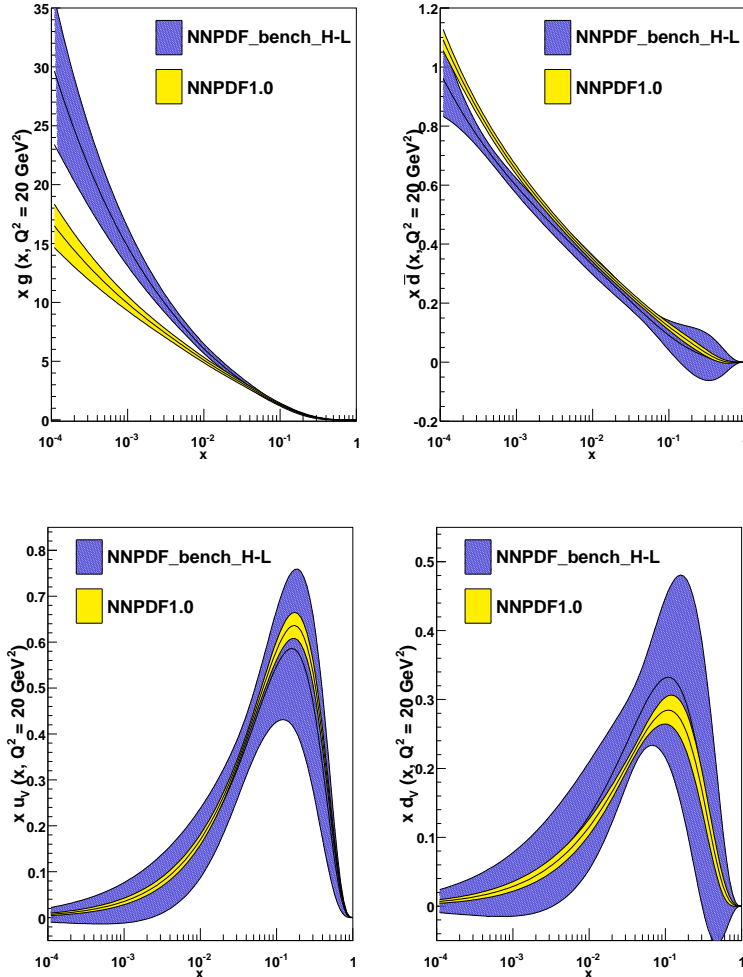


Fig. 26: Comparison of the NNPDF benchmark and reference fits for the gluon, d -sea, u -valence and d -valence at $Q^2 = 20 \text{ GeV}^2$.

In Fig. 26 we compare the NNPDF benchmark fit to the NNPDF1.0 reference fit of Ref. [155] (NNPDF global, henceforth), while in Fig. 27 we compare the MSTW benchmark fit to the MRST01 [164] (MRST global, henceforth) and MSTW08 [39, 156] global fits (MSTW global, henceforth).

The χ^2 of the NNPDF benchmark and global fits are compared in Table 4, while those of the MSTW benchmark and global fits are compared in Table 5. Note that for the NNPDF fits the χ^2 is computed using the full covariance matrix, while for the MSTW fits systematic and statistical uncertainties are added in quadrature. Note also that the MRST and MSTW global fits are carried out in a general-mass variable flavour number scheme rather than the zero-mass variable flavour number scheme used in the corresponding benchmark fits, whereas for NNPDF both global and benchmark fits are done with a zero-mass variable flavour number scheme. Comparison of the quality of each benchmark to the corresponding global fit to the same points in Table 5 shows a significant deterioration in the quality of the fit (total $\Delta\chi^2 \gg 1$), especially for the BCDMS F_2^D data. All fits appear to be acceptable for all data sets: for instance, even though the χ^2 of the NNPDF global fit for the benchmark subset of data is 1.98, it is equal to 1.59 [155] for the full BCDMS set of data. However, the increase in χ^2 suggests that there might be data inconsistencies.

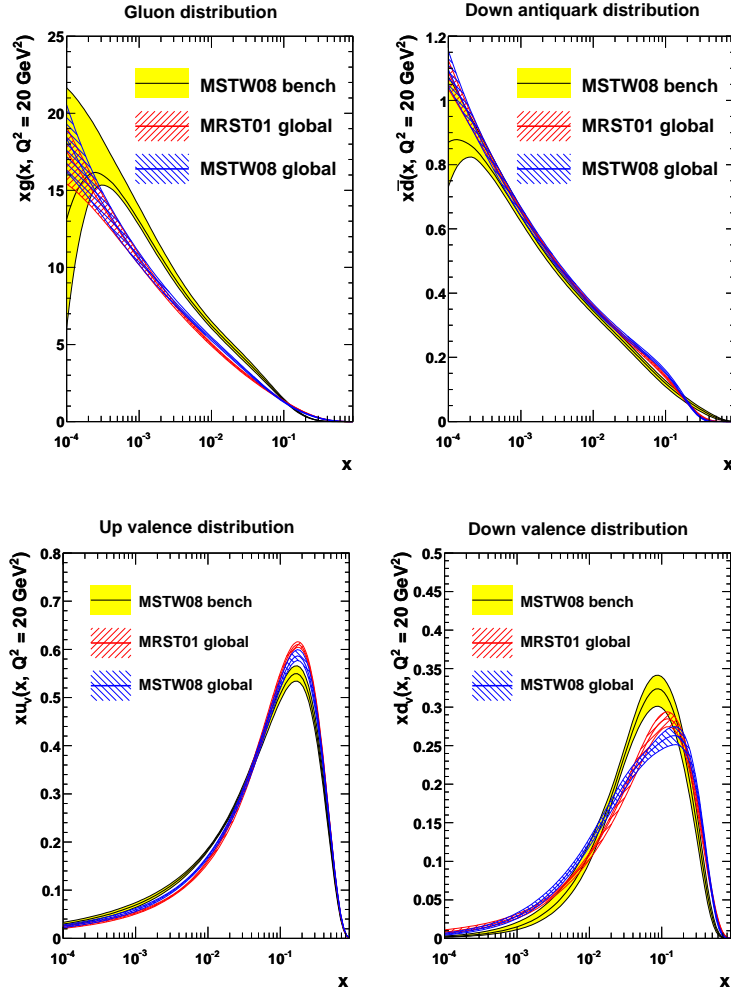


Fig. 27: Comparison of the MSTW benchmark and MRST/MSTW global fits for the gluon, d -sea, u -valence and d -valence at $Q^2 = 20 \text{ GeV}^2$. All uncertainties shown correspond to one- σ bands.

Let us now compare each pair of benchmark and global fits. For NNPDF, the difference in central value between benchmark and reference is comparable to that found between the MRST or Alekhin global fits and their benchmark counterparts in Ref. [1]. However, the NNPDF global and benchmark fits remain compatible within their respective error bands. Indeed, the NNPDF benchmark fit has a rather larger error band than the reference, as one would expect from a fit based on a rather smaller set of (compatible) data. Such a behaviour was however not observed in the comparison between global and benchmark MRST and Alekhin fits of Ref. [1].

It is interesting to observe that the gluon shape at low x of the benchmark and global NNPDF disagree at the one σ level (though they agree at two σ). This can be understood as a consequence of the fact that the value of α_s in the two fits is sizably different ($\alpha_s = 0.112$ vs. $\alpha_s = 0.119$). Theoretical uncertainties related to the value of α_s were shown in Ref. [155] to be negligible and thus not included in the NNPDF error band, but of course they become relevant if α_s is varied by several standard deviations (3.5σ , in this case).

Coming now to MSTW, we first notice that, as discussed in Sect. 3.3.3, the MSTW benchmark set has somewhat larger uncertainty bands than the MRST benchmark set and thus also than each of the sets obtained from global fits. Consequently, the MSTW benchmark PDFs are generally far more consistent with the MSTW global fit sets than the corresponding comparison between MRST benchmark PDFs and global fit PDFs shown in Ref. [1], largely due to the more realistic uncertainties in the MSTW benchmark. Comparing central values we see exactly the same feature in the gluon distribution as the NNPDF group, and the explanation is likewise the same, highlighting possible difficulties in comparing PDFs obtained with different values of $\alpha_s(M_Z)$.

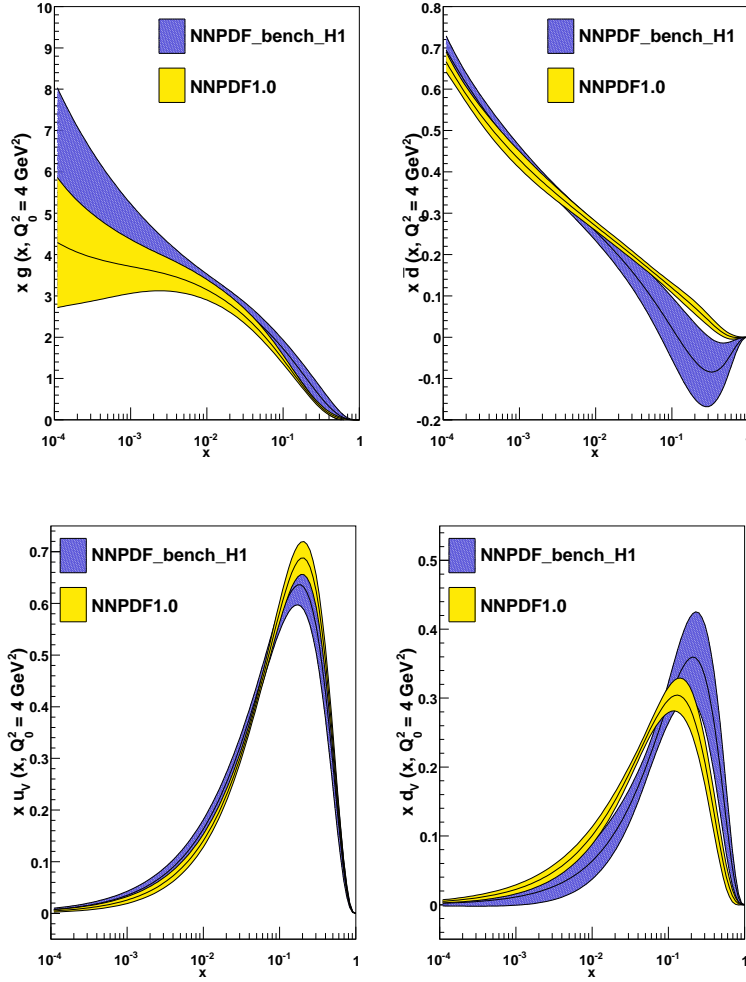


Fig. 28: Comparison of the NNPDF benchmark and reference fits for the gluon, d -sea, u_v and d_v at $Q^2 = 4 \text{ GeV}^2$.

Unlike for the NNPDF group, the MSTW group sees some degree of incompatibility between the benchmark PDFs and the global fit PDFs for the valence quarks, particularly in the case of the down valence. This may be related to the assumption $\bar{u} = \bar{d}$, which constrains valence quarks and sea quarks in an artificial manner since there is less flexibility to alter each independently. Indeed, in the global fits there is an excess of \bar{d} over \bar{u} which maximizes at $x = 0.1$. Forcing equivalence of antiquark distributions might therefore lead to a deficit of down sea quarks and a corresponding excess of up sea quarks, and also, for the same reason, to an excess of down valence quarks. These are indeed seen both in the NNPDF and MSTW benchmark fits when compared to the respective global fits. The effect is however well within the uncertainty bands for NNPDF, which indeed do not observe any statistically significant difference between results of a fit to the reduced benchmark data set with the $\bar{u} = \bar{d}$ assumption (as presented in Fig. 26) or without it (as presented in Ref. [155], Fig. 12).

As well as this important effect one sees that the main discrepancy at $x = 0.1$ for down valence quarks is greater when comparing the benchmark fits to the global MSTW fit than to the global MRST fit. This is because recent new Tevatron data on Z rapidity distributions and lepton asymmetry from W decays provide a strong constraint on the down quark, and some of this new data shows considerable tension with other data sets.

3.4 H1 Benchmark

We now discuss the extension of the fit using the settings of Sect. 3.1.1 to also include the NNPDF approach. Results are compared both to those of the NNPDF reference fit, and to those obtained by the H1 fit of Sect. 3.2 to the same data. We then compare the NNPDF benchmark and reference, with the specific aim of addressing

the issue of the dependence of the results on the size of the data set (H1 dataset vs. the HERA–LHC dataset of Sect. 3.3). Finally, the H1 and NNPDF benchmark fits are compared to each other with the purpose of understanding the impact of the respective methodologies.

3.4.1 NNPDF analysis³⁹

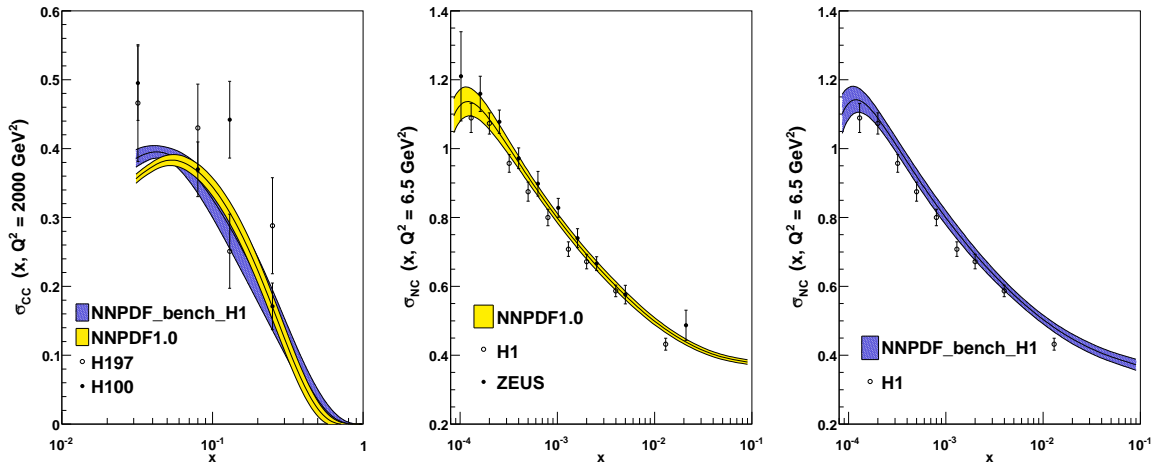


Fig. 29: Left: NNPDF benchmark and reference fits at $\sqrt{s} = 301\text{GeV}$ compared to H1 charged current data. Center: NNPDF reference fit compared to H1 and ZEUS neutral current data. Right: NNPDF benchmark fit compared to H1 neutral current data.

The results of the NNPDF benchmark are compared to the NNPDF reference fit results in Fig. 28. The general features of the benchmark are analogous to those of the HERA–LHC benchmark discussed in Section 3.3.4, with some effects being more pronounced because the benchmark dataset is now even smaller. Specifically, we observe that uncertainties bands blow up when data are removed: this is very clear for instance in the \bar{d} distribution at large- x , as a consequence of the fact that the benchmark dataset of Table 1 does not include deuterium data. The negative value of this PDF at large x is presumably unphysical and it would disappear if positivity of charged current cross sections were imposed, including also the (anti-)neutrino ones. The only positivity constraint in the NNPDF fit is imposed on the F_L structure function [155], because this is the only DIS observable whose positivity is not constrained by the full data set.

It is interesting to note however that this effect is not observed for the u_v distribution, where instead the benchmark and the reference fit show almost equal uncertainties. In order to understand this, in Fig. 29 we compare two situations with or without error shrinking, by examining the predictions obtained using the benchmark and reference fits for some observables to the corresponding data. A first plot (left) shows the shrinking of the uncertainty on the prediction for the charged–current cross section in the reference fit. This is mostly due to the CHORUS neutrino data, which are in the reference and not in the benchmark. These data are clearly consistent with the H1 data shown in the plot. The subsequent pair of plots compares (center) the prediction for the neutral–current cross section from the reference fit compared to H1 and ZEUS data (both of which are used for the reference fit), and (right) from the benchmark fit to the H1 data only (which are the only ones used in the benchmark fit). The uncertainty bands in the two fits are similar size: indeed, the ZEUS and H1 data display a systematic disagreement which is approximately the size of this uncertainty band. Hence, the (small but significant) systematic inconsistency between the ZEUS and H1 data prevents reduction of the uncertainty band when the ZEUS data are added to the fit, beyond the size of this discrepancy. Therefore, the NNPDF methodology leads to combined uncertainties for inconsistent data which are similar to those obtained with the so–called PDG (or scale-factor) method [167].

Notice that if relative normalization are fitted (as done by in the H1 approach of Sect. 3.2) instead of being treated simply as a source of systematics, this systematic inconsistency would be significantly reduced

³⁹Contributing authors R. D. Ball, L. Del Debbio, S. Forte, A. Guffanti, J. I. Latorre, A. Piccione, J. Rojo, M. Ubiali

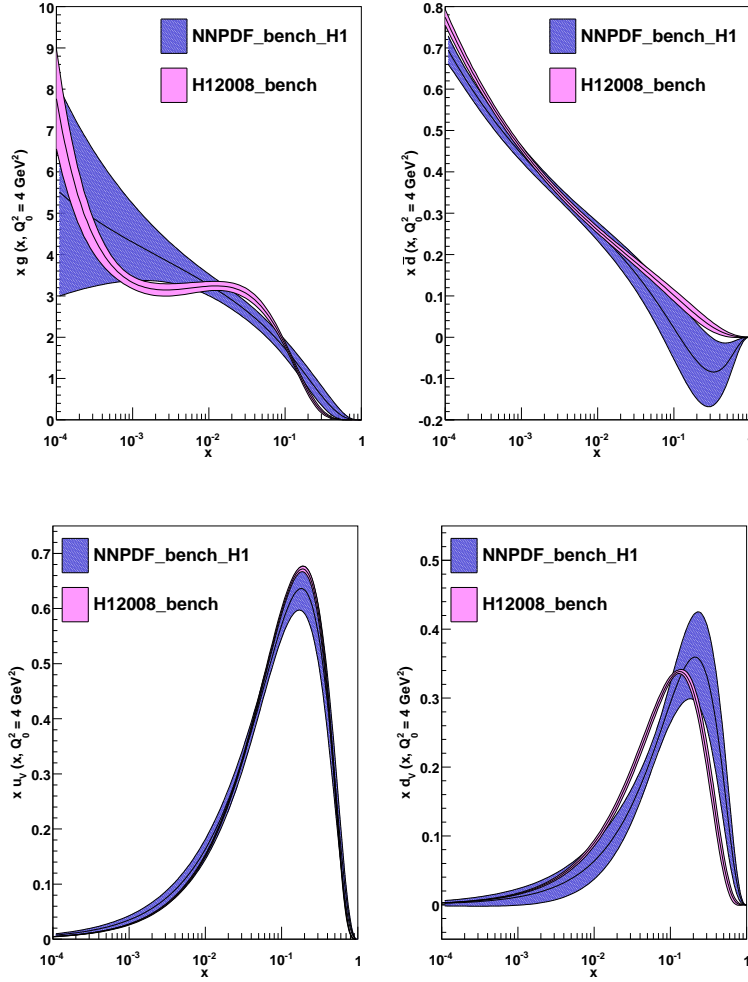


Fig. 30: Comparison of the NNPDF and H1 benchmark fit for the gluon, d -sea, u_v and d_v at $Q^2 = 4 \text{ GeV}^2$.

Data Set	$\chi_{\text{H1}}^2/N_{\text{data}}$	$\chi_{\text{NNPDF}}^2/N_{\text{data}}$
H197mb	0.83	0.82
H197lowQ2	0.90	0.87
H197NC	0.69	0.80
H197CC	0.73	0.97
H199NC	0.88	1.01
H199CC	0.62	0.84
H199NChy	0.35	0.35
H100NC	0.97	1.00
H100CC	1.07	1.38
Total	0.88	0.96

Table 6: H1 and NNPDF χ^2 for the total and each single data set. Cross correlations among data sets are neglected to evaluate the χ^2 of a single data set.

in the best-fit. The associate uncertainty however then appears as an addition source of systematics. This happens when H1 and ZEUS data are combined in a single dataset (see Section 4.1 below). In the NNPDF approach, instead, this systematics is produced by the Monte Carlo procedure.

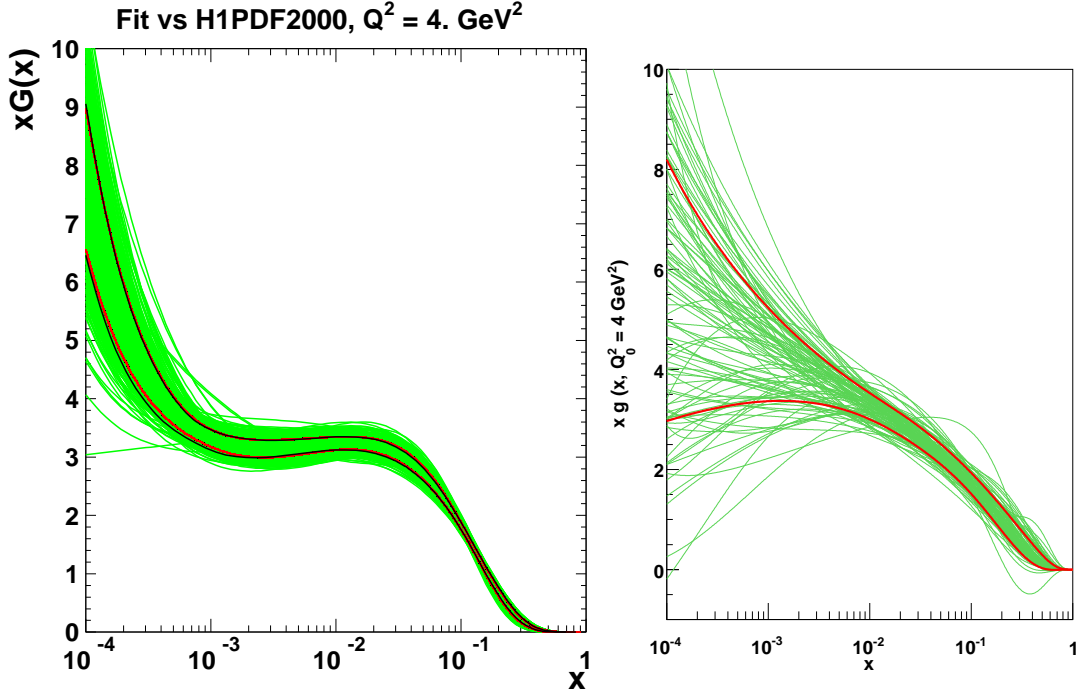


Fig. 31: The Monte Carlo set of gluon PDFs for the H1 benchmark (left, same as Fig. 23) and the NNPDF benchmark. The red lines show the one-sigma contour calculated from the Monte Carlo set, and in the H1 case the black lines show the Hessian one-sigma contour.

3.4.2 Comparison between the Benchmark Parton Distributions

The χ^2 of the H1 and NNPDF benchmarks are given in Table 6, while the corresponding PDFs are compared in Fig. 30. Furthermore, in Fig. 31 we show the respective full Monte Carlo PDF sets in the case of the gluon distribution.

The quality of the two fits is comparable, the differences in χ^2 being compatible with statistical fluctuations. In the region where experimental information is mostly concentrated, specifically for the u_v distribution over all the x -range and for the \bar{d} and the d_v distributions in the small- x range, the results of the two fits are in good agreement, though the H1 uncertainty bands are generally somewhat smaller.

In the region where experimental information is scarce or missing, sizable differences are found, similar to those observed when comparing the MRST/MSTW bench and NNPDF bench to the HERA–LHC benchmark of Sect. 3.3.3. Specifically, in these regions NNPDF uncertainties are generally larger than H1 bands: the width of the uncertainty band for the H1 fit varies much less between the data and extrapolation regions than that of the NNPDF bench. Also, the H1 central value always falls within the NNPDF uncertainty band, but the NNPDF central value tends to fall outside the H1 uncertainty band whenever the central values differ significantly. Figure 31 suggests that this may be due to the greater flexibility of the functional form in the NNPDF fit. Specifically, the \bar{d} quark distribution at large x does not become negative in the H1 fit, because this behaviour is not allowed by the parameterization.

4 DETERMINATION OF PARTON DISTRIBUTIONS

4.1 Extraction of the proton PDFs from a combined fit of H1 and ZEUS inclusive DIS cross sections ⁴⁰

4.1.1 Introduction

The kinematics of lepton hadron scattering is described in terms of the variables Q^2 , the invariant mass of the exchanged vector boson, Bjorken x , the fraction of the momentum of the incoming nucleon taken by the struck quark (in the quark-parton model), and y which measures the energy transfer between the lepton and hadron systems. The differential cross-section for the neutral current (NC) process is given in terms of the structure functions by

$$\frac{d^2\sigma(e^\pm p)}{dx dQ^2} = \frac{2\pi\alpha^2}{Q^4 x} [Y_+ F_2(x, Q^2) - y^2 F_L(x, Q^2) \mp Y_- x F_3(x, Q^2)],$$

where $Y_\pm = 1 \pm (1 - y)^2$. The structure functions F_2 and $x F_3$ are directly related to quark distributions, and their Q^2 dependence, or scaling violation, is predicted by perturbative QCD. For low x , $x \leq 10^{-2}$, F_2 is sea quark dominated, but its Q^2 evolution is controlled by the gluon contribution, such that HERA data provide crucial information on low- x sea-quark and gluon distributions. At high Q^2 , the structure function $x F_3$ becomes increasingly important, and gives information on valence quark distributions. The charged current (CC) interactions also enable us to separate the flavour of the valence distributions at high- x , since their (LO) cross-sections are given by,

$$\begin{aligned} \frac{d^2\sigma(e^+p)}{dx dQ^2} &= \frac{G_F^2 M_W^4}{(Q^2 + M_W^2)^2 2\pi x} x [(\bar{u} + \bar{c}) + (1 - y)^2 (d + s)], \\ \frac{d^2\sigma(e^-p)}{dx dQ^2} &= \frac{G_F^2 M_W^4}{(Q^2 + M_W^2)^2 2\pi x} x [(u + c) + (1 - y)^2 (\bar{d} + \bar{s})]. \end{aligned}$$

Parton Density Function (PDF) determinations are usually obtained in global NLO QCD fits [168–170], which use fixed target DIS data as well as HERA data. In such analyses, the high statistics HERA NC e^+p data have determined the low- x sea and gluon distributions, whereas the fixed target data have determined the valence distributions. Now that high- Q^2 HERA data on NC and CC e^+p and e^-p inclusive double differential cross-sections are available, PDF fits can be made to HERA data alone, since the HERA high Q^2 cross-section data can be used to determine the valence distributions. This has the advantage that it eliminates the need for heavy target corrections, which must be applied to the ν -Fe and μ D fixed target data. Furthermore there is no need to assume isospin symmetry, i.e. that d in the proton is the same as u in the neutron, since the d distribution can be obtained directly from CC e^+p data.

The H1 and ZEUS collaborations have both used their data to make PDF fits [170], [18]. Both of these data sets have very small statistical uncertainties, so that the contribution of systematic uncertainties becomes dominant and consideration of point to point correlations between systematic uncertainties is essential. The ZEUS analysis takes account of correlated experimental systematic errors by the Offset Method, whereas H1 uses the Hessian method [171]. Whereas the resulting ZEUS and H1 PDFs are compatible, the gluon PDFs have rather different shapes, see Fig 38, and the uncertainty bands spanned by these analyses are comparable to those of the global fits.

It is possible to improve on this situation since ZEUS and H1 are measuring the same physics in the same kinematic region. These data have been combined using a 'theory-free' Hessian fit in which the only assumption is that there is a true value of the cross-section, for each process, at each x, Q^2 point [172]. Thus each experiment has been calibrated to the other. This works well because the sources of systematic uncertainty in each experiment are rather different, such that all the systematic uncertainties are re-evaluated. The resulting correlated systematic uncertainties on each of the combined data points are significantly smaller than the statistical errors. This combined data set has been used as the input to an NLO QCD PDF fit. The consistency of the input data set and its small systematic uncertainties enables us to calculate the experimental uncertainties on the PDFs using the χ^2 tolerance, $\Delta\chi^2 = 1$. This represents a further advantage compared to the global fit analyses where increased tolerances of $\Delta\chi^2 = 50 - 100$ are used to account for data inconsistencies.

⁴⁰Contributing authors: A. Cooper-Sarkar, A. Glazov, G. Li for the H1-ZEUS combination group.

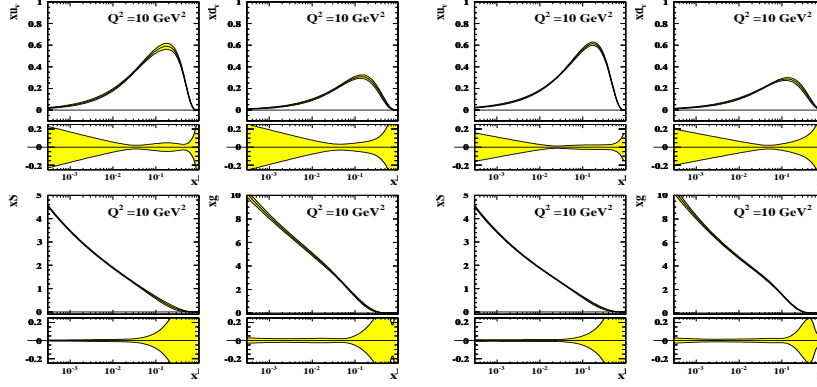


Fig. 32: HERAPDFs, xu_v, xd_v, xS, xg at $Q^2 = 10\text{GeV}^2$. (Left) with experimental uncertainties evaluated as for the central fit (see text) and (right) with experimental uncertainties evaluated by accounting for the 47 systematic errors by the Hessian method.

For the HERAPDF0.1 fit presented here, the role of correlated systematic uncertainties is no longer crucial since these uncertainties are relatively small. This ensures that similar results are obtained using either Offset or Hessian methods, or by simply combining statistical and systematic uncertainties in quadrature. The χ^2 per degree of freedom for a Hessian fit is 553/562 and for a quadrature fit it is 428/562. For our central fit we have chosen to combine the 43 systematic uncertainties which result from the separate ZEUS and H1 data sets in quadrature, and to Offset the 4 sources of uncertainty which result from the combination procedure. The χ^2 per degree of freedom for this fit is 477/562. This procedure results in the most conservative estimates on the resulting PDFs as illustrated in Fig. 32 which compares the PDFs and their experimental uncertainties as evaluated by the procedure of our central fit and as evaluated by treating the 47 systematic uncertainties by the Hessian method.

Despite this conservative procedure, the experimental uncertainties on the resulting PDFs are impressively small and a thorough consideration of further uncertainties due to model assumptions is necessary. In Section 4.1.2 we briefly describe the data combination procedure. In Section 4.1.3 we describe the NLO QCD analysis and model assumptions. In Section 4.1.4 we give results. In Section 4.1.5 we give a summary of the fit results and specifications for release of the HERAPDF0.1 to LHAPDF. In Section 4.1.6 we investigate the predictions of the HERAPDF0.1 for W and Z cross-sections at the LHC.

4.1.2 Data Combination

The data combination is based on assumption that the H1 and ZEUS experiments measure the same cross section at the same kinematic points. The systematic uncertainties of the measurements are separated, following the prescription given by the H1 and ZEUS, into point to point correlated sources α_j and uncorrelated systematic uncertainty, which is added to the statistical uncertainty in quadrature to result in total uncorrelated uncertainty σ_i for each bin i . The correlated systematic sources are considered to be uncorrelated between H1 and ZEUS. All uncertainties are treated as multiplicative i.e. proportional to the central values, which is a good approximation for the measurement of the cross sections.

A correlated probability distribution function for the physical cross sections $M^{i,\text{true}}$ and systematic uncertainties $\alpha_{j,\text{true}}$ for a single experiment corresponds to a χ^2 function:

$$\chi_{\text{exp}}^2(M^{i,\text{true}}, \alpha_{j,\text{true}}) = \sum_i \frac{\left[M^{i,\text{true}} - \left(M^i + \sum_j \frac{\partial M^i}{\partial \alpha_j} \frac{M^{i,\text{true}}}{M^i}(\alpha_{j,\text{true}}) \right) \right]^2}{\left(\sigma_i \frac{M^{i,\text{true}}}{M^i} \right)^2} + \sum_j \frac{(\alpha_{j,\text{true}})^2}{\sigma_{\alpha_j}^2}, \quad (50)$$

where M^i are the central values measured by the experiment, $\partial M^i / \partial \alpha_j$ are the sensitivities to the correlated systematic uncertainties and σ_{α_j} are the uncertainties of the systematic sources. For more than one experiment, total χ_{tot}^2 can be represented as a sum of χ_{exp}^2 . The combination procedure allows to represent χ_{tot}^2 in the

following form:

$$\chi_{\text{tot}}^2(M^{i,\text{true}}, \beta_{j,\text{true}}) = \chi_0^2 + \sum_i \frac{\left[M^{i,\text{true}} - \left(M^{i,\text{ave}} + \sum_j \frac{\partial M^{i,\text{ave}}}{\partial \beta_j} \frac{M^{i,\text{true}}}{M^{i,\text{ave}}}(\beta_{j,\text{true}}) \right) \right]^2}{\left(\sigma_{i,\text{ave}} \frac{M^{i,\text{true}}}{M^{i,\text{ave}}} \right)^2} + \sum_j \frac{(\beta_{j,\text{true}})^2}{\sigma_{\beta_j}^2}. \quad (51)$$

Here the sum runs over a union set of the cross section bins. The value of the χ_{tot}^2 at the minimum, χ_0^2 , quantifies consistency of the experiments. $M^{i,\text{ave}}$ are the average values of the cross sections and β_j correspond to the new systematic sources which can be obtained from the original sources α_j through the action of an orthogonal matrix. In essence, the average of several data sets allows one to represent the total χ^2 in a form which is similar to that corresponding to a single data set, Eq. 50, but with modified systematic sources.

The combination is applied to NC and CC cross section data taken with e^+ and e^- beams simultaneously to take into account correlation of the systematic uncertainties. The data taken with proton beam energies of $E_p = 820$ GeV and $E_p = 920$ GeV are combined together for inelasticity $y < 0.35$, for this a small center of mass energy correction is applied. For the combined data set there are 596 data points and 43 experimental systematic sources. The $\chi_0^2/dof = 510/599$ is below 1, which indicates conservative estimation of the uncorrelated systematics.

Besides the experimental uncertainties, four additional sources related to the assumptions made for the systematic uncertainties are considered. Two of the extra sources deal with correlation of the H1 and ZEUS data for estimation of the photoproduction background and simulation of hadronic energy scale. These sources introduce additional $\sim 1\%$ uncertainty for $y > 0.6$ and $y < 0.02$ data. The third source covers uncertainty arising from the center of mass correction by varying $F_L = F_L^{QCD}$ to $F_L = 0$. The resulting uncertainty reaches few per mille level for $y \sim 0.35$. Finally, some of the systematic uncertainties, for example background subtraction, may not be necessary multiplicative but rather additive, independent of the cross section central values. The effect of additive assumption for the errors is evaluated by comparing the average obtained using Eq. 50 and an average in which $M^{i,\text{true}}/M^{i,\text{ave}}$ scaling is removed for all but global normalization errors.

4.1.3 QCD Analysis

The QCD predictions for the structure functions are obtained by solving the DGLAP evolution equations [102, 104, 105] at NLO in the $\overline{\text{MS}}$ scheme with the renormalisation and factorization scales chosen to be Q^2 ⁴¹. The DGLAP equations yield the PDFs at all values of Q^2 provided they are input as functions of x at some input scale Q_0^2 . This scale has been chosen to be $Q_0^2 = 4\text{GeV}^2$ and variation of this choice is considered as one of the model uncertainties. The resulting PDFs are then convoluted with NLO coefficient functions to give the structure functions which enter into the expressions for the cross-sections. The choice of the heavy quark masses is, $m_c = 1.4$, $m_b = 4.75\text{GeV}$, and variation of these choices is included in the model uncertainties. For this preliminary analysis, the heavy quark coefficient functions have been calculated in the zero-mass variable flavour number scheme. The strong coupling constant was fixed to $\alpha_s(M_Z^2) = 0.1176$ [167], and variations in this value of ± 0.002 have also been considered.

The fit is made at leading twist. The HERA data have a minimum invariant mass of the hadronic system, W^2 , of $W_{\text{min}}^2 = 300 \text{ GeV}^2$ and a maximum x , $x_{\text{max}} = 0.65$, such that they are in a kinematic region where there is no sensitivity to target mass and large- x higher twist contributions. However a minimum Q^2 cut is imposed to remain in the kinematic region where perturbative QCD should be applicable. This has been chosen to be $Q_{\text{min}}^2 = 3.5 \text{ GeV}^2$. Variation of this cut is included as one of the model uncertainties.

A further model uncertainty is the choice of the initial parameterization at Q_0^2 . Three types of parameterization have been considered. For each of these choices the PDFs are parameterized by the generic form

$$xf(x) = Ax^B(1-x)^C(1+Dx+Ex^2+Fx^3), \quad (52)$$

⁴¹The programme QCDNUM [163] has been used and checked against the programme QCDfit [173].

and the number of parameters is chosen by 'saturation of the χ^2 ', such that parameters D, E, F are only varied if this brings significant improvement to the χ^2 . Otherwise they are set to zero.

The first parameterization considered follows that used by the ZEUS collaboration. The PDFs for u valence, $xu_v(x)$, d valence, $xd_v(x)$, total sea, $xS(x)$, the gluon, $xg(x)$, and the difference between the d and u contributions to the sea, $x\Delta(x) = x(\bar{d} - \bar{u})$, are parameterized.

$$\begin{aligned} xu_v(x) &= A_{uv}x^{B_{uv}}(1-x)^{C_{uv}}(1 + D_{uv}x + E_{uv}x^2) \\ xd_v(x) &= A_{dv}x^{B_{dv}}(1-x)^{C_{dv}} \\ xS(x) &= A_Sx^{B_S}(1-x)^{C_S} \\ xg(x) &= A_gx^{B_g}(1-x)^{C_g}(1 + D_gx) \\ x\Delta(x) &= A_\Delta x^{B_\Delta}(1-x)^{C_\Delta} \end{aligned}$$

The total sea is given by, $xS = 2x(\bar{u} + \bar{d} + \bar{s} + \bar{c} + \bar{b})$, where $\bar{q} = q_{sea}$ for each flavour, $u = u_v + u_{sea}$, $d = d_v + d_{sea}$ and $q = q_{sea}$ for all other flavours. There is no information on the shape of the $x\Delta$ distribution in a fit to HERA data alone and so this distribution has its parameters fixed, such that its shape is consistent with Drell-Yan data and its normalization is consistent with the size of the Gottfried sum-rule violation. A suppression of the strange sea with respect to the non-strange sea of a factor of 2 at Q_0^2 , is imposed consistent with neutrino induced dimuon data from NuTeV. The normalisation parameters, A_{uv}, A_{dv}, A_g , are constrained to impose the number sum-rules and momentum sum-rule. The B parameters, B_{uv} and B_{dv} are set equal, since there is no information to constrain any difference. Finally this ZEUS-style parameterization has eleven free parameters.

The second parameterization considered follows that of the H1 Collaboration. The choice of quark PDFs which are parameterized is different. The quarks are considered as u -type and d -type, $xU = x(u_v + u_{sea} + c)$, $xD = x(d_v + d_{sea} + s)$, $x\bar{U} = x(\bar{u} + \bar{c})$ and $x\bar{D} = x(\bar{d} + \bar{s})$, assuming $q_{sea} = \bar{q}$, as usual. These four (anti-)quark distributions are parameterized separately.

$$\begin{aligned} xU(x) &= A_Ux^{B_U}(1-x)^{C_U}(1 + D_Ux + E_Ux^2 + F_Ux^3) \\ xD(x) &= A_Dx^{B_D}(1-x)^{C_D}(1 + D_Dx) \\ x\bar{U}(x) &= A_{\bar{U}}x^{B_{\bar{U}}}(1-x)^{C_{\bar{U}}} \\ x\bar{D}(x) &= A_{\bar{D}}x^{B_{\bar{D}}}(1-x)^{C_{\bar{D}}} \\ xg(x) &= A_gx^{B_g}(1-x)^{C_g} \end{aligned}$$

Since the valence distributions must vanish as $x \rightarrow 0$, the parameters, A and B are set equal for xU and $x\bar{U}$; $A_U = A_{\bar{U}}$, $B_U = B_{\bar{U}}$; and for xD and $x\bar{D}$; $A_D = A_{\bar{D}}$, $B_D = B_{\bar{D}}$. Since there is no information on the flavour structure of the sea it is also necessary to set $B_{\bar{U}} = B_{\bar{D}}$, such that there is a single B parameter for all four quark distributions. The normalisation, A_g , of the gluon is determined from the momentum sum-rule and the parameters D_U and D_D are determined by the number sum-rules. Assuming that the strange and charm quark distributions can be expressed as x independent fractions, $f_s = 0.33$ and $f_c = 0.15$, of the d and u type sea respectively, gives the further constraint $A_{\bar{U}} = A_{\bar{D}}(1 - f_s)/(1 - f_c)$, which ensures that $\bar{u} = \bar{d}$ at low x . Finally this H1-style parameterization has 10 free parameters.

The third parameterization we have considered combines the best features of the previous two. It has less model dependence than the ZEUS-style parameterization in that it makes fewer assumptions on the form of sea quark asymmetry $x\Delta$, and it has less model dependence than the H1-style parameterization in that it does not assume equality of all B parameters. Furthermore, although all types of parameterization give acceptable χ^2 values, the third parameterization has the best χ^2 and it gives the most conservative experimental errors. This is the parameterization which we chose for our central fit. The PDFs which are parameterized are xu_v, xd_v, xg and $x\bar{U}, x\bar{D}$.

$$xu_v(x) = A_{uv}x^{B_{uv}}(1-x)^{C_{uv}}(1 + D_{uv}x + E_{uv}x^2)$$

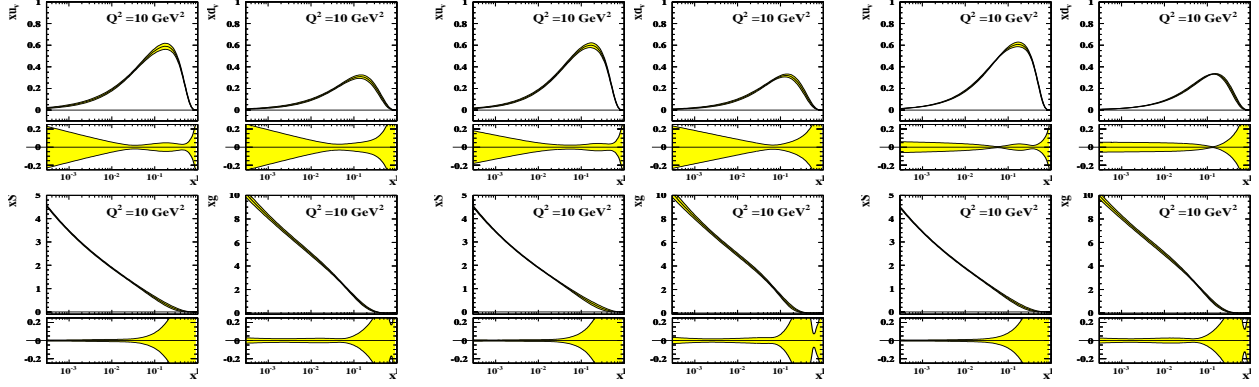


Fig. 33: HERAPDFs, xu_v , xd_v , xS , xg and their uncertainties at $Q^2 = 10\text{GeV}^2$. (Left) for the central fit; (centre) for the ZEUS-style parameterization; (right) for the H1-style parameterization

Model variation	Standard value	Upper Limit	Lower limit
m_c	1.4	1.35	1.5
m_b	4.75	4.3	5.0
Q_{min}^2	3.5	2.5	5.0
Q_0^2	4.0	2.0	6.0
f_s	0.33	0.25	0.40
f_c	0.15	0.12	0.18

Table 7: Standard values of input parameters and cuts, and the variations considered to evaluate model uncertainty

$$\begin{aligned}
 xd_v(x) &= A_{dv} x^{B_{dv}} (1-x)^{C_{dv}} \\
 x\bar{U}(x) &= A_{\bar{U}} x^{B_{\bar{U}}} (1-x)^{C_{\bar{U}}} \\
 x\bar{D}(x) &= A_{\bar{D}} x^{B_{\bar{D}}} (1-x)^{C_{\bar{D}}} \\
 xg(x) &= A_g x^{B_g} (1-x)^{C_g}
 \end{aligned}$$

The normalisation parameters, A_{uv} , A_{dv} , A_g , are constrained to impose the number sum-rules and momentum sum-rule. The B parameters, B_{uv} and B_{dv} are set equal, $B_{uv} = B_{dv}$ and the B parameters $B_{\bar{U}}$ and $B_{\bar{D}}$ are also set equal, $B_{\bar{U}} = B_{\bar{D}}$, such that there is a single B parameter for the valence and another different single B parameter for the sea distributions. Assuming that the strange and charm quark distributions can be expressed as x independent fractions, $f_s = 0.33$ and $f_c = 0.15$, of the d and u type sea, gives the further constraint $A_{\bar{U}} = A_{\bar{D}}(1 - f_s)/(1 - f_c)$. The value of $f_s = 0.33$ has been chosen to be consistent with determinations of this fraction using neutrino induced di-muon production. This value has been varied to evaluate model uncertainties. The charm fraction has been set to be consistent with dynamic generation of charm from the start point of $Q^2 = m_c^2$, in a zero-mass-variable-flavour-number scheme. A small variation of the value of f_c is included in the model uncertainties. Finally this parameterization has 11 free parameters.

It is well known that the choice of parameterization can affect both PDF shapes and the size of the PDF uncertainties. Fig 33 compares the PDFs and their uncertainties as evaluated using these three different parameterizations. As mentioned earlier, the third parameterization results in the most conservative uncertainties.

We present results for the HERA PDFs based on the third type of parameterization, including six sources of model uncertainty as specified in Table 7. We also compare to results obtained by varying $\alpha_s(M_Z^2)$ and by varying the choice of parameterization to those of the ZEUS and the H1 styles of parameterization.

4.1.4 Results

In Fig. 34 we show the HERAPDF0.1 superimposed on the combined data set for NC data and CC data. In

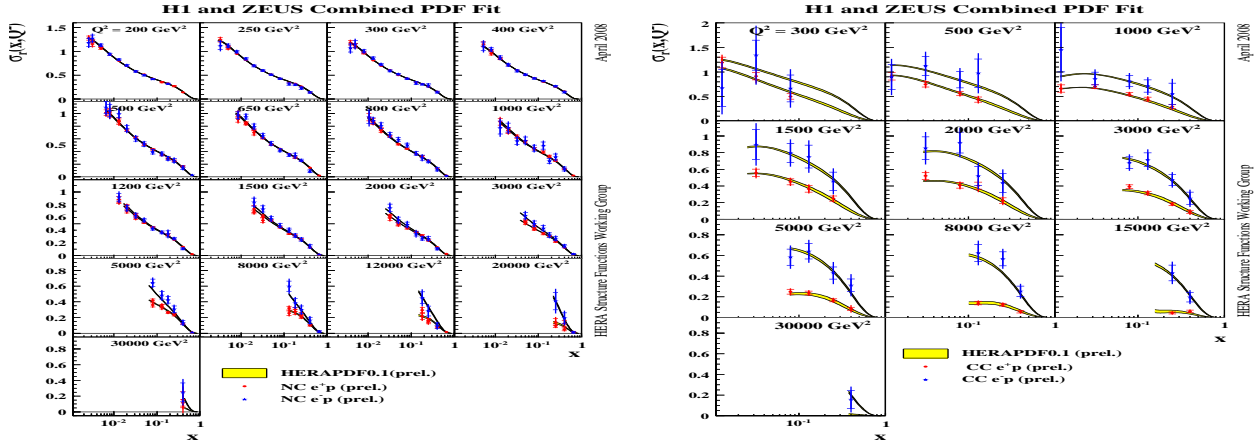


Fig. 34: HERA combined NC (left) and CC (right) data. The predictions of the HERAPDF0.1 fit are superimposed. The uncertainty bands illustrated derive from both experimental and model sources

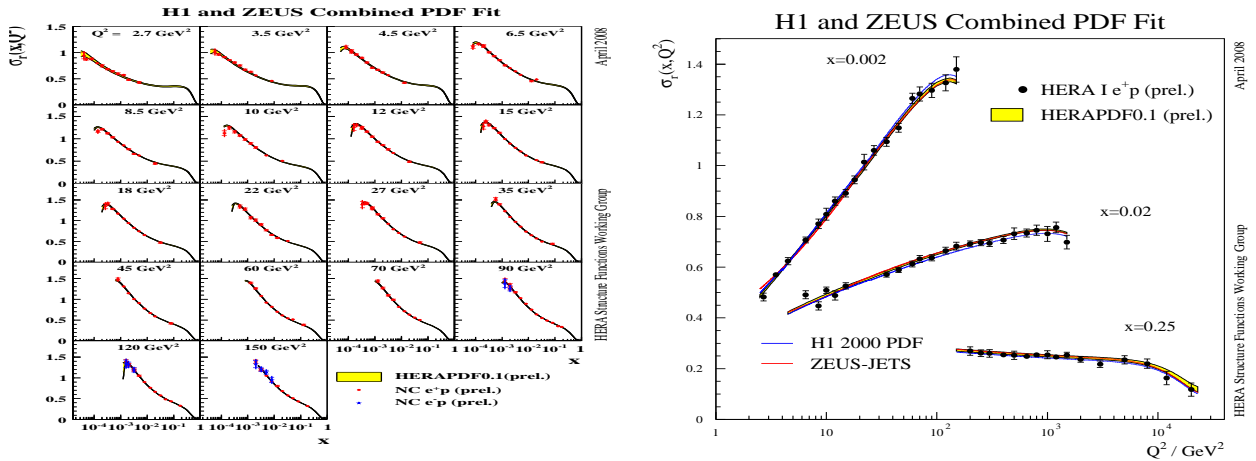


Fig. 35: Left: HERA combined NC data at low Q^2 . Right: the NC reduced cross-section vs Q^2 for three x -bins. The predictions of the HERAPDF0.1 fit are superimposed, together with the predictions of the ZEUS-JETS and H1PDF2000 PDFs

Fig 35 we show the NC data at low Q^2 , and we illustrate scaling violation by showing the reduced cross-section vs. Q^2 for a few representative x bins. The predictions of the HERAPDF0.1 fit are superimposed, together with the predictions of the ZEUS-JETS and H1PDF2000 PDFs.

Fig. 36 shows the HERAPDF0.1 PDFs, xu_v, xd_v, xS, xg , as a function of x at the starting scale $Q^2 = 4 \text{ GeV}^2$ and at $Q^2 = 10 \text{ GeV}^2$. Fig. 37 shows the same PDFs at the scales $Q^2 = 100, 10000 \text{ GeV}^2$. Fractional uncertainty bands are shown beneath each PDF. The experimental and model uncertainties are shown separately. As the PDFs evolve with Q^2 the total uncertainty becomes impressively small.

The total uncertainty of the PDFs obtained from the HERA combined data set is much reduced compared to the PDFs extracted from the analyses of the separate H1 and ZEUS data sets, as can be seen from the summary plot Fig. 38, where these new HERAPDF0.1 PDFs are compared to the ZEUS-JETS and H1PDF2000 PDFs. It is also interesting to compare the present HERAPDF0.1 analysis of the combined HERA-I data set with an analysis of the separate data sets which uses the same parameterization and assumptions. Fig 39 makes this comparison. It is clear that it is the data combination, and not the choice of parameterization and assumptions, which has resulted in reduced uncertainties for the low- x gluon and sea PDFs.

The break-up of the HERAPDFs into different flavours is illustrated in Fig. 40, where the PDFs xU ,

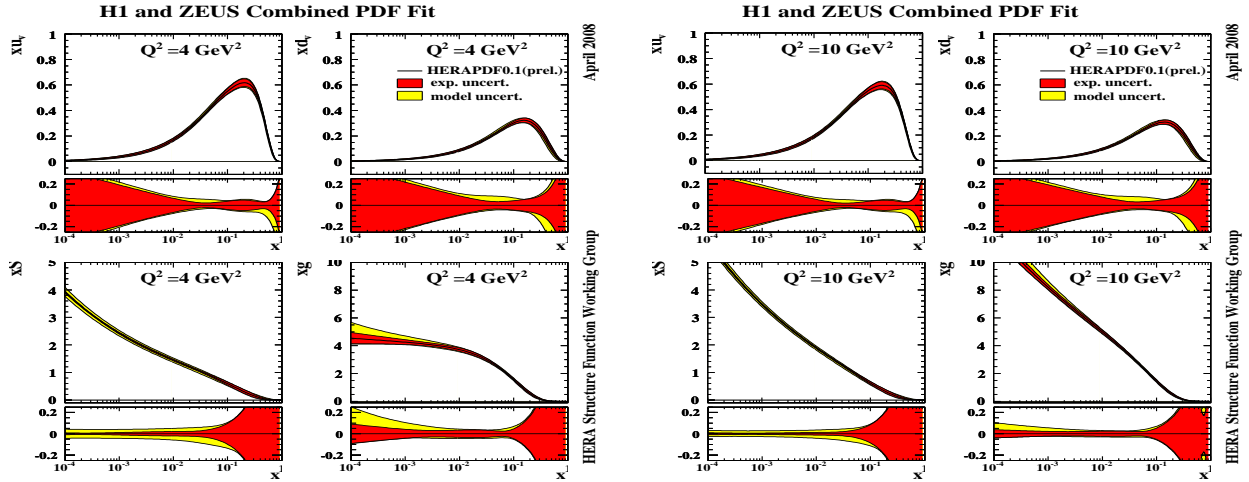


Fig. 36: HERAPDFs, xu_v, xd_v, xS, xg , at (left) $Q^2 = 4 \text{ GeV}^2$ and (right) $Q^2 = 10 \text{ GeV}^2$. Fractional uncertainty bands are shown beneath each PDF. The experimental and model uncertainties are shown separately as the red and yellow bands respectively

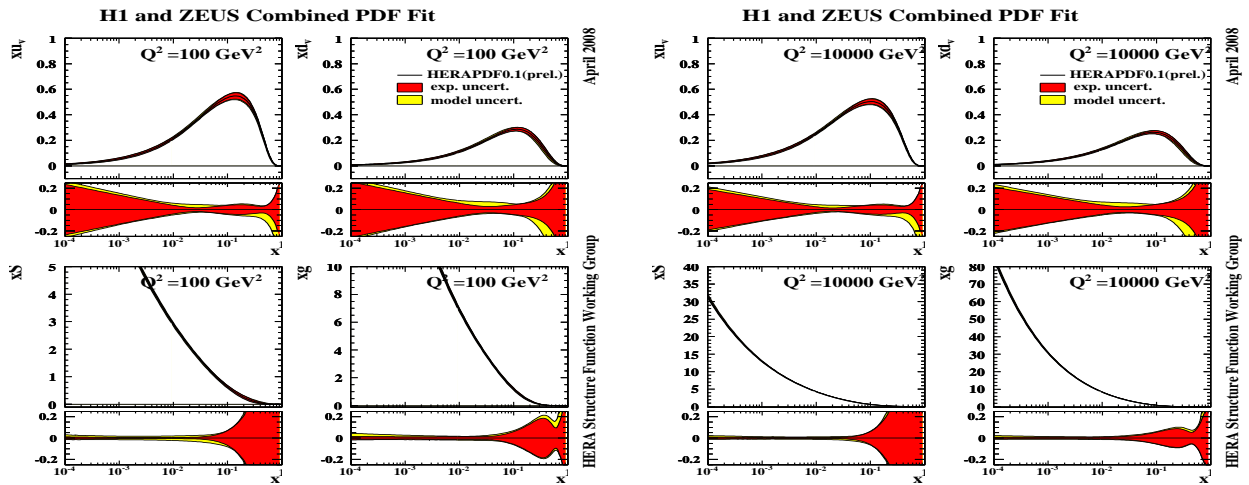


Fig. 37: HERAPDFs, xu_v, xd_v, xS, xg , at (left) $Q^2 = 100 \text{ GeV}^2$ and (right) $Q^2 = 10000 \text{ GeV}^2$. Fractional uncertainty bands are shown beneath each PDF. The experimental and model uncertainties are shown separately as the red and yellow bands respectively

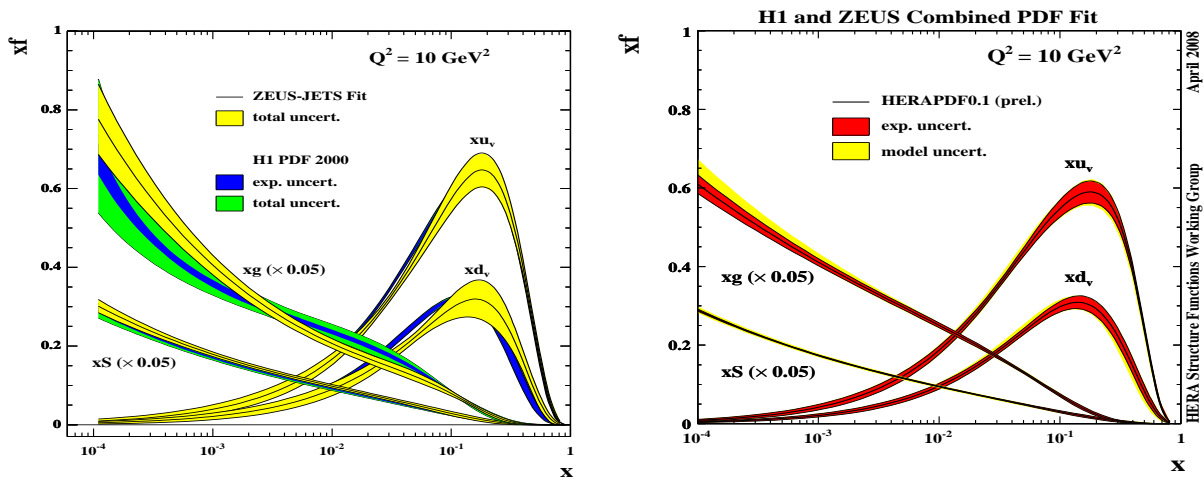


Fig. 38: Left: PDFs from the ZEUS-JETS and H1PDF2000 PDF separate analyses of ZEUS and H1. Right: HERAPDF0.1 PDFs from the analysis of the combined data set

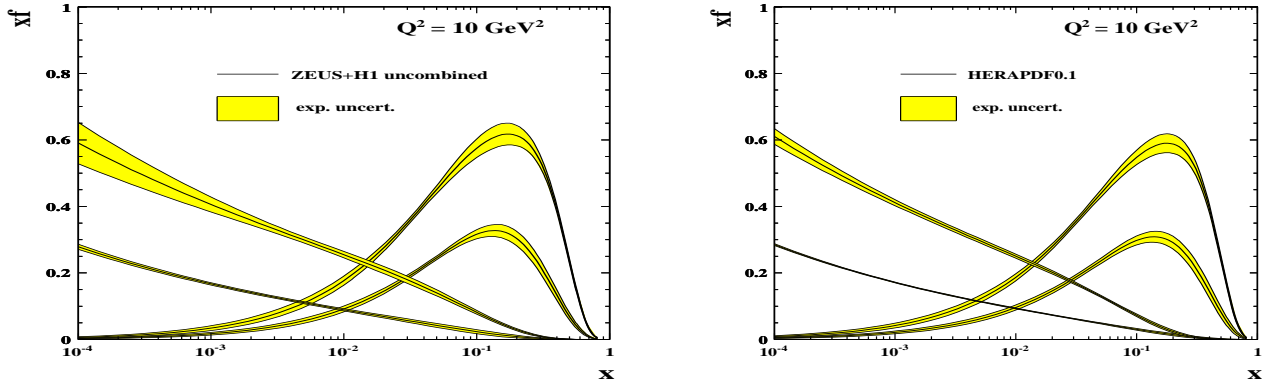


Fig. 39: Left: PDFs resulting from an analysis of the H1 and ZEUS separate data sets using the same parameterization and assumptions as HERAPDF0.1. Right: HERAPDF0.1 PDFs from the analysis of the combined data set (experimental uncertainties only)

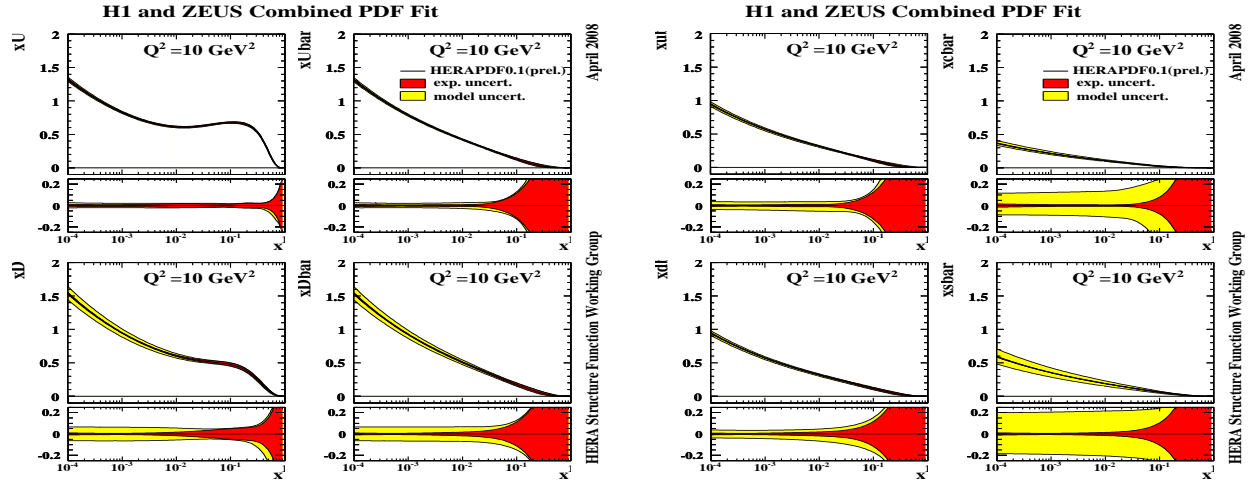


Fig. 40: HERAPDFs at $Q^2 = 10\text{GeV}^2$: (left) $xU, xD, x\bar{U}, x\bar{D}$; (right) $x\bar{u}, x\bar{d}, x\bar{c}, x\bar{s}$. Fractional uncertainty bands are shown beneath each PDF. The experimental and model uncertainties are shown separately as the red and yellow bands respectively

$xD, x\bar{U}, x\bar{D}$ and $x\bar{u}, x\bar{d}, x\bar{c}, x\bar{s}$ are shown at $Q^2 = 10\text{ GeV}^2$. The model uncertainty on these PDFs from variation of Q_{min}^2, Q_0^2, m_c and m_b is modest. The model uncertainty from variation of f_s and f_c is also modest except for its obvious effect on the charm and strange quark distributions.

It is also interesting to look at the results obtained from using the ZEUS-style and H1 style parameterizations described in Section 4.1.3. In Fig. 41 these alternative parameterizations are shown as a blue line superimposed on the HERAPDF0.1 PDFs. These variations in parameterization produce changes in the resulting PDFs which are comparable to the experimental uncertainties in the measured kinematic range. A further variation of parameterization originates from the fact that, if the D parameter for the gluon is allowed to be non-zero, then each type of parameterization yields a double minimum in χ^2 such that the gluon may take a smooth or a 'humpy' shape. Although the lower χ^2 is obtained for the smooth shape, the χ^2 for the 'humpy' shape is still acceptable. The PDFs for the 'humpy' version of our chosen form of parameterization are compared to the standard version in Fig. 42, where they are shown as a blue line superimposed on the HERAPDF0.1 PDFs. This comparison is shown at $Q^2 = 4\text{GeV}^2$, where the difference is the greatest. Nevertheless the resulting PDFs are comparable to those of the standard choice. This explains a long-standing disagreement in the shape of the gluon obtained by the separate ZEUS-JETS and H1PDF200 analyses. The ZEUS data favoured the smooth shape and the H1 data favoured the 'humpy' shape. However the precision of the combined data set results in PDFs for these shapes which are not significantly different in the measured kinematic region.

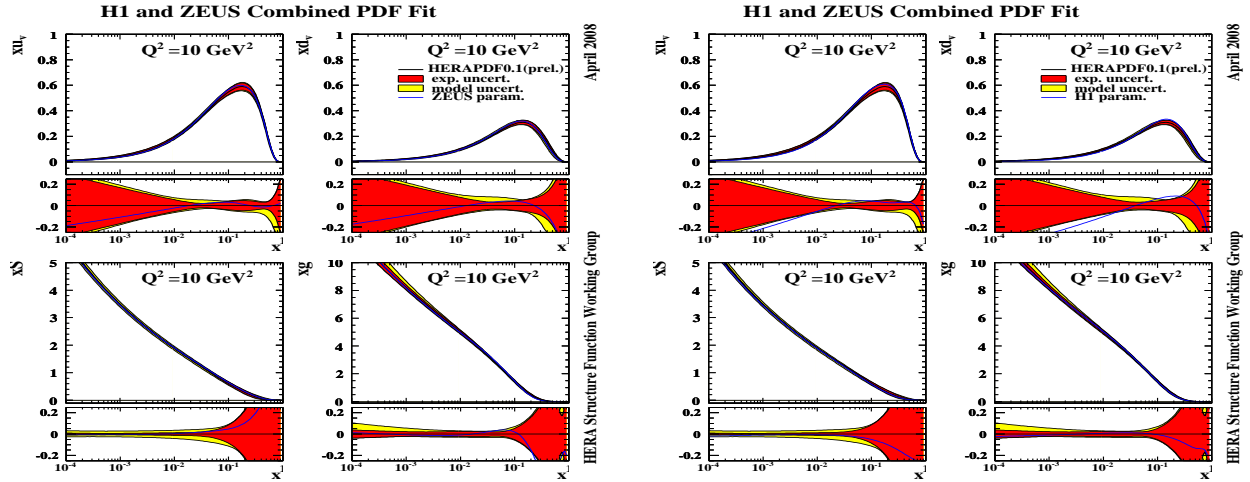


Fig. 41: HERAPDFs at $Q^2 = 10 \text{ GeV}^2$: with the results for the ZEUS-style parameterization (left) and for the H1-style parameterization (right) superimposed as a blue line.

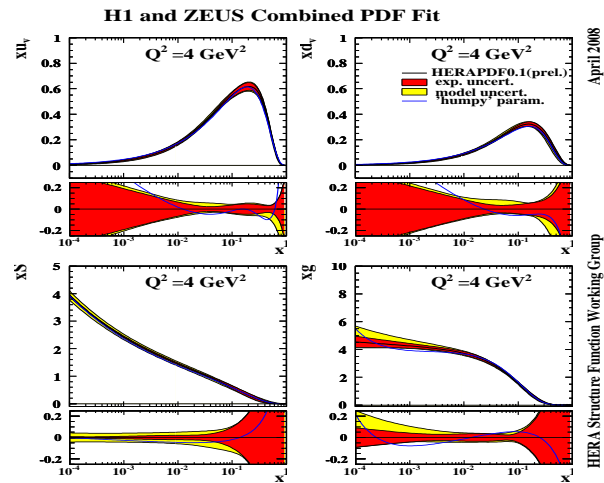


Fig. 42: HERAPDFs at $Q^2 = 4 \text{ GeV}^2$: with the results for the humpy version superimposed as a blue line.

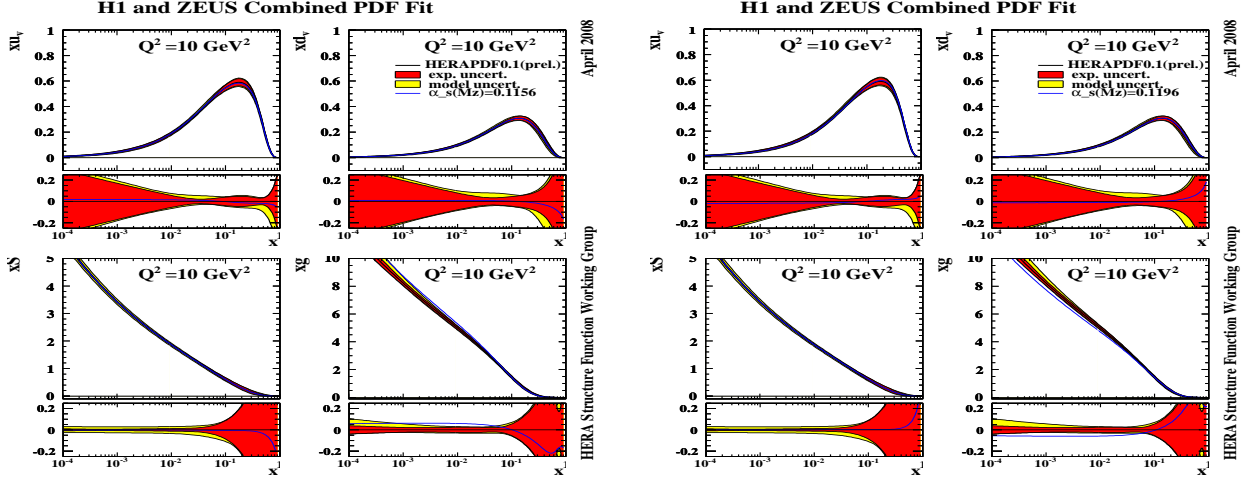


Fig. 43: HERAPDFs at $Q^2 = 10\text{GeV}^2$: with the results for $\alpha_s(M_Z^2) = 0.1156$ (left) and for $\alpha_s(M_Z^2) = 0.1196$ (right) superimposed as a blue line.

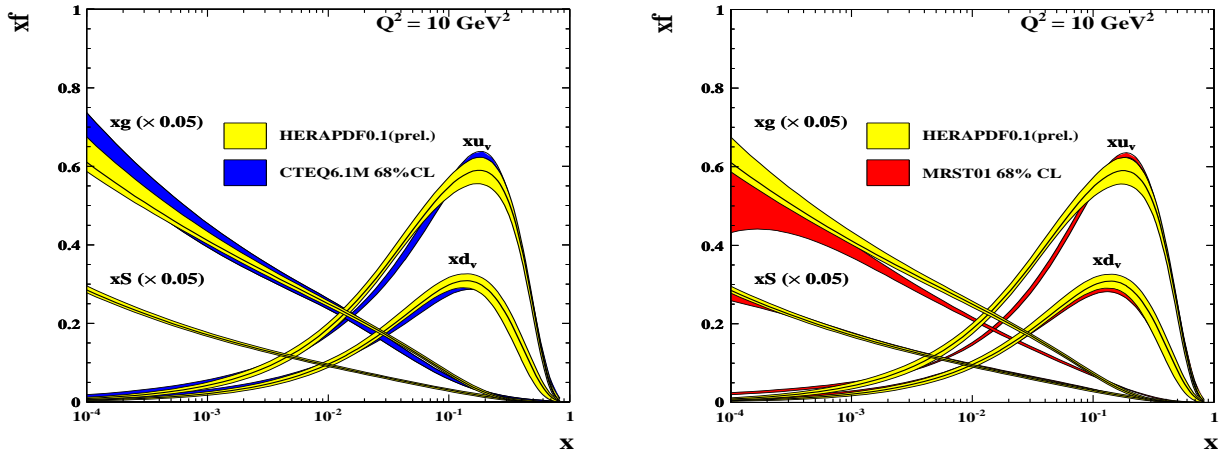


Fig. 44: HERAPDFs at $Q^2 = 10\text{GeV}^2$ compared to the PDFs from CTEQ6.1 and MRST01

It is also interesting to compare the PDFs for the standard choice to those obtained with a different input value of $\alpha_s(M_Z^2)$. The uncertainty on the current PDG value of $\alpha_s(M_Z^2)$ is ± 0.002 and thus we vary our central choice by this amount. The results are shown in Fig. 43, where we can see that this variation only affects the gluon PDF, such that the larger(smaller) value of $\alpha_s(M_Z^2)$ results in a harder(softener) gluon as predicted by the DGLAP equations. The change is outside total uncertainty bands of the standard fit. Finally, Figs. 44 and 45 compare the HERAPDF0.1 PDFs to those of the CTEQ and the MRST/MSTW groups respectively. The uncertainty bands of the CTEQ and MRST/MSTW analyses have been scaled to represent 68% CL limits for direct comparability to the HERAPDF0.1. The HERAPDF0.1 analysis has much improved precision on the low- x gluon.

4.1.5 Summary of HERAPDF0.1 results

Now that high- Q^2 HERA data on NC and CC e^+p and e^-p inclusive double differential cross-sections are available, PDF fits can be made to HERA data alone, since the HERA high Q^2 cross-section data can be used to determine the valence distributions and HERA low Q^2 cross-section data can be used to determine the Sea and gluon distributions. The combined HERA-I data set, of neutral and charged current inclusive cross-sections for e^+p and e^-p scattering, has been used as the sole input for an NLO QCD PDF fit in the DGLAP formalism. The consistent treatment of systematic uncertainties in the joint data set ensures that

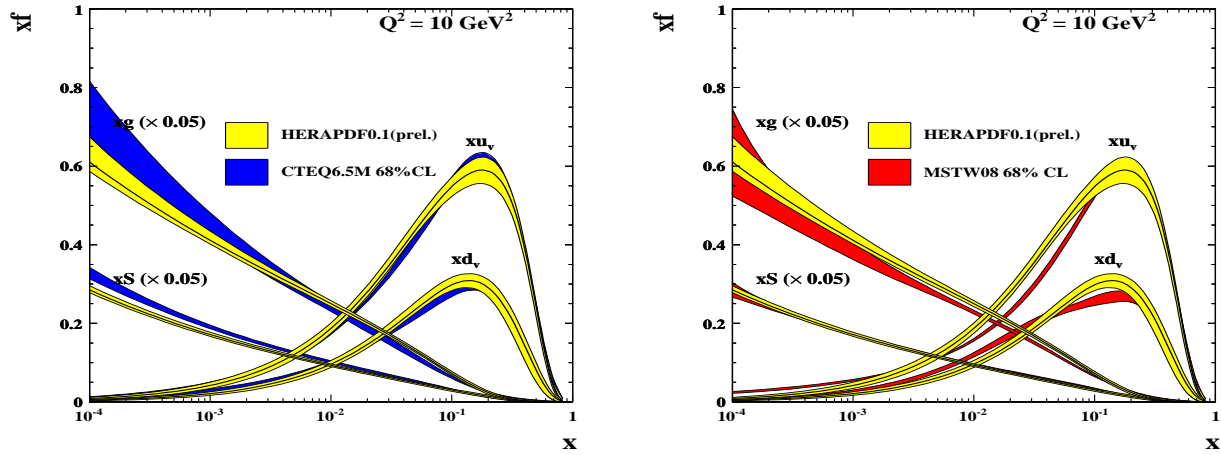


Fig. 45: HERAPDFs at $Q^2 = 10\text{GeV}^2$ compared to the PDFs from CTEQ6.5 and MSTW08(prel.)

experimental uncertainties on the PDFs can be calculated without need for an increased χ^2 tolerance. This results in PDFs with greatly reduced experimental uncertainties compared to the separate analyses of the ZEUS and H1 experiments. Model uncertainties, including those arising from parameterization dependence, have also been carefully considered. The resulting HERAPDFs (called HERAPDF0.1) have improved precision at low- x compared to the global fits. This will be important for predictions of the W and Z cross-sections at the LHC, as explored in the next Section.

These PDFs have been released on LHAPDF in version LHAPDF.5.6: they consist of a central value and 22 experimental eigenvectors plus 12 model alternatives. The user should sum over $N_{\text{mem}}=1,22$ for experimental uncertainties and over $N_{\text{mem}}=1,34$ for total uncertainties.

4.1.6 Predictions for W and Z cross-sections at the LHC using the HERAPDF0.1

At leading order (LO), W and Z production occur by the process, $q\bar{q} \rightarrow W/Z$, and the momentum fractions of the partons participating in this subprocess are given by, $x_{1,2} = \frac{M}{\sqrt{s}} \exp(\pm y)$, where M is the centre of mass energy of the subprocess, $M = M_W$ or M_Z , \sqrt{s} is the centre of mass energy of the reaction ($\sqrt{s} = 14$ TeV at the LHC) and $y = \frac{1}{2} \ln \frac{(E+pl)}{(E-pl)}$ gives the parton rapidity. The kinematic plane for LHC parton kinematics is shown in Fig. 46. Thus, at central rapidity, the participating partons have small momentum fractions, $x \sim 0.005$. Moving away from central rapidity sends one parton to lower x and one to higher x , but over the central rapidity range, $|y| < 2.5$, x values remain in the range, $5 \times 10^{-4} < x < 5 \times 10^{-2}$. Thus, in contrast to the situation at the Tevatron, the scattering is happening mainly between sea quarks. Furthermore, the high scale of the process $Q^2 = M^2 \sim 10,000 \text{ GeV}^2$ ensures that the gluon is the dominant parton, see Fig. 46, so that these sea quarks have mostly been generated by the flavour blind $g \rightarrow q\bar{q}$ splitting process. Thus the precision of our knowledge of W and Z cross-sections at the LHC is crucially dependent on the uncertainty on the momentum distribution of the low- x gluon.

HERA data have already dramatically improved our knowledge of the low- x gluon, as discussed in earlier proceedings of the HERALHC workshop [1]. Now that the precision of HERA data at small- x have been dramatically improved by the combination of H1 and ZEUS HERA-I data, we re-investigate the consequences for predictions of W, Z production at the LHC.

Predictions for the W/Z cross-sections, decaying to the lepton decay mode, using CTEQ, ZEUS PDFs and the HERAPDF0.1 are summarised in Table 8. Note that the uncertainties of CTEQ PDFs have been rescaled to represent 68% CL, in order to be comparable to the HERA PDF uncertainties. The precision on the predictions of the global fits (CTEQ6.1/5 and ZEUS-2002) for the total W/Z cross-sections is $\sim 3\%$ at 68% CL. The precision of the ZEUS-2005 PDF fit prediction, which used only ZEUS data, is comparable, since information on the low- x gluon is coming from HERA data alone. The increased precision of the HERAPDF0.1 low- x gluon PDF results in increased precision of the W/Z cross-section predictions of $\sim 1\%$.

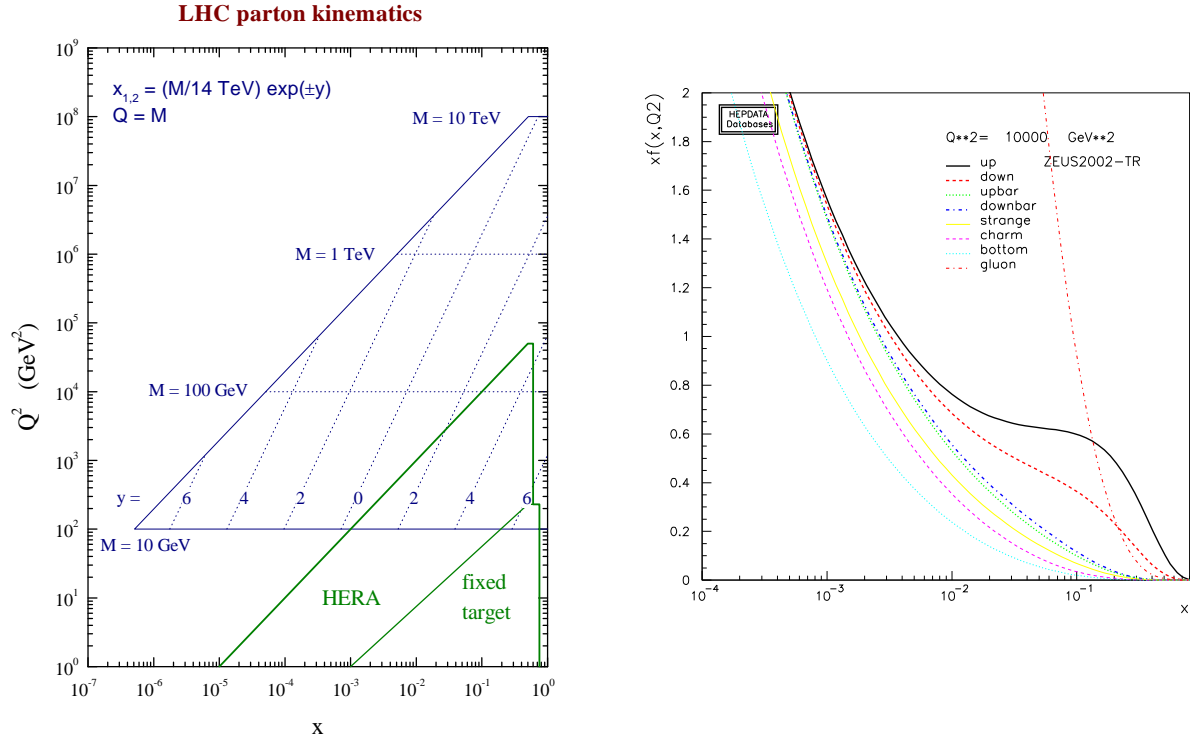


Fig. 46: Left plot: The LHC kinematic plane (thanks to James Stirling). Right plot: Typical PDF distributions at $Q^2 = 10,000 \text{ GeV}^2$.

PDF Set	$\sigma(W^+).B(W^+ \rightarrow l^+\nu_l)$	$\sigma(W^-).B(W^- \rightarrow l^-\bar{\nu}_l)$	$\sigma(Z).B(Z \rightarrow l^+l^-)$
CTEQ6.1	$11.61 \pm 0.34 \text{ nb}$	$8.54 \pm 0.26 \text{ nb}$	$1.89 \pm 0.05 \text{ nb}$
CTEQ6.5	$12.47 \pm 0.28 \text{ nb}$	$9.14 \pm 0.22 \text{ nb}$	$2.03 \pm 0.04 \text{ nb}$
ZEUS-2002	$12.07 \pm 0.41 \text{ nb}$	$8.76 \pm 0.30 \text{ nb}$	$1.89 \pm 0.06 \text{ nb}$
ZEUS-2005	$11.87 \pm 0.45 \text{ nb}$	$8.74 \pm 0.31 \text{ nb}$	$1.97 \pm 0.06 \text{ nb}$
HERAPDF0.1	$12.14 \pm 0.13 \text{ nb}$	$9.08 \pm 0.14 \text{ nb}$	$1.99 \pm 0.025 \text{ nb}$

Table 8: LHC W/Z cross-sections for decay via the lepton mode, for various PDFs, with 68% CL uncertainties.

It is interesting to consider the predictions as a function of rapidity. Fig 47 shows the predictions for W^+ , W^- , Z production as a function of rapidity from the HERAPDF0.1 PDF fit and compares them to the predictions from a PDF fit, using the same parameterization and assumptions, to the H1 and ZEUS data from HERA-I uncombined. The increase precision due to the combination is impressive. Fig. 48 show the predictions for W^+ , W^- , Z production as a function of rapidity from the CTEQ6.1, 6.6 and MRST01 PDF fits for comparison. The uncertainties on the CTEQ and MRST PDF predictions have been rescaled to represent 68% CL limits, for direct comparability to the HERAPDF0.1 uncertainties. At central rapidity these limits give an uncertainty on the boson cross-sections of $\sim 5\%$, ($\sim 3\%$), ($\sim 2\%$) for CTEQ6.1, (CTEQ6.6), (MRST01) compared to $\sim 1\%$ for the HERAPDF0.1.

So far, only experimental uncertainties have been included in these evaluations. It is also necessary to include model uncertainties. Fig. 49 shows the W^+ , W^- , Z rapidity distributions including the six sources of model uncertainty detailed in Section 4.1.3. These model uncertainties increase the total uncertainty at central rapidity to $\sim 2\%$. Further uncertainty due to the choice of $\alpha_s(M_Z)$ is small because, although a lower (higher) choice results in a larger (smaller) gluon at low x , the rate of QCD evolution is lower (higher) and this largely compensates. Uncertainties due to the choice of parameterization also have little impact on the boson rapidity spectra in the central region as illustrated in Fig. 49 by the superimposed blue line, which represents the alternative 'humpy' gluon parameterization (see Sec. 4.1.4).

Since the PDF uncertainty feeding into the W^+ , W^- and Z production is mostly coming from the

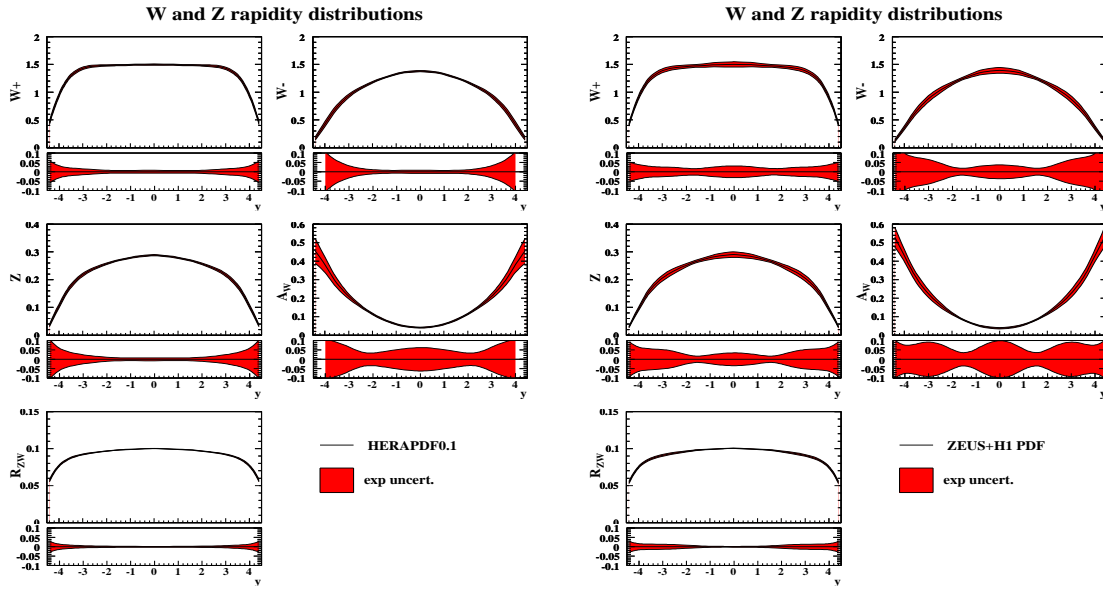


Fig. 47: The W^+ , W^- , Z rapidity distributions, A_W and R_{ZW} (see text) and their uncertainties as predicted by (left) HERAPDF0.1 (right) a similar fit to the uncombined ZEUS and H1 data from HERA-I.

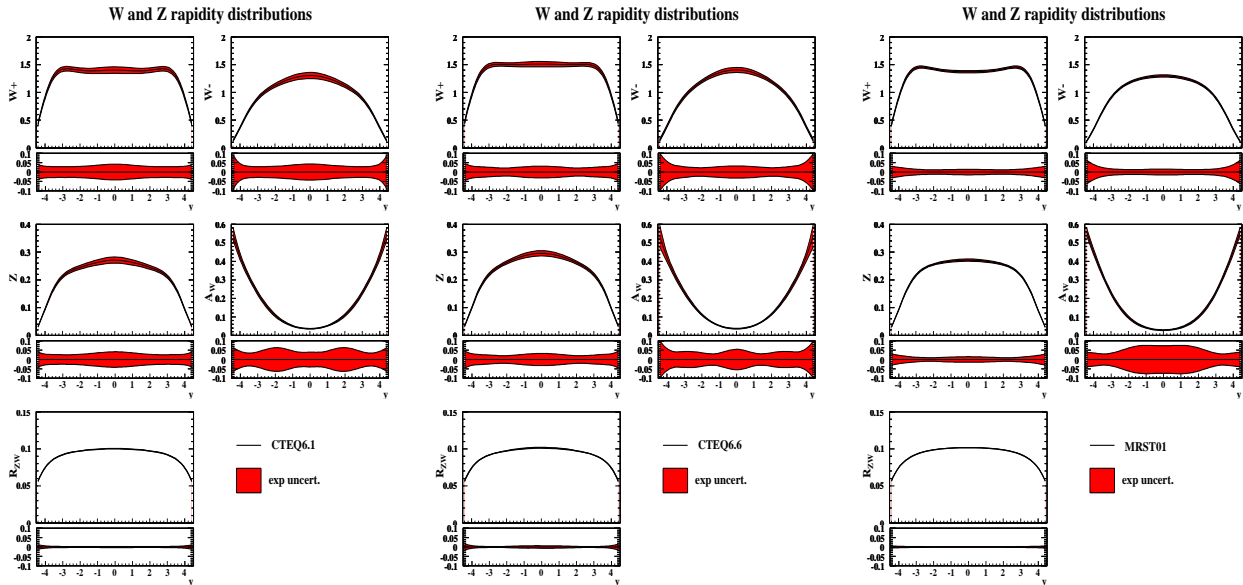


Fig. 48: The W^+ , W^- , Z rapidity distributions, A_W and R_{ZW} (see text) and their uncertainties (scaled to 68% CL) as predicted by (left) CTEQ6.1, (middle) CTEQ6.6, right (MRST01)

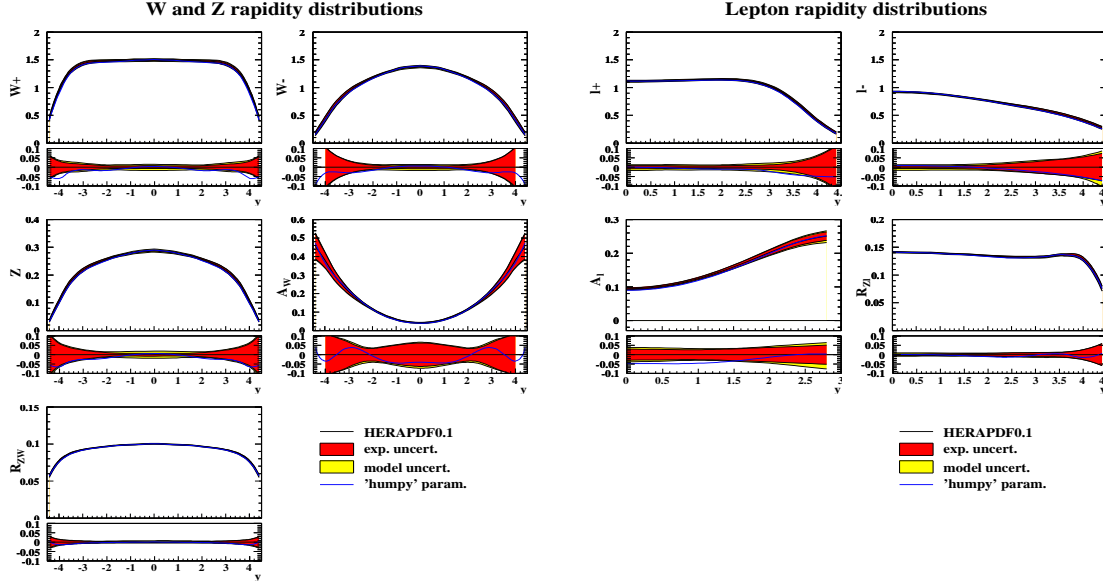


Fig. 49: Left: the W^+ , W^- , Z rapidity distributions, A_W , and R_{ZW} (see text) and their experimental uncertainties (red) and model uncertainties (yellow). Right: the l^+ , l^- rapidity distributions, A_l and R_{Zl} (see text) and their experimental and model uncertainties. The superimposed blue line represents the results of the alternative 'humpy' gluon parameterization.

gluon PDF, for all three processes, there is a strong correlation in their uncertainties, which can be removed by taking ratios. Figs. 47, 48 and 49 also show the W asymmetry

$$A_W = (W^+ - W^-)/(W^+ + W^-).$$

The experimental PDF uncertainty on the asymmetry is larger ($\sim 5\%$ for both CTEQ and HERAPDFs, $\sim 7\%$ for the MRST01 PDFs) than that on the individual distributions and the variation between PDF sets is also larger - compare the central values of the CTEQ and MRST predictions, which are almost 25% discrepant. This is because the asymmetry is sensitive to the difference in the valence PDFs, $u_v - d_v$, in the low- x region, $5 \times 10^{-4} < x < 5 \times 10^{-2}$, where there is no constraint from current data. To see this consider that at LO,

$$A_W \sim (u\bar{d} - d\bar{u})/(u\bar{d} + d\bar{u} + c\bar{s} + s\bar{c})$$

and that $\bar{d} \sim \bar{u}$ at low- x . (Note that the $c\bar{s}$ and $s\bar{c}$ contributions cancel out in the numerator). The discrepancy between the CTEQ and MRST01 asymmetry predictions at $y = 0$ can be quantitatively understood by considering their different valence PDFs (see Figs. 44, 45 in Sec. 4.1.4). In fact a measurement of the asymmetry at the LHC will provide new information to constrain these PDFs.

By contrast, the ratio

$$R_{ZW} = Z/(W^+ + W^-),$$

also shown in Figs. 47, 48 and 49, has very small PDF uncertainties (both experimental and model) and there is no significant variation between PDF sets. To understand this consider that at LO

$$R_{ZW} = (u\bar{u} + d\bar{d} + c\bar{c} + s\bar{s})/(u\bar{d} + d\bar{u} + c\bar{s} + s\bar{c})$$

(modulo electroweak couplings) and that $\bar{d} \sim \bar{u}$ at low- x ⁴². This will be a crucial measurement for our understanding of Standard Model Physics at the LHC.

However, whereas the Z rapidity distribution can be fully reconstructed from its decay leptons, this is not possible for the W rapidity distribution, because the leptonic decay channels which we use to identify the W 's have missing neutrinos. Thus we actually measure the W 's decay lepton rapidity spectra rather than the

⁴²There is some small model dependence from the strange sea fraction accounted for in both HERAPDF0.1 and in CTEQ6.6 PDFs.

W rapidity spectra. Fig. 49 also shows the rapidity spectra for positive and negative leptons from W^+ and W^- decay, the lepton asymmetry,

$$A_l = (l^+ - l^-)/(l^+ + l^-)$$

and the ratio

$$R_{Zl} = Z/(l^+ + l^-)$$

A cut of, $p_{tl} > 25$ GeV, has been applied on the decay lepton, since it will not be possible to trigger on leptons with small p_{tl} . A particular lepton rapidity can be fed from a range of W rapidities so that the contributions of partons at different x values is smeared out in the lepton spectra, but the broad features of the W spectra remain.

In summary, these investigations indicate that PDF uncertainties, deriving from experimental error, on predictions for the W, Z rapidity spectra in the central region, have reached a precision of $\sim 1\%$, due to the input of the combined HERA-I data. This level of precision is maintained when using the leptons from the W decay and gives us hope that we could use these processes as luminosity monitors⁴³. However, model dependent uncertainties must now be considered very carefully. The current study will be repeated using a general-mass variable-flavour scheme for heavy quarks.

The predicted precision on the ratios R_{ZW}, R_{Zl} is even better since model uncertainties are also very small giving a total uncertainty of $\sim 1\%$. This measurement may be used as a SM benchmark. However the W and lepton asymmetries have larger uncertainties (5 – 7%). A measurement of these quantities would give new information on valence distributions at small- x .

4.2 Measurements of the Proton Structure Function F_L at HERA ⁴⁴

4.2.1 Introduction

The inclusive deep inelastic ep scattering (DIS) cross section can at low Q^2 be written in terms of the two structure functions, F_2 and F_L , in reduced form as

$$\sigma_r(x, Q^2, y) \equiv \frac{d^2\sigma}{dx dQ^2} \cdot \frac{Q^4 x}{2\pi\alpha^2 Y_+} = F_2(x, Q^2) - \frac{y^2}{Y_+} \cdot F_L(x, Q^2), \quad (53)$$

where $Q^2 = -q^2$ is the negative of the square of the four-momentum transferred between the electron⁴⁵ and the proton, and $x = Q^2/2qP$ denotes the Bjorken variable, where P is the four-momentum of the proton. The two variables are related through the inelasticity of the scattering process, $y = Q^2/sx$, where $s = 4E_e E_p$ is the centre-of-mass energy squared determined from the electron and proton beam energies, E_e and E_p . In eq. 53, α denotes the fine structure constant and $Y_+ = 1 + (1 - y)^2$.

The two proton structure functions F_2 and F_L are related to the cross sections of the transversely and longitudinally polarised virtual photons interacting with protons, σ_L and σ_T , according to $F_L \propto \sigma_L$ and $F_2 \propto (\sigma_L + \sigma_T)$. Therefore the relation $0 \leq F_L \leq F_2$ holds. In the Quark Parton Model (QPM), F_2 is the sum of the quark and anti-quark x distributions, weighted by the square of the electric quark charges, whereas the value of F_L is zero [174]. The latter follows from the fact that a quark with spin $\frac{1}{2}$ cannot absorb a longitudinally polarised photon.

In Quantum Chromodynamics (QCD), F_L differs from zero, receiving contributions from quarks and from gluons [175]. At low x and in the Q^2 region of deep inelastic scattering the gluon contribution greatly exceeds the quark contribution. Therefore F_L is a direct measure of the gluon distribution to a very good approximation. The gluon distribution is also constrained by the scaling violations of F_2 as described by the DGLAP QCD evolution equations [102–105, 176]. An independent measurement of F_L at HERA, and its comparison with predictions derived from the gluon distribution extracted from the Q^2 evolution of $F_2(x, Q^2)$,

⁴³A caveat is that the current study has been performed using PDF sets which are extracted using NLO QCD in the DGLAP formalism. The extension to NNLO gives small corrections $\sim 1\%$. However, there may be much larger uncertainties in the theoretical calculations because the kinematic region involves low- x . There may be a need to account for $\ln(1/x)$ resummation or high gluon density effects.

⁴⁴Contributing authors: J. Grebenyuk, V. Lendermann

⁴⁵The term electron is used here to denote both electrons and positrons unless the charge state is specified explicitly.

thus represents a crucial test on the validity of perturbative QCD (pQCD) at low x . Moreover, depending on the particular theoretical approach adopted, whether it be a fixed order pQCD calculation, a re-summation scheme, or a color dipole ansatz, there appear to be significant differences in the predicted magnitude of F_L at low Q^2 . A measurement of F_L may be able to distinguish between these approaches.

Previously the structure function F_L was extracted by the H1 collaboration from inclusive data at high y using indirect methods, as discussed in Sect. 4.2.2. A preliminary measurement was also presented by the ZEUS collaboration using initial state radiation (ISR) events [177], although the precision of this measurement was limited.

To make a direct measurement of F_L , reduced cross sections must be measured at the same x and Q^2 but with different y values. This can be seen from eq. 53 which states that $F_L(x, Q^2)$ is equal to the partial derivative $\partial\sigma_r(x, Q^2, y)/\partial(y^2/Y_+)$. Due to the relationship $y = Q^2/xs$ this requires data to be collected at different beam-beam centre-of-mass energies, which was done in the last year of HERA running. To maximize the precision of this procedure, the measurable range of y^2/Y_+ had to be maximised for each fixed x and Q^2 . This was achieved by operating HERA at the lowest attainable centre-of-mass energy and by measuring this data up to the highest possible value of y . An intermediate HERA centre-of-mass energy was also chosen, to improve the precision of F_L extraction and to act as a consistency check. More specifically, between March and June 2007, HERA was operated with proton beam energies, $E_p = 460$ GeV and 575 GeV, compared to the previous nominal value of 920 GeV. The electron beam energy was unaltered at $E_e = 27.6$ GeV. Thus, three data sets, referred to the high- (HER), middle- (MER) and low-energy running (LER) samples, were collected with $\sqrt{s} = 318$ GeV, 251 GeV and 225 GeV, respectively. The integrated luminosities of the data sets used by ZEUS (H1) to measure F_L are $32.8(21.6)$ pb $^{-1}$ for HER, $6(6.2)$ pb $^{-1}$ for MER and $14(12.4)$ pb $^{-1}$ for LER. The specific issues of the recent H1 and ZEUS analyses are discussed in Sect. 4.2.3, and the results are presented in Sect. 4.2.4.

4.2.2 Indirect F_L Extraction by H1

H1 extracted F_L from inclusive data using several indirect methods, which exploit the turn over of the reduced cross section at high y due to the F_L contribution. The basic principle is the following. First, the reduced neutral current cross section σ_r is measured in a y range, where the F_L contribution is negligible and thus the relation $\sigma_r = F_2$ holds very well. Afterward, based on some theoretical assumption, the knowledge of F_2 is extrapolated towards high y . Finally F_L is extracted from the difference between the prediction for F_2 and the measurement of σ_r at high y .

In the analyses at $Q^2 \gtrsim 10$ GeV 2 [18, 89, 178] the ‘‘extrapolation’’ method is used. In this method, an NLO QCD PDF fit to H1 HERA I data is performed at $y < 0.35$, and the results are extrapolated to higher y using the DGLAP evolution equations. F_L is then extracted at a fixed $y = 0.75$ and at Q^2 up to 700 GeV 2 using eq. 53. The extracted values are shown in Fig. 50 for the high- Q^2 analysis [18].

At low Q^2 , extrapolations of DGLAP fits become uncertain. For $Q^2 \lesssim 2$ GeV 2 , as the strong coupling constant $\alpha_s(Q^2)$ increases, the higher order corrections to the perturbative expansion become large and lead to the breakdown of the pQCD calculations. Therefore other methods are used in the H1 low- Q^2 data analyses.

The ‘‘shape method’’, as used in the last H1 low- Q^2 study of HERA I data [179], exploits the shape of σ_r in a given Q^2 bin. The Q^2 dependence at high y is driven by the kinematic factor y^2/Y_+ (eq. 53), and to a lesser extent by $F_L(x, Q^2)$. On the other hand, the gluon dominance at low x suggests that F_L may exhibit an x dependence similar to F_2 . Therefore it is assumed that F_L is proportional to F_2 and the coefficient of proportionality depends only on Q^2 . In the extraction procedure one uses the ratio R of the cross sections of the transversely and longitudinally polarised photons

$$R = \frac{\sigma_T}{\sigma_L} = \frac{F_L}{F_2 - F_L} \quad (54)$$

which is thus assumed to depend only on Q^2 . The reduced cross section is fitted by

$$\sigma_r = F_2 \left[1 - \frac{y^2}{Y_+} \frac{R(Q^2)}{1 + R(Q^2)} \right], \quad (55)$$

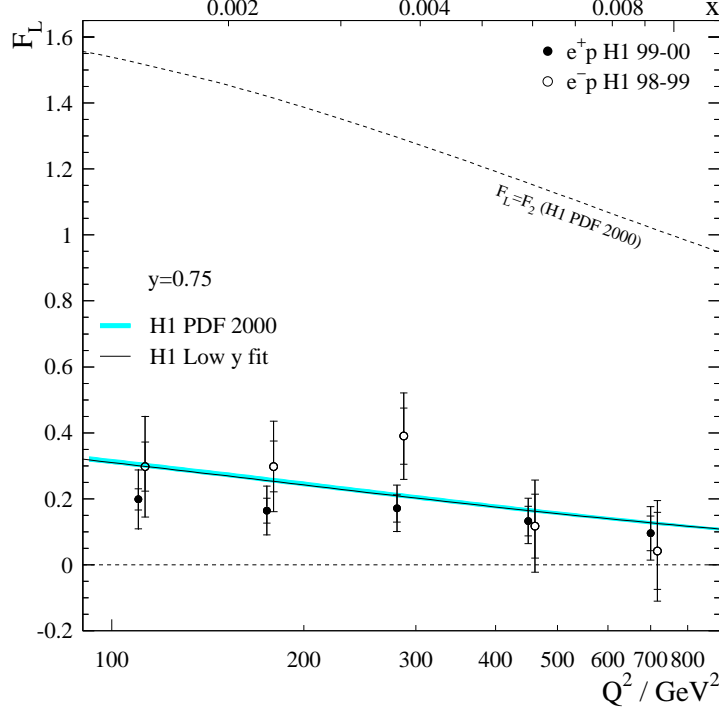


Fig. 50: F_L determined indirectly by H1 at a fixed $y = 0.75$ and high Q^2 is shown as a function of Q^2 (lower scale) or equivalently x (upper scale) for e^+p (closed circles) and e^-p (open circles) data. The inner error bar represents the statistical error, and the outer error bar also includes the systematic error and the uncertainty arising from the extrapolation of F_2 .

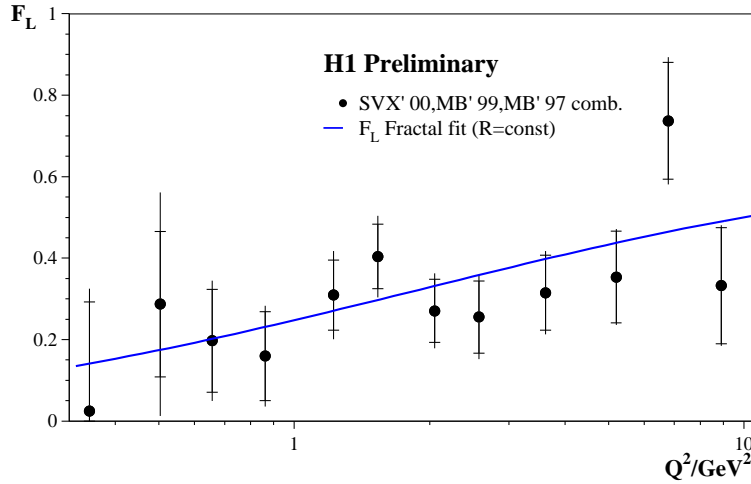


Fig. 51: Q^2 dependence of $F_L(x, Q^2)$ at fixed $y = 0.75$, extracted from the preliminary H1 low- Q^2 data. The solid line shows the prediction of the fractal fit with a constant R .

where some phenomenological model for F_2 is chosen.

An example of such an extraction using a fractal fit for F_2 [180] is shown in Fig. 51, where preliminary H1 results [179] for F_L at $y = 0.75$ in the range of $0.35 \leq Q^2 \leq 8.5 \text{ GeV}^2$ are presented. The data favour a positive, not small F_L at low Q^2 . A drawback of this method is that it reveals a considerable dependence of R on the choice of the F_2 model.

In the derivative method [89, 179], F_L is extracted from the partial derivative of the reduced cross section on y at fixed Q^2

$$\left. \frac{\partial \sigma_r}{\partial \ln y} \right|_{Q^2} = -x \frac{\partial F_2}{\partial x} - \frac{2y^2(2-y)}{Y_+^2} F_L - x \frac{y^2}{Y_+} \frac{\partial F_L}{\partial x} \quad (56)$$

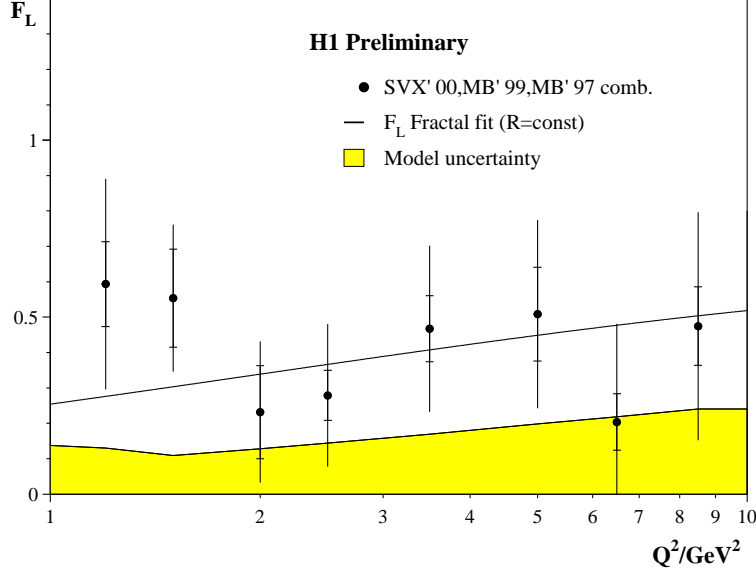


Fig. 52: Structure function F_L extracted by H1 using the derivative method. The solid line shows the prediction of the fractal fit with a constant R . The inner error bars represent statistical uncertainties, the outer error bars represent statistical and systematic uncertainties added in quadrature. The solid (yellow) band indicates the model uncertainty.

which is dominated by the F_L -dependent term at high y . The term proportional to $\partial F_L/\partial x$ is negligible for moderately varying parametrisations of F_L . For low Q^2 values the rise of F_2 is weak. The change of the term $x\partial F_2/\partial x$ for the two assumptions: no rise at low x , i.e. $\partial F_2/\partial x = 0$, and $F_2 \propto x^{-\lambda}$ is numerically significantly smaller than the experimental precision for $\partial\sigma_r/\partial\ln y$. Therefore the derivative method provides a means for determining F_L at low Q^2 with minimal phenomenological assumption. On the other hand, the errors obtained with the derivative method turn out to be significantly larger than those from the shape method.

The preliminary results of F_L extraction from H1 HERAI data [179] are presented in Fig. 52. The residual dependence of the measurement on the assumption made for F_2 is estimated by a comparison with results obtained assuming an F_2 which is flat in y . The lower bound on F_L obtained this way is depicted as a solid band in the figure.

4.2.3 Details of Direct F_L Measurements

The H1 and ZEUS analysis procedures involve a measurement of the inclusive cross section at $y > 0.1$. In this range, the kinematic variables x , y and Q^2 are most accurately reconstructed using the polar angle, θ_e , and the energy, E'_e , of the scattered electron according to

$$y = 1 - \frac{E'_e}{E_e} \sin^2 \frac{\theta_e}{2}, \quad Q^2 = \frac{E'_e{}^2 \sin^2 \theta_e}{1 - y}, \quad x = \frac{Q^2}{ys}. \quad (57)$$

Reaching the high y values necessary for the F_L determination requires a measurement of the scattered electron with energy down to a few GeV. The electron candidate is selected as an isolated electromagnetic energy deposition (cluster) in a calorimeter. The crucial analysis issue at high- y region is the identification of the scattered electron, and the estimation of the hadronic background which occurs when a particle from the hadronic final state mimics the electron signal. Most of background events are photoproduction (γp) events with $Q^2 \approx 0$ in which the final state electron is scattered at low angles (high θ)⁴⁶ and thus escapes through the beam pipe.

The γp background suppression is performed in several steps. Firstly, calorimeter shower estimators are utilised which exploit the different profiles of electromagnetic and hadronic showers. Secondly, background

⁴⁶The z axis of the right-handed coordinate systems used by H1 and ZEUS is defined by the direction of the incident proton beam with the origin at the nominal ep interaction vertex. Consequently, small scattering angles of the final state particles correspond to large polar angles in the coordinate system.

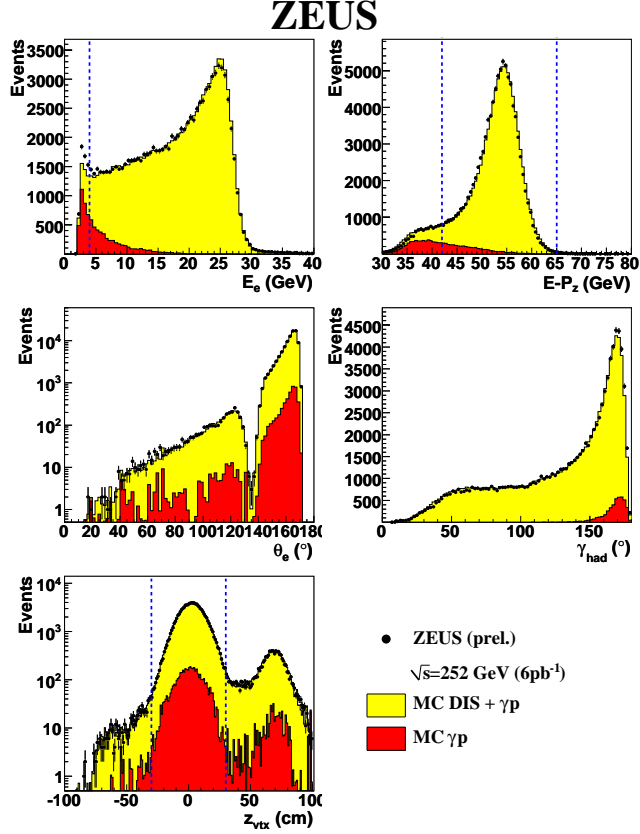


Fig. 53: Comparison of 575 GeV data with the sum of DIS and background simulations for the energy of the scattered electron, total $E - p_z$, theta of the scattered electron, angle of the hadronic final state and z coordinate of the vertex. The dotted lines indicate the cuts applied.

coming from neutral particles, such as π_0 , can be rejected by requiring a track associated to the electron candidate. Furthermore, γp events are suppressed by utilising the energy-momentum conservation. For that, the variable $E - p_z = \sum_i (E_i - p_{z,i})$ is exploited, where the sum runs over energies E_i and longitudinal momentum components $p_{z,i}$ of all particles in the final state. The requirement $E - p_z > 35$ (42) GeV in the H1 (ZEUS) analysis removes events where the escaping electron carries a significant momentum. It also suppresses events with hard initial state photon radiation.

However, at low E'_e the remaining background contribution after such a selection is of a size comparable to or even exceeding the genuine DIS signal. The further analysis steps differ for the H1 and ZEUS analyses as discussed in the following.

ZEUS Analysis Procedure The electron candidates are selected as compact electromagnetic energy depositions in the Uranium Calorimeter (UCal). The position of the candidate is reconstructed using either the Small Angle Rear Tracking Detector (SRTD), which is a high-granularity lead-scintillator calorimeter, or with the Hadron-Electron Separator (HES), which is a silicon detector located in the electromagnetic section of the UCal. The candidates are selected such that $E'_e > 6 \text{ GeV}$ ⁴⁷.

The candidates are validated using information from the tracking devices. The acceptance region for ZEUS tracking is limited to polar angles $\theta_e \lesssim 154^\circ$. The tracking detectors do provide some coverage beyond $\theta_e = 154^\circ$, up to $\theta_e \approx 168^\circ$, however the number of tracking layers is too sparse for full track reconstruction. The hit information from the tracking detectors can still be used. To do this, a “road” is created between the measured interaction vertex and the position of the electron candidate in the calorimeter. Hits in the tracking layers along the road are then counted and compared to the maximum possible number of hits. If too few hits

⁴⁷Cut of $E'_e > 4 \text{ GeV}$ is used for the event selection, although the binning for F_L measurement is chosen such that $E'_e > 6 \text{ GeV}$.

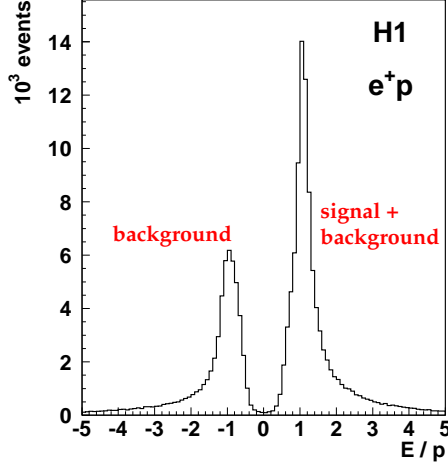


Fig. 54: Distribution of energy over momentum for tracks linked to clusters in the SpaCal with energy from 3.4 to 10 GeV that pass all the medium Q^2 analysis cuts. Tracks with a negative charge are assigned a negative E/p .

are found, the candidate is assumed to be a neutral particle and it is rejected. To ensure the reliability of this method, the scattered electron is required to exit the central drift chamber at a radius $R > 20$ cm. Given that $E'_e > 6$ GeV, this effectively limits the maximal y to $y < 0.8$ and the minimum Q^2 achievable at low y . In the HES analysis, events are measured down to $y = 0.2$ roughly translating to the Q^2 region, $Q^2 > 24$ GeV². No background treatment based on the charge of the candidate is performed.

The remaining γp background is estimated using Monte Carlo (MC) simulations. In order to minimise the model uncertainty of the γp simulation, a pure photoproduction sample is selected using an electron tagger placed close to the beam pipe about 6 meters away from the interaction point in the rear direction. It tags, with almost perfect efficiency and purity, the scattered electrons in such events which are not identified in the main detector and escape down the beam pipe. Photoproduction MC is verified against and normalised to this sample. The normalisation factor is found to be 1 ± 0.1 for all data sets.

Figure 53 shows, as an example, comparisons of the 575 GeV data with simulated distributions, for the energy of the scattered electron, total $E - p_z$, polar angle of the scattered electron, angle of the hadronic final state and the z coordinate of the interaction vertex. A good description of the data by the simulation is observed. A similar level of agreement was found for both, HER and LER data sets.

A full set of systematic uncertainties is evaluated for the cross section measurements. The largest single contribution comes from the electron energy scale uncertainty, which is known to within $\pm 1\%$ for $E'_e > 10$ GeV, increasing to $\pm 3\%$ at $E'_e = 5$ GeV. Other significant contributions are due to the $\pm 10\%$ uncertainty in verifying the Pythia prediction of the γp cross section using the electron tagger. The systematic uncertainty due to the luminosity measurement was reduced by scaling the three cross sections relative to each other. The spread of relative normalisation factor was found to be within the expected level of uncorrelated systematic uncertainty.

H1 Analysis Procedure The H1 measurements of F_L are performed in separate analyses involving different detector components and thus covering different Q^2 ranges. In the high- Q^2 analysis the electron candidate is selected as an isolated electromagnetic energy deposition in the Liquid Argon (LAr) calorimeter which covers the polar angle range $4^\circ < \theta < 153^\circ$. The selected cluster is further validated by a matching track reconstructed in the central tracking device (CT) with an angular acceptance of $15^\circ < \theta < 165^\circ$. In the medium Q^2 analysis the electron candidate is selected in the backward calorimeter SpaCal covering the angular range $153^\circ < \theta < 177.5^\circ$ and is also validated by a CT track. Lower Q^2 values are expected to be accessed in the third analysis, in which the SpaCal cluster is validated by a track in the Backward Silicon Tracker reaching the highest θ . The first measurement of F_L at medium Q^2 is already published [181], and preliminary results of the combined medium-high- Q^2 analysis are available.

The remaining γp background is subtracted on statistical basis. The method of background subtraction

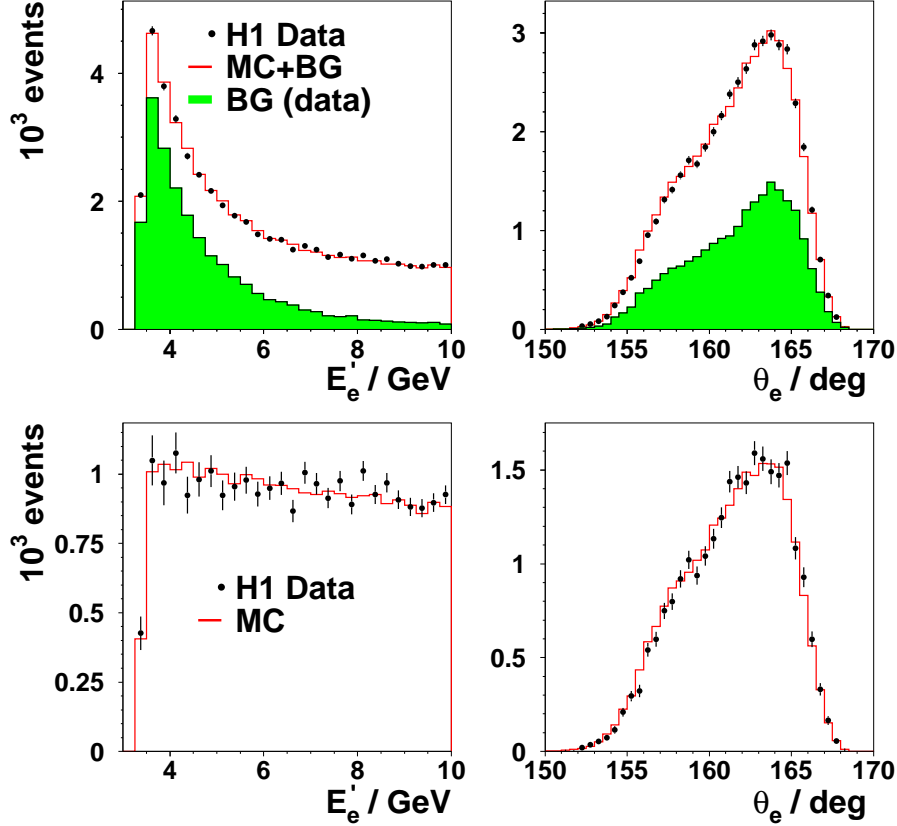


Fig. 55: Top: comparison of the correct sign data (points) with the sum (open histogram) of the DIS MC simulation and background, determined from the wrong sign data (shaded histogram), for the energy E_e' (left) and the polar angle θ_e (right) of the scattered electron, for the 460 GeV data with $E_e' < 10$ GeV. Bottom: as top but after background subtraction.

relies on the determination of the electric charge of the electron candidate from the curvature of the associated track.

Figure 54 shows the E/p distribution of the scattered electron candidates from e^+p interactions with the energy E measured in the SpaCal and the momentum p of the linked track determined by the CT. The good momentum resolution leads to a clear distinction between the negative and positive charge distributions. The smaller peak corresponds to tracks with negative charge and thus represents almost pure background. These tracks are termed wrong sign tracks and events with such candidates are rejected. The higher peak, due to right sign tracks, contains the genuine DIS signal superimposed on the remaining positive background. The size of the latter to first approximation equals the wrong sign background. The principal method of background subtraction, and thus of measuring the DIS cross section up to $y \simeq 0.9$, consists of the subtraction of the wrong sign from the right sign event distribution in each x, Q^2 interval.

The background subtraction based on the charge measurement requires a correction for a small but non-negligible charge asymmetry in the negative and positive background samples, as has been observed previously by H1 [89]. The main cause for this asymmetry lies in the enhanced energy deposited by anti-protons compared to protons at low energies. The most precise measurement of the background charge asymmetry has been obtained from comparisons of samples of negative tracks in e^+p scattering with samples of positive tracks in e^-p scattering. An asymmetry ratio of negative to positive tracks of 1.06 is measured using the high statistics $e^\pm p$ data collected by H1 in 2003-2006. This result is verified using photoproduction events with a scattered electron tagged in a subdetector of the luminosity system.

Figure 55 shows, as an example, comparisons of the 460 GeV high y data with simulated distributions, for the energy and the polar angle of the scattered electron prior to and after subtraction of the background, which is determined using wrong sign data events.

The measurement of F_L as described below relies on an accurate determination of the variation of the

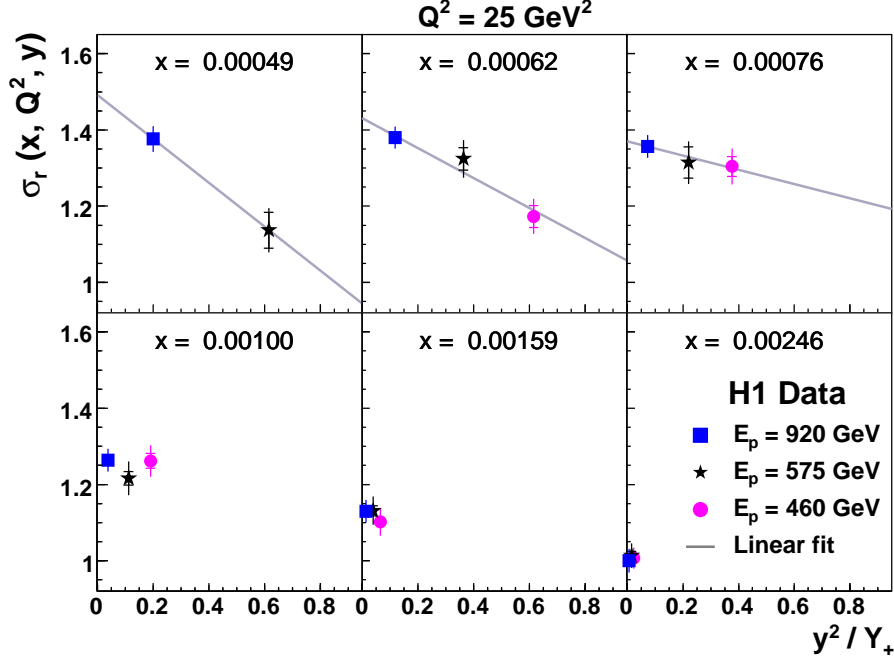


Fig. 56: The reduced inclusive DIS cross section plotted as a function of y^2/Y_+ for six values of x at $Q^2 = 25 \text{ GeV}^2$, measured by H1 for proton beam energies of 920, 575 and 460 GeV. The inner error bars denote the statistical error, the full error bars include the systematic errors. The luminosity uncertainty is not included in the error bars. For the first three bins in x , corresponding to larger y , a straight line fit is shown, the slope of which determines $F_L(x, Q^2)$.

cross section for a given x and Q^2 at different beam energies. In order to reduce the uncertainty related to the luminosity measurement, which presently is known to 5% for each proton beam energy of the 2007 data, the three data samples are normalised relatively to each other. The renormalisation factors are determined at low y , where the cross section is determined by F_2 only, apart from a small correction due to F_L . The relative normalisation is known to within 1.6%.

All correlated and uncorrelated systematic errors combined with the statistical error lead to an uncertainty on the measured cross sections at high y of 3 to 5%, excluding the common luminosity error.

4.2.4 Measurements of $F_L(x, Q^2)$ by H1 and ZEUS

The longitudinal structure function is extracted from the measurements of the reduced cross section as the slope of σ_r versus y^2/Y_+ , as can be seen in eq. 53. This procedure is illustrated in Fig. 56. The central F_L values are determined in straight-line fits to $\sigma_r(x, Q^2, y)$ as a function of y^2/Y_+ using the statistical and uncorrelated systematic errors.

The first published H1 measurement of $F_L(x, Q^2)$ is shown in Fig. 57, the preliminary ZEUS measurement is presented in Fig. 58. The H1 measured values of F_L are compared with the H1 PDF 2000 fit [18], while the ZEUS F_L values are compared to the ZEUS-JETS PDF fit [170]. Both measurements are consistent and show a non-zero F_L .

The H1 results were further averaged over x at fixed Q^2 , as shown in the left panel of Fig. 59. The averaging is performed taking the x dependent correlations between the systematic errors into account. The averaged values of F_L are compared with H1 PDF 2000 fit and with the expectations from global parton distribution fits at higher order perturbation theory performed by the MSTW [182] and the CTEQ [131, 169] groups. Within the experimental uncertainties the data are consistent with these predictions. The measurement is also consistent with previous indirect determinations of F_L by H1.

In the combined medium-high Q^2 analysis by H1 the Q^2 range is extended up to $Q^2 = 800 \text{ GeV}^2$. The preliminary results are shown in the right panel of Fig. 59. In some Q^2 bins there is an overlap between the SpaCal and LAr measurements which improves the precision of the F_L extraction as compared to the pure

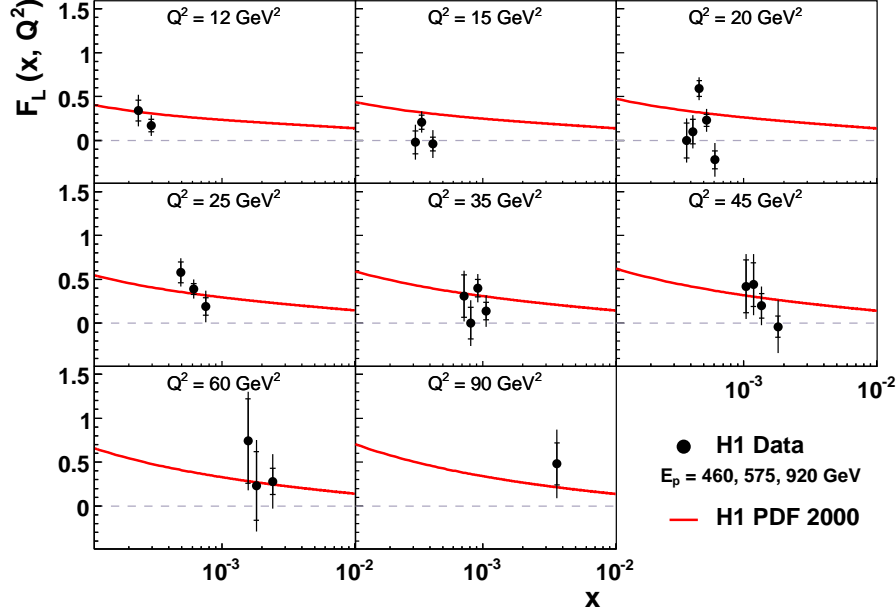


Fig. 57: The longitudinal proton structure function $F_L(x, Q^2)$ measured by the H1 collaboration. The inner error bars denote the statistical error, the full error bars include the systematic errors. The curves represent the H1 PDF 2000 fit.

ZEUS

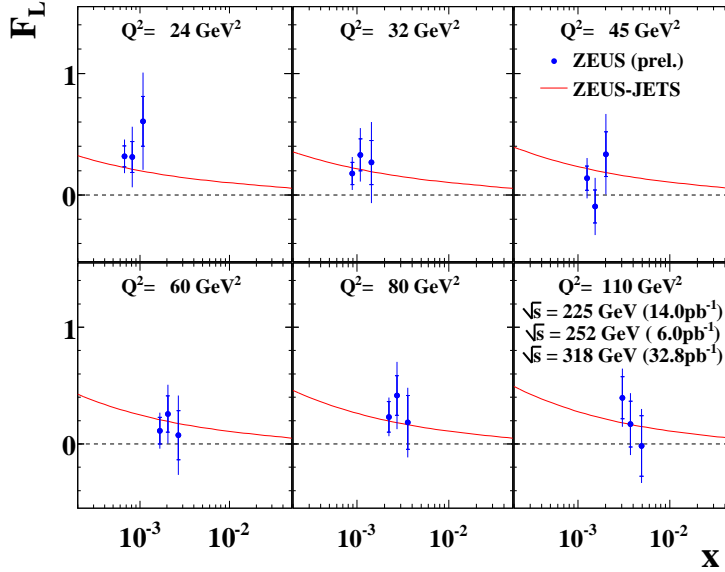


Fig. 58: The longitudinal proton structure function $F_L(x, Q^2)$ measured by the ZEUS collaboration. The inner error bars denote the statistical error, the full error bars include the systematic errors. The curves represent the ZEUS-JETS PDF fit.

SpaCal analysis.

4.2.5 Summary

Direct measurements of the proton structure function F_L have been performed in deep inelastic ep scattering at low x at HERA. The F_L values are extracted by the H1 and ZEUS collaborations from the cross sections measured at fixed x and Q^2 but different y values. This is achieved by using data sets collected with three different proton beam energies. The H1 and ZEUS results are consistent with each other and exhibit a non-zero F_L . The measurements are also consistent with the previous indirect determinations of F_L by H1. The results confirm DGLAP NLO and NNLO QCD predictions for $F_L(x, Q^2)$, derived from previous HERA data,

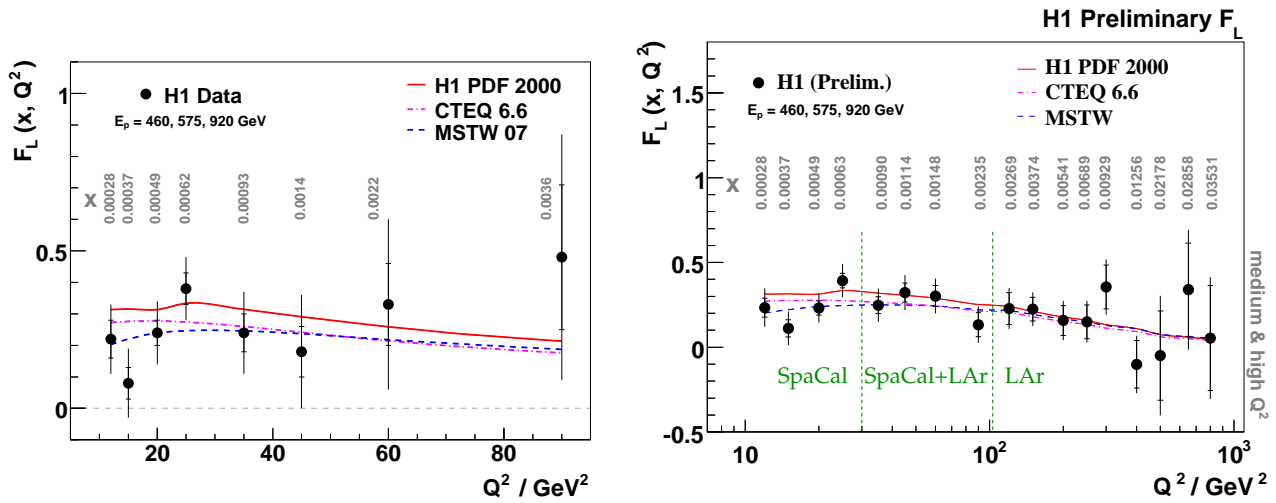


Fig. 59: The proton structure function F_L shown as a function of Q^2 at the given values of x : a) first direct measurement at HERA by H1; b) preliminary H1 results combining SpaCal and LAr analyses. The inner error bars denote the statistical error, the full error bars include the systematic errors. The luminosity uncertainty is not included in the error bars. The solid curve describes the expectation on F_L from the H1 PDF 2000 fit using NLO QCD. The dashed (dashed-dotted) curve depicts the expectation of the MSTW (CTEQ) group using NNLO (NLO) QCD. The theory curves connect predictions at the given (x, Q^2) values by linear extrapolation.

which are dominated by a large gluon density at low x .

5 PROTON-PROTON LUMINOSITY, STANDARD CANDLES AND PDFS AT THE LHC⁴⁸

5.1 Introduction

The Large Hadron Collider (LHC) is expected to start colliding proton beams in 2009, and is expected to reach design parameters in energy and luminosity sometime later and deliver a few fb^{-1} per year of data at the 14 TeV collision energy.

During the past 15 years many theoretical calculations and experimental simulations have demonstrated a huge potential to perform many accurate tests of the Standard Model (SM) with LHC data, which could yield insight into new physics mechanisms.

To make these tests, the experiments identify a particular signature X and observe, using a variety of selection criteria, a certain number of events in a given data taking period. After correcting this event rate for backgrounds and the selection efficiency, the number is converted into a cross section. The cross section, $\sigma_{pp \rightarrow X}$ can be compared with theoretical predictions⁴⁹ according to the formula: $N_{corrected} = \sigma_{pp \rightarrow X} \times L_{pp}$ where L_{pp} is the recorded proton proton luminosity.

Besides the statistical errors of a measurement, the systematic error is related to the uncertainties from the L_{pp} determination, the background and efficiency corrections within the detector acceptance and from extrapolations into the uncovered very forward rapidity regions. The interpretation of an observed cross section within the SM requires further the knowledge of the theoretical cross section. Thus the uncertainties of the proton parton distribution function (PDF) have to be considered also.

In this Section we describe the status and perspectives of the ATLAS, CMS and LHCb, the three LHC pp collision detectors [183], to determine the proton proton luminosity normalization. The investigated methods are known and studied since many years and can be separated into the absolute (1) direct and (2) indirect proton proton luminosity determination. A third approach (3) tries to measure and calculate final states only relative to well understood reactions which depend on the parton-parton luminosity and are as such largely independent of the knowledge of the pp luminosity.

- Absolute, direct or indirect, proton proton luminosity normalization: If the absolute approach is used, the interpretations of a measured reaction cross section depends still on the knowledge of parton distribution function (PDF), which must be obtained from other experiments. Examples are:
 - The proton proton luminosity normalization is based on the measurements of the beam currents and shapes. While the beam currents can be accurately determined using beam transformers, the beam profiles are more difficult to determine directly and usually constitute the dominant source of uncertainty on a luminosity measurement using this technique. The use of the machine luminosity determination using beam parameter measurements [184] and [185] will be described in Section 5.3.1. Alternatively one can try to measure the beam profiles also within the experiments using the precision vertex detectors. A short description of this idea, currently pursued within the LHCb collaboration, is also given in Section 5.3.1.
 - The simultaneous measurements of a pair of cross sections that are connected with each other quadratically via the optical theorem. A well known example of this is the measurement of the total inelastic cross section and the elastic cross section at very high pseudorapidities $|\eta| \approx 9$ and will be described in Section 5.3.3.
So called instantaneous or real time luminosity measurements are based on “stable” high rate measurements of particular final state reactions. Once the ratio of such reactions to the pp luminosity determination has been measured, those reactions can be subsequently used as independent luminosity monitors. Some possibilities are discussed in Section 5.3.4.
 - The indirect absolute proton proton luminosity normalization is based on the theoretically well understood “two photon” reaction $pp \rightarrow pp\mu\mu$ [186, 187] (Section 5.3.5). This reaction could perhaps be considered as the equivalent of the luminosity counting in e^+e^- experiments using forward Bhabha scattering.

⁴⁸Contributing authors: J. Anderson, M. Boonekamp, H. Burkhardt, M. Dittmar, V. Halyo, T. Petersen

⁴⁹Alternatively, one can also apply a Monte Carlo simulation to the theoretical prediction and compare the number of background corrected events directly.

- Indirect pp luminosity measurements use final states, so called “standard candles”, with well known theoretical cross sections (Section 5.4).

Obviously, the resulting proton proton luminosity can only be as good as the theoretical and experimental knowledge of the “standard candle” reaction. The theoretically and experimentally best understood LHC reactions are the inclusive production of W and Z bosons with subsequent leptonic decays. Their large cross section combined with experimentally well defined final states, e.g. almost background free Z and W event samples can be selected over a relative large rapidity range, makes them the preferred LHC “standard candle” reaction. Other interesting candidates are the high p_t jet - boson ($= \gamma, W$ or Z) final states. The indirect luminosity method requires also some knowledge of the PDFs, and of course, if one follows this approach, the cross section of the “standard candle” reaction becomes an input and can not be measured anymore. Thus, only well understood reactions should be considered as candidate reactions.

- pp luminosity independent relative rate measurements using “standard candle” reactions. In addition to the above indirect pp luminosity determinations, “standard candle” reactions allow to perform luminosity independent relative event rate calculations and measurements. This approach has already been used successfully in the past and more details were discussed during the past HERA-LHC workshop meetings [1]. For some reactions, this approach appears to be much easier and more accurate than standard cross section measurements and their interpretations. Perhaps the best known example at hadron colliders is the measurement and its interpretation of the production ratio for Z and W events, where Tevatron experiments have reached accuracies of about 1-2% [188, 189]. Another example is related to relative branching ratio and lifetime measurements as used for b-flavored hadrons.

Furthermore the rapidity distributions of leptonic W and Z decays at the LHC are very sensitive to the PDF parameterization and, as was pointed out 10 years ago [190], one can use these reactions to determine the parton luminosity directly and very accurately over a large x ($=$ parton momentum/proton momentum) range. In fact, W and Z production with low transverse momentum were found in this analysis to be very sensitive to $q\bar{q}$ luminosities, and the jet-boson final states, e.g. the jet- γ , Z, W final states at high transverse momentum are sensitive to the gluon luminosity.

In the following we attempt to describe the preparations and the status of the different luminosity measurements and their expected accuracies within ATLAS, CMS and LHCb. Obviously, all these direct and indirect methods should and will be pursued. In Section 5.5 we compare the advantages and disadvantages of the different methods. Even though some methods look more interesting and rewarding than others, it should be clear from the beginning that as many independent pp luminosity determinations as possible need to be performed by the experiments.

We also try to quantify the systematic accuracies which might be achieved over the next few years. As these errors depend somewhat on the overall achieved luminosity, we need in addition a hypothetical working scenario for the first 4 LHC years. We thus assume that during the first year, hopefully 2009, data at different center of mass energies can be collected by ATLAS and CMS. During the following three physics years we expect that 10 TeV will be the highest collision energy in year I and that at most 100 pb^{-1} can be collected. We assume further that during the following two years the design energy of 14 TeV can be achieved and that a luminosity of about 1 fb^{-1} and 10 fb^{-1} can be collected respectively per year. During the first few years similar numbers are expected for the LHCb experiment. However once the LHC reaches the first and second phase design luminosity of $10^{33}/\text{cm}^2/\text{sec}$ and $10^{34}/\text{cm}^2/\text{sec}$ it is expected that the LHCb experiment will run at an average luminosity of $2 \times 10^{32}/\text{cm}^2/\text{sec}$ (resulting in about $2 \text{ fb}^{-1}/\text{per year}$).

5.2 Luminosity relevant design of ATLAS/CMS and LHCb

In the following we give a short description of the expected performance with respect to lepton and jet identification capabilities. Especially the electron and muon measurement capabilities are important for the identification of events with leptonic decays of W and Z bosons.

Both ATLAS and CMS are large so called omni purpose experiments with a large acceptance and precision measurement capabilities for high p_t electrons, muons and photons. Currently, the simulations

of both experiments show very similar performance for a large variety of LHC physics reactions with and without jets. For the purpose of this Section we focus on the possibility to identify the production of inclusive W and Z decays with subsequent decays to electrons and muons. Both experiments expect excellent trigger accuracies for isolated leptons and it is expected that electrons and muons with momenta above 20-25 GeV can be triggered with high efficiency and up to $|\eta|$ of about 2.5. The special design of the ATLAS forward muon spectrometer should allow to detect muons with good accuracy even up to $|\eta|$ of 2.7.

The operation of ALFA, a very far forward detector placed about 240 m down the beam line, is envisaged by the ATLAS collaboration to provide an absolute luminosity measurement, either using special optics LHC running and the use of the optical theorem or using the total cross section measurement from the dedicated TOTEM experiment installed near CMS; results from this device can be expected from 2010 and on-wards. In addition to absolute luminosity measurements from ALFA the two detectors LUCID and the Zero-Degree-Calorimeter (CDC) [191] are sensitive to the relative luminosity at time scales of single bunch crossings.

A similar approach for absolute and relative luminosity measurements is foreseen by the CMS experiment. Here it is planned that dedicated forward detectors, the Hadron Forward Calorimeter (HF) and the ZDC device provide similar results as the ones in ATLAS.

Another technique that is expected to be available early on is a luminosity-independent measurement of the pp total cross section. This will be done using a forward detector built by the TOTEM experiment [192].

The LHCb experiment [193] has been designed to search for New Physics at the LHC through precision measurements of CP violating observables and the study of rare decays in the b-quark sector. Since the $b\bar{b}$ pairs resulting from the proton-proton collisions at the LHC will both be produced at small polar angles and in the same forward or backward cone, LHCb has been designed as a single-arm forward spectrometer covering the pseudo rapidity range $1.9 < \eta < 4.9$. The LHCb tracking system, which is composed of a silicon vertex detector, a warm dipole magnet and four planar tracking stations, will provide a momentum resolution of $\delta P/P = (0.3 + 0.0014P/GeV)\%$ [194]. Muon identification is primarily achieved using a set of five planar multi-wire proportional chambers, one placed in front of the calorimeter system and four behind, and it is expected that for the momenta range 3-150GeV/c an identification efficiency of $\sim 98\%$ and an associated pion dis-identification rate of $\sim 1\%$ will be achieved. The reconstruction of primary and secondary vertices, a task of crucial importance at b physics experiments, will be virtually impossible in the high particle multiplicity environment present with the nominal LHC running luminosity of $10^{34} cm^{-2}s^{-1}$ - LHCb has therefore been designed to run at the lower luminosity of $2 \times 10^{32} cm^{-2}s^{-1}$.

Recent LHCb simulations have shown that leptonic W and Z decays to muons can be identified with a small background in the forward and very forward rapidity region starting from η of 1.9 and up to values larger than 4. As will be discussed later in more detail, the common muon acceptance region for the three LHC experiments between 1.9 and about 2.5 will allow to cross check and normalize the W and Z measurements in this region. Consequently the unique large rapidity from 2.5 to 4.9 can be used by LHCb to investigate the very low x range of the PDFs for the first time.

The absolute luminosity at LHCb will be obtained either directly, by making measurements of the beam parameters, or indirectly via a measurement of the event rate of an accurately predicted physics process.

As will be explained in the following Sections, all experiments will try to perform as many as possible direct and indirect absolute and relative luminosity measurements and will, if available, at least during the first years, also use luminosity numbers from the machine group.

5.2.1 Lepton triggering and W/Z identification.

Generally, the lepton trigger selections depend on the instantaneous luminosity and some pre-scaling might eventually be needed. However, current simulations by all experiments show that the envisaged $|\eta|$ and p_t thresholds will not limit the measurement accuracies of leptons originating from W and Z decays.

The lepton trigger selections that are generally perceived to be used for most W and Z related analyses are very similar in ATLAS and CMS as indicated in Table 9.

Trigger and reconstruction efficiencies for leptonic W and Z decays within the acceptance of the detec-

Experiment	Trigger selection e		Trigger selection μ	
	p_T	$ \eta $	p_T	$ \eta $
ATLAS	25 GeV	2.5	20 GeV	2.7
CMS	20 GeV	2.5	20 GeV	2.1
LHCb*	–	–	2.5 GeV	1.9-4.9

Table 9: For ATLAS and CMS the lepton trigger/selection p_t thresholds are given for single isolated leptons. *For the LHCb threshold is given for the muon pair mass instead of single muons and only positive values of η are covered.

tors have been estimated for ATLAS to be 97.7% and 80.0% for electrons and 84.3% and 95.1% for muons, respectively. The reconstruction efficiency includes the trigger efficiencies and the off-line electron and muon selections used later to identify clean inclusive W and Z event samples [195].

The current equivalent trigger and off-line efficiencies for CMS are about 85% and 77% for electrons and combined about 85% for single muons [196]. Similar efficiency numbers for muons from W and Z decays are expected within the LHCb acceptance region [197]. Current simulations show that these numbers can be determined with high accuracies, reaching perhaps 1% or better, at least for isolated leptons⁵⁰ which have a transverse momentum some GeV above the trigger thresholds. For lower momenta near the thresholds or for additional special trigger conditions somewhat larger systematic uncertainties can be expected.

5.3 Direct and indirect absolute pp luminosity measurements

Three different absolute proton proton luminosity measurements are discussed in this Section. (1) The machine luminosity determination using beam parameter measurements [198], (2) the luminosity independent total pp cross section measurement combined with the measurement of the elastic pp scattering rate [192] and (3) the measurement of the “two photon” reaction $pp \rightarrow pp\mu\mu$ [186, 187]. As will be discussed in more detail in Section 5.5, only method (3) can be performed during the normal collision data taking. For method (1) some special methods, which take the actual detector performance during each run into account, need to be developed. Method 2 uses a two phase approach (a) a special machine optics run with low luminosity to determine the total cross section and (b) a normalization to some high rate final state reactions which can be counted during normal physics runs.

5.3.1 Proton-proton luminosity from machine parameters⁵¹

The luminosity for colliding beams can be directly obtained from geometry and numbers of particles flowing per time unit [184]. This can be used to determine the absolute LHC luminosity from machine parameters without prior knowledge of pp scattering cross sections. The principle is briefly outlined here. More details can be found in [185].

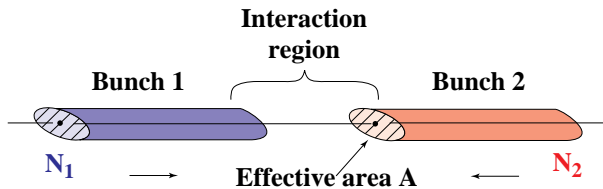


Fig. 60: Luminosity from particles flux and geometry.

For two bunches of N_1 and N_2 particles colliding head-on in an interaction region as sketched in Fig.60 with the frequency f the luminosity is given as

$$\mathcal{L} = \frac{N_1 N_2 f}{A_{\text{eff}}} . \quad (58)$$

⁵⁰As isolated high p_t photons are triggered essentially like electrons similar accuracies for both particle types can be assumed.

⁵¹Contributing author: H. Burkhardt

A_{eff} is the *effective transverse area* in which the collisions take place. For a uniform transverse particle distribution, A_{eff} would be directly equal to the transverse beam cross section. More generally, the effective area can be calculated from the overlap integral of the two transverse beam distributions $g_1(x, y)$, $g_2(x, y)$ according to

$$\frac{1}{A_{\text{eff}}} = \int g_1(x, y) g_2(x, y) dx dy . \quad (59)$$

For equal Gaussian beams

$$g_1 = g_2 = \frac{1}{2\pi\sigma_x\sigma_y} \exp \left[-\frac{x^2}{2\sigma_x^2} - \frac{y^2}{2\sigma_y^2} \right] \quad (60)$$

we obtain for head-on collisions $A_{\text{eff}} = 4\pi\sigma_x\sigma_y$ so that

$$\mathcal{L} = \frac{N_1 N_2 f}{4\pi\sigma_x\sigma_y} . \quad (61)$$

The collision frequency f is accurately known. The number of particles circulating in a storage ring is measured using beam current transformers to roughly 1% precision [198].

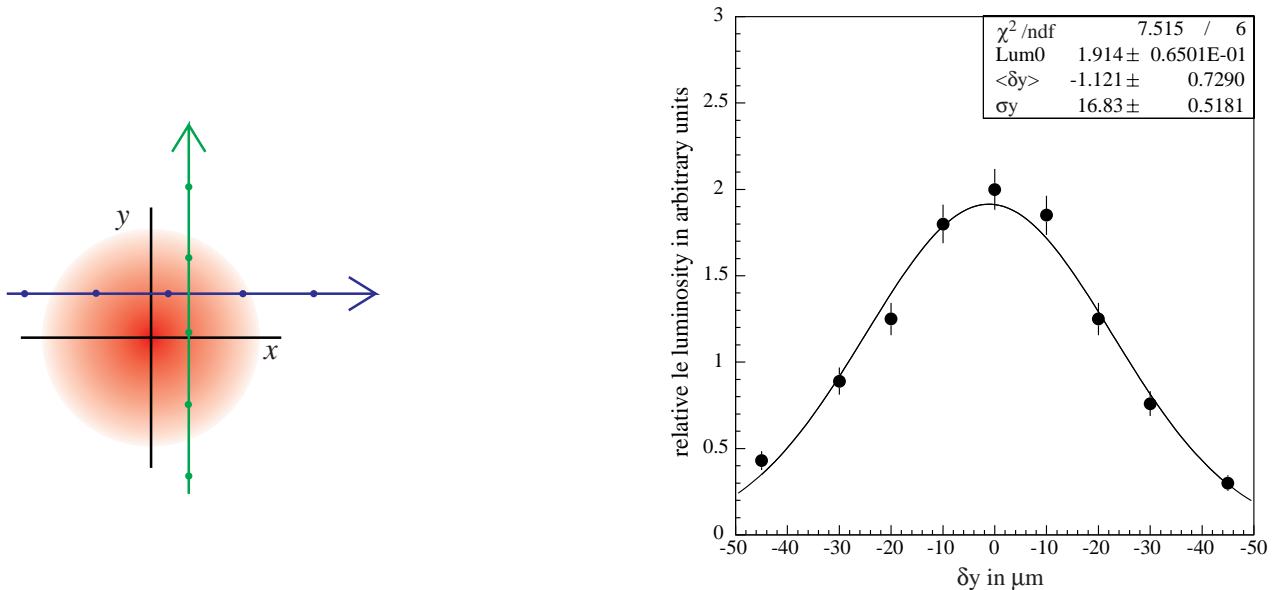


Fig. 61: Schematic view of the steps involved in an orthogonal separation scan proposed for the LHC (left) and a possible result in one direction (based on early LEP data) shown on the right.

The main uncertainty in the absolute luminosity determination from machine parameters is expected to originate in the knowledge of the transverse beam dimensions. Safe operation of the LHC requires a rather good knowledge of the optics and beam sizes and we expect that this should already allow a determination of the luminosity from machine parameters to about 20 – 30 percent. A much better accuracy can be obtained when the size of the overlap region at the interaction points is determined by measuring the relative luminosity as a function of lateral beam separation, as illustrated in Fig. 61. This technique was pioneered at the ISR [199] and allowed to reduce the uncertainty to below 1%, [200, 201].

For the more complicated LHC and early operation, a 10% overall uncertainty in the absolute LHC machine luminosity calibration should be a realistic goal. The actual precision will depend on the running time and effort which is invested. A relatively small number of scans under favorable beam conditions will in principle be sufficient to obtain and verify the reproducibility in the absolute luminosity calibration. While fast scans may always be useful to optimize collisions, we assume that any dedicated, detailed luminosity scans will become obsolete when the other, cross section based luminosity determinations described in these proceedings allow for smaller uncertainties.

Optimal running conditions are moderate bunch intensities, large bunch spacings, no crossing angle and $\beta^* = 2$ m or larger. These conditions are in fact what is proposed anyway for the initial LHC operation with 43 – 156 bunches per beam. Statistics are not expected to be a problem. For early operation at top energy (10 - 14 TeV) with 43 bunches and 4×10^{10} particles per bunch, before beams are squeezed, at a $\beta^* = 11$ m, we already expect luminosities of the order of $10^{30} \text{ cm}^{-2}\text{s}^{-1}$ resulting in event rates of 10^4 Hz, for a cross section of 0.01 barn as typical for the low angle luminosity monitors.

From the LHC injectors, we expect bunch by bunch variations of about 10% in intensity and 20% in emittance. For the large spacing between bunches in the operation with up to 156 bunches, there is no need for crossing angles at the interaction points. Parasitic beam-beam effects will be negligible. All bunches in each beam will follow the same equilibrium orbit and collide at the same central position.

Calibration runs require good running conditions and in particular good beam lifetimes. Bunch by bunch differences are not expected to change significantly during a scan. Storing bunch intensities at the beginning and end of a scan and using one set of timed averaged bunch intensities for a scan should be sufficient. To avoid any bias, it will be important to use the correct pairing of bunch intensities and relative luminosities in the calculation of absolute bunch luminosities according to Eq. 58, before any summing or averaging over different bunches.

We are currently preparing an on-line application for automatic luminosity scans⁵². Scan parameters like range, step size and duration can be set before the start of the scan. Once the parameters are defined, it is possible to launch automatic horizontal and vertical separation scans in the LHC interactions regions. For a detailed scan, we may choose a range from -4 to $+4 \sigma$ in nominal beam size in steps of 0.5σ , resulting in 17 equidistant points. If we wait 1 s between points to allow for the magnets to change and for 2 s integration time, the scan time would still be below a minute per plane. Details are currently being worked out in close collaboration with the experiments. Exchanging all data bunch-by-bunch at a 1 Hz rate between the machine control room (CCC) and the experiments would be rather demanding and risks to saturate current capacities.

For the initial running, it will be sufficient to exchange average values at about 1 Hz rate. It allows quality monitoring and the determination of the peak position. For the detailed off line analysis, we only have to rely on local logging and timing information synchronized to at least 1 s precision at the beginning of the scan. With fixed time interval defined and saved before the scan, this allows for off-line synchronization of the detailed data and a complete bunch by bunch analysis.

5.3.2 Direct measurements of the absolute luminosity at LHCb

LHCb plans to measure the absolute luminosity using both the Van Der Meer scan, [199], and beam-gas techniques following a more recently proposed method [202]. Here one tries to determine the transverse beam profiles at colliding beam experiments utilizing the precision vertex detectors found at modern HEP experiments to reconstruct beam gas interactions near the beams crossing point. The vertex resolution in the transverse direction at LHCb can be parameterized by the relation

$$\sigma_{x,y} = \frac{100\mu\text{m}}{\sqrt{N_{tracks}}} \quad (62)$$

where N_{tracks} is the number of tracks originating from the vertex. Since the nominal transverse bunch size at LHCb will be $100\mu\text{m}$, the reconstruction of beam-gas vertices's, which will have a track multiplicity of ~ 10 , will enable the measurement of the colliding bunch profiles and the beam overlap integral. This method is currently under investigation by the LHCb collaboration and is expected to result in a luminosity measurement with an associated uncertainty of 3-5%.

5.3.3 Absolute pp luminosity from specialized detectors and from the total cross section measurement

ATLAS and CMS are planning to perform absolute and relative pp luminosity measurements using dedicated luminosity instruments.

⁵²Done by Simon White, as part of his PhD thesis work on the LHC machine luminosity determination

Three particular luminosity instruments will operate around the ATLAS interaction point. The absolute luminosity measurement will be provided by ALFA [191] placed 240m down the beam line and due to operate in 2010. This measurement requires some special optics low luminosity running of the LHC and should be able to measure the very low angle Coulomb scattering reaction. The expected precision is of the order 3%, depending on yet unknown LHC parameters during running. The ALFA detector can also measure the absolute luminosity using the optical theorem if the Coulomb region can not be reached. Extrapolating the elastic cross section to very low momentum transfer $t = 0$ and using the total cross section as measured by TOTEM [192] (located at the CMS interaction point) current simulations indicate that a precision of about 3% might also be reached with this method. In addition to absolute luminosity measurements from ALFA, LUCID and a Zero-Degree-Calorimeter (ZDC) [191] are sensitive to the relative single bunch crossings luminosity. LUCID and ZDC will however not give absolute measurements.

A similar approach is currently foreseen by the CMS collaboration [203].

5.3.4 Real time relative luminosity measurements

A large number of instantaneous relative luminosity measurements have been discussed during the past years by ATLAS, CMS and LHCb and more details can be found in the three presentations given during the “standard candle” session of this workshop [204]. As an example we outline in the following some ideas discussed within CMS.

Multiple techniques capable of providing suitable luminosity information in real time have been identified in CMS. One technique employs signals from the forward hadron calorimeter (HF) while another, called the Pixel Luminosity Telescope (PLT), uses a set of purpose-built particle tracking telescopes based on single-crystal diamond pixel detectors. At this writing, the PLT has not been formally approved, but is under study. The methods based on signals from the HF described are the ones being most vigorously pursued.

Two methods for extracting a real-time relative instantaneous luminosity with the HF have been studied. The first method is based on “zero counting,” in which the average fraction of empty towers is used to infer the mean number of interactions per bunch crossing. The second method called “EtSum method” exploits the linear relationship between the average transverse energy per tower and the luminosity.

Outputs of the QIE chips used to digitize the signals from the HF PMTs on a bunch-by-bunch basis are routed to a set of 36 HCAL Trigger and Readout (HTR) boards, each of which services 24 HF physical channels. In order to derive a luminosity signal from the HTR, an additional mezzanine board called the HF luminosity transmitter (HLX) is mounted on each of the HTR boards. The HLX collects channel occupancy and E_T sum data to create eight histograms: two sets of three occupancy histograms, one E_T -sum histogram, and one additional occupancy histogram. These histograms comprise about 70 KB of data, which is transmitted at a rate of approximately 1.6 Mbps to a dedicated luminosity server via an Ethernet switch that aggregates the data from multiple HLX boards for further processing.

Although all HF channels can be read by the HLX, MC studies indicate that the best linearity is obtained using only the inner four η rings. The algorithm has been optimized to minimize sensitivity to pedestal drifts, gain changes and other related effects. Both “Zero Counting” and the “EtSum” method have demonstrated linearity up to LHC design luminosity. A statistical error of about 1% will be achieved at $\text{fewtimes} \times 10^{31} \text{cm}^{-2}\text{s}^{-1}$. Hence the dominant error on the absolute luminosity will result from the normalization of the online relative luminosity.

5.3.5 Proton-proton luminosity from the reaction $pp \rightarrow pp\mu\mu$

The QED process $pp \rightarrow pp\mu^+\mu^-$, where a $\mu^+\mu^-$ pair is produced via photon-photon scattering, was first proposed for luminosity measurements at hadron colliders in [186]. At the LHC such pairs will be predominantly produced with small transverse momenta, at small polar angles and in the same forward or backward cone.

All three experiments are considering to use the well calculated $pp \rightarrow pp\mu\mu$ process for measuring absolute luminosity. The theoretical understanding of this QED photon-photon scattering reactions is considered to be accurate to better than 1%. Consequently this final state is thus often considered to be the perfect theoretical luminosity process. However, the experimental identification of this process requires to select muon

pairs with low mass and within a well understood acceptance. The measurement of this reaction at a hadron collider appears to be much more difficult than the corresponding measurements of the reaction $ee \rightarrow ee\mu\mu$ at LEP. The systematic measurement error for example in L3 and after several years of data taking was about $\pm 3\%$ [205]

Current simulations by the three LHC experiments indicate that the final state can be identified using straight forward criteria. For ATLAS and CMS one finds that about 1000 accepted events could at best be expected for an integrated luminosity of 1 fb^{-1} , resulting in a statistical error of about $\pm 3\%$.

For example the ATLAS study selects oppositely charged back-to-back muon tracks with $p_T > 6 \text{ GeV}$ and $|\eta| < 2.2$ with an invariant mass less than 60 GeV and a common vertex with no other tracks originating from it (isolation), yields a cross section of 1.33 pb . Thus, about 1300 events can be expected for running periods with a luminosity of 1 fb^{-1} and yielding a potential statistical error of 3% . However, backgrounds not only from pile up events will be a critical issue. Some proton tagging with high luminosity roman pots is currently investigated but this will certainly reduce the accepted cross section and introduce additional acceptance errors. Similar conclusions have been reached by simulations performed within the CMS collaboration. Consequently, both experiments expect that, during the coming years, this reaction will be mainly used as a cross check of the other methods.

The cross section for this process where both muons lie inside the LHCb acceptance and have a combined invariant mass greater than 2.5 GeV is $\approx 88 \text{ pb}$. The expected uncertainty is perhaps 1% or smaller and comes mainly from rescattering corrections [187], i.e. strong interactions between the interacting protons.

The feasibility of using the elastic two photon process $pp \rightarrow p + \mu^+\mu^- + p$ to make luminosity measurements at LHCb was first explored in [206] and has recently been investigated in more detail by members of the LHCb collaboration [207]. A variety of background processes have been studied: dimuons produced via inelastic two-photon fusion and double pomeron exchange; low mass Drell-Yan pairs; QCD processes such as $b\bar{b} \rightarrow \mu^+\mu^- + X$; and the combinatoric backgrounds caused by K/π mis-identification. A simple offline selection has been developed that requires: the dimuon pair transverse momentum to be less than $50 \text{ MeV}/c$; the dimuon invariant mass to be in the range $2.5 \text{ GeV}/c^2 < M_{\mu\mu} < 20 \text{ GeV}/c^2$; and a charged particle multiplicity of less than 3 (i.e. the event should contain a $\mu^+\mu^-$ pair and no other charged particles). These criteria select $\sim 27\%$ of the signal events that pass the trigger and are reconstructed and result in a background contamination that is $(4.1 \pm 0.5(\text{stat.}) \pm 1.0(\text{syst.}))\%$ of the signal level with the dominant contribution due K/π mis-identification. Overall it is expected that $\sim 10^4$ $pp \rightarrow p + \mu^+\mu^- + p$ events will be triggered, reconstructed and selected at LHCb during one nominal year of data taking (2 fb^{-1}). Systematic uncertainties on a luminosity measurement at LHCb using this channel are estimated to be $\sim 1.31\%$ and are dominated by the uncertainty on the predicted cross section for events containing dimuons produced via double pomeron exchange, an uncertainty that is expected to be reduced in the near future. A measurement of the absolute luminosity at LHCb using this channel and a dataset of 2 fb^{-1} will therefore be possible with an associated uncertainty of $\sim 1.5\%$.

In summary, the accurate measurement of this theoretically well understood reaction looks like an interesting challenge for the LHC experiments. Interesting results can be expected once integrated luminosities of 5 fb^{-1} and more can be accumulated for ATLAS and CMS and about 1 fb^{-1} for LHCb. Of course, it remains to be proven, if the systematic uncertainties under real data taking conditions can indeed be reduced to the interesting 1% level.

5.4 Indirect and relative pp luminosity measurements

The methods to measure the absolute proton proton luminosity and their limitations have been described in the previous chapter.

In this Section we will describe the possibilities to measure the luminosity indirectly using well defined processes, so called ‘‘Standard Candles’’ and their use to further constrain the PDFs and discuss the possibility to ‘‘measure’’ directly the parton-parton luminosities.

Before describing the details of these indirect approaches, a qualitative comparison of luminosity measurements at e^+e^- colliders and hadron colliders might be useful. The most important difference appears

to be that in the e^+e^- case one studies point like parton parton interactions. In contrast, at hadron hadron interactions one studies the collision of protons and other hadrons made of quarks and gluons. As a result, in one case the Bhabha elastic scattering reaction $e^+e^- \rightarrow e^+e^-$ at low Q^2 reaction can be calculated to high accuracy and the observed rate can be used as a luminosity normalization tool. In contrast, the elastic proton proton scattering cross section can not be calculated at the LHC nor at any other hadron colliders. As a consequence, absolute normalization procedures depend always on the measurement accuracy of the pp total cross section. Even though it is in principle possible to determine the pp total cross section in a luminosity independent way using special forward detectors like planned by the TOTEM or the ALFA experiments, the accuracy will be limited ultimately and after a few years of LHC operation to perhaps a few %.

Furthermore, as essentially all interesting high Q^2 LHC reactions are parton parton collisions, the majority of experimental results and their interpretation require the knowledge of parton distribution functions and thus the parton luminosities.

Following this reasoning, more than 10 years ago, the inclusive production of W and Z bosons with subsequent leptonic decays has been proposed as the ultimate precision parton parton luminosity monitor at the LHC [190]. The following points summarize the arguments why W and Z production are indeed the ideal “Standard Candles” at the LHC.

- The electroweak couplings of W and Z bosons to quarks and leptons are known from the LEP measurements to accuracies smaller than 1% and the large cross section of leptonic decays W and Z bosons allows that these final states can be identified over a large rapidity range with large essentially background free samples.
- Systematic, efficiency corrected counting accuracies within the detector acceptance of 1% or better might be envisioned during the early LHC running. In fact it is believed that the relative production rate of W and Z can be measured within the detector acceptance with accuracies well below 1%.
- Theoretical calculations for the W and Z resonance production are the most advanced and accurately known LHC processes. Other potentially more interesting LHC reactions, like various diboson pair production final states are expected to have always larger, either statistical or systematic, experimental and theoretical uncertainties than the W and Z production.
- The current PDF accuracies, using the latest results from HERA and other experiments demonstrate that the knowledge of the quark and anti quark accuracies are already allowing to predict the W and Z cross at 14 TeV center of mass energies to perhaps 5% or better. The measurable rapidity and p_t distributions of the Z boson and the corresponding ones for the charged leptons from W decays can be used to improve the corresponding parton luminosity functions.

Obviously, the use of W and Z bosons as a luminosity tool requires that the absolute cross section becomes an input, thus it can not be measured anymore. As a result this method has been criticized as being “a quick hack at best”. In contrast, advocates of this method point out that this would not be a noticeable loss for the LHC physics program.

5.4.1 Using the reaction $pp \rightarrow Z \rightarrow \ell^+\ell^-$ to measure L_{pp}

Very similar and straight forward selection criteria for the identification of leptonic Z decays, depending somewhat on the detector details and the acceptance region, are applied by ATLAS, CMS and LHCb. In the following the current selection strategy in ATLAS and LHCb are described.

5.4.2 Measuring Z and W production, experimental approaches in ATLAS

The ATLAS W and Z cross section measurements are based on the following selections in the electron and muon channels:

- A typical selection of $W \rightarrow e\nu$ requires that events with “good” electrons have to fulfill the additional kinematic acceptance criteria:
 $p_T > 25 \text{ GeV}, |\eta| < 1.37$ or $1.52 < |\eta| < 2.4$.

The criteria for $W \rightarrow \mu\nu$ muons are similar where $p_T > 25$ GeV and $|\eta| < 2.5$. is required. Furthermore, in order to classify the event as a W event, the reconstructed missing transverse momentum and the transverse mass should fulfill $E_T(miss) > 25\text{GeV}$ and $m_T(W) > 40$ GeV.

- The selection of $Z \rightarrow ee$ and $Z \rightarrow \mu\mu$ requires that a pair of oppositely charged electrons or muons is found. Due to lower background the electrons should have $p_T > 15$ GeV and $|\eta| < 2.4$ and their invariant mass should be between 80-100 GeV.

Similar criteria are applied for the muons with $p_T > 15$ GeV and $|\eta| < 2.5$. The reconstructed mass should be between 71-111 GeV.

Following this selection and some standard Monte Carlo simulations, the expected number of reconstructed events per 10 pb^{-1} at $\sqrt{s} = 14$ TeV are about 45000, 5500 for W and Z decays to electrons and 60000, and 5000 for the decays to muons, respectively. Thus, even with a small data sample of only 10 pb^{-1} , the statistical uncertainty for the Z counting comes close to 1% in each channel.

Systematic uncertainties from the experimental selection are dominated by the Z efficiency determination and from backgrounds in the W selection. Other sources of uncertainties originate from the knowledge of energy scale and the resolution. The lepton efficiencies are evaluated by considering $Z \rightarrow \ell\ell$ events and using the so called “tag and probe” method, like for example described by the D0 experiment [188, 189]. The efficiency uncertainty associated with the precision of this method has been estimated for a data sample of 50 pb^{-1} (1 fb^{-1}) of data to be 2% (0.4%) for W and 3% (0.7%) for Z events. The backgrounds for W events are of the order 4% in the electron channel and 7% in the muon channel. The main contributions are from other W or Z decays, and are thus well understood, leading to background uncertainties of the order 4% for both channels if a sample 50 pb^{-1} is analyzed. For much larger samples it is expected that uncertainties at or below 1% can be achieved. The backgrounds for the Z decays are very small, and can be determined accurately from mass spectrum, and hence does not carry any sizable uncertainty. It has been demonstrated, that the detector scales and resolutions can be determined very accurately [195], and the associated uncertainties are therefore also close to negligible.

Some detailed studies demonstrate that eventually the systematic error between 1-2% or even smaller might be achieved for the W and Z counting and within the detector acceptance up to rapidities of about 2.5.

In order to use this number for the pp luminosity determination the total inclusive W and Z cross-section at NNLO can be used. These have been calculated to be 20510 pb and 2015pb, respectively [208]. Variations in models, floating parameters, and other theoretical uncertainties lead to significant variations in the estimates. The uncertainties on these calculation are estimated to be 5% or smaller. This uncertainty appears to be currently dominated by the PDF uncertainties needed to extrapolate to the experimentally uncovered large rapidity region. More discussions about these uncertainties can be found for example at [209] and [210].

It can be assumed that the detailed studies of the rapidity distributions within the acceptance region with W and Z decays might eventually lead to further error reductions.

5.4.3 Measuring Z production, experimental approach in LHCb

The uncertainty on the predicted Z production cross section at the LHC comes from two sources: the uncertainty on the NNLO partonic cross section prediction [208], which contributes an uncertainty of $< 1\%$, and uncertainties in our understanding of the proton Parton Distribution Functions (PDFs) which, for the latest MSTW fit [39], contribute an uncertainty of $\sim 3\%$ for Z bosons produced with rapidities in the range $-5 < y < 5$.

A measurement of the Z production rate at LHCb via the channel $Z \rightarrow \mu^+\mu^-$, which provides a final state that is both clean and fully reconstructible, can be achieved with high efficiency and little background contamination. In addition, since the dimuon trigger stream at LHCb [211] requires two muons with an invariant mass larger than 2.5GeV and a summed transverse momentum ($P_T^1 + P_T^2$) greater than 1.4GeV, a high trigger efficiency of $\sim 95\%$ is expected for these events. A variety of background sources for this channel have been investigated: other electroweak processes such as $Z \rightarrow \tau^+\tau^-$ where both taus decay to muons and neutrinos; QCD processes such as $b\bar{b} \rightarrow \mu^+\mu^- + X$; and events where two hadrons with an invariant mass near the Z mass are both mis-identified as muons. To deal with these backgrounds an off-line selection has been developed [212] that requires: the dimuon invariant mass to be within 20 GeV of the Z mass; the higher and

lower transverse momentum muons to be greater than 20 GeV and 15 GeV respectively; the impact parameter of both muons is consistent with the primary vertex; and both muons have associated hadronic energy that is less than 50 GeV. For $Z \rightarrow \mu^+\mu^-$ events that are triggered and reconstructed at LHCb, these off-line selection criteria will select $91 \pm 1\%$ of the signal events while reducing the background to $(3.0 \pm 2.9)\%$ of the signal level with the dominant contribution due to the combinatoric backgrounds from pion and kaon mis-identification. It is expected that these backgrounds can be well understood from real data or removed using muon isolation criteria. Overall it is expected that $Z \rightarrow \mu^+\mu^-$ events will be triggered, reconstructed and selected at LHCb at a rate of $\sim 190 \text{ evts}/\text{pb}^{-1}$. Systematic uncertainties have also been investigated and it is expected that with as little as 5 pb^{-1} of data the experimental efficiency (trigger, tracking, muon identification etc.) can be measured with an uncertainty of $\sim 1.5\%$ enabling a luminosity measurement with an uncertainty of $\sim 3.5\%$.

5.4.4 PDF and relative parton-parton luminosity measurements

Theoretically well understood reactions at the LHC offer the possibility to use their rapidity distributions to improve today's knowledge of PDFs. Especially the resonance production of W and Z bosons with leptonic decays with low and high transverse momentum and the production of isolated high p_t γ -Jet events have been demonstrated to be very sensitive to the relative parton distribution functions. Simulations from ATLAS and CMS have shown that experimental errors on these rapidity regions up to $|y|$ of about 2.5 can probably be performed with accuracies eventually reaching perhaps 1% or better. The possibility to cross-check the measurements with W and Z decays to (a) electron(s) and (b) muon(s) and between both experiments will of course help to reach the accuracy.

During the past years simulation studies from the LHCb collaboration have shown that the experiment has a unique potential to extend the acceptance region from ATLAS and CMS for muons up to rapidity values at least up to 4.5. Furthermore, the existing overlap region for y between 1.9 and 2.5 should allow to reduce normalisation uncertainties. Obviously, these rapidity values are understood as being reasonably accurate but qualitative values and more precise values will be defined once real data will allow to define a well understood fiducial volume of the detectors.

In addition, the LHCb collaboration has investigated the possibility to identify clean samples of very low mass Drell-Yan mu-pair events. The results indicate that such pairs can be measured within their acceptance region down to masses of 5 GeV. Such a measurement would in principle allow to measure PDFs for x values approaching extremely low values of 10^{-6} for the first time [213].

It should be clear that such measurements, which are known to be very sensitive to quark, antiquark and gluon relative parton luminosities will not allow an absolute PDF normalisation. Such an improvement of absolute PDF normalisation would require the accurate knowledge of the proton-proton luminosity to better than today's perhaps $\pm 3\%$ PDF accuracy obtained from the HERA measurements over a large x range and obviously lower Q^2 . The alternative approach to combine the relative parton luminosities over the larger x , Q^2 range using the sum rules has, to our knowledge, so far not been studied in sufficient detail.

A more detailed analysis of the different experimental approaches to improve the PDFs are interesting but are beyond the scope of this note about the luminosity. Nevertheless we hope that the experimentalists of the three collaborations will start to combine their efforts and will pursue the PDF measurements, in direct collaboration with theorists, during the coming years.

5.5 Comparing the different pp luminosity measurements

A relatively large number of pp luminosity measurements has been proposed and the most relevant have been discussed in this note. Here we try to give a critical overview of the different methods and their potential problems. Despite these advantages and disadvantages it should be clear that it is important to perform as many as possible independent luminosity methods during the coming years.

- **The machine luminosity determination using beam parameters:**

This method will be pursued independently of the experiments and its main purpose will be to optimize the performance of the LHC and thus providing a maximum number of physics collisions for the

experiments. The potential to use this number as an almost instantaneous absolute luminosity number with uncertainties of perhaps $\pm 10\%$ (and eventually $\pm 5\%$), assuming that non gaussian tails of the beam can be controlled to this accuracy will certainly be useful to the experiments. Of course the experiments would lose somewhat their “independence” and still need to combine this number with their actual active running time.

However, one should remember that the Tevatron experiments did not use this method for their measurements.

The method to determine the beam size using the LHCb precision vertex detector look very promising and it is hoped that their approach might result in a pp luminosity measurement with an associated uncertainty of 3-5%.

- **Total cross section and absolute luminosity normalisation with specialized far forward Detectors:**

The luminosity independent total pp cross section measurement is planned by the TOTEM collaboration and by the ALFA detector. Using these numbers both ATLAS and CMS plan to obtain the pp luminosity from the counting of the pp elastic scattering counting numbers from the forward detectors which thus depend on the knowledge of the total cross section measurement. In order to obtain this number some few weeks of special optics and low luminosity LHC running are required. As all LHC experiments are very keen to obtain as quickly as possible some reasonable luminosity at 14 TeV center of mass energy it is not likely that those special LHC data taking will happen during the first year(s) of data taking. Furthermore, despite the hope that the total cross section can be determined in principle with an interesting accuracy of $\pm 1\%$, it remains to be demonstrated with real LHC running. In this respect it is worth remembering that the two independent measurements of the total cross section at the Tevatron differed by 12% while much smaller errors were obtained by the individual experiments. As a result the average value with an error of $\pm 6\%$ was used for the luminosity normalisation.

- **Luminosity determination using $Z \rightarrow \ell\ell$:**

This method provides an accurate large statistic relative luminosity number. It will be as accurate as the theoretical cross section calculation, which is based on the absolute knowledge of the PDFs from other experiments, from unknown higher order corrections and their incomplete Monte Carlo implementation. Today's uncertainties are estimated to be about 5%. It has been estimated, assuming the experiments perform as expected, that the potential Z counting accuracy within the acceptance region including efficiency corrections might quickly reach $\pm 1\%$. The extrapolation to the uncovered rapidity space, mainly due to the worse knowledge of the PDFs in this region, increases the error to perhaps 3%. Taking other theoretical uncertainties into account an error of $\pm 5\%$ is currently estimated. Of course, advocates of the Z normalisation method like to point out that the real power of this method starts once relative measurements, covering similar partons and similar ranges of the parton distribution functions will be performed with statistical errors below 5%. Examples where such a normalization procedure looks especially interesting are the relative cross section measurements of $N(Z)/N(W)$, $N(W^+)/N(W^-)$, high mass Drell-Yan events with respect to Z events and diboson final states decaying to leptons. Of course, correlations and anticorrelations between quark and gluon dominated production rates exist and need to be carefully investigated before similar advantages for the gluon PDFs can eventually be exploited. The loss of an independent Z cross section measurement would of course be a fact of life.

- **pp luminosity from the reaction $pp \rightarrow pp\mu\mu$:**

A measurement of this reaction offers in principle a direct and theoretically accurate proton proton luminosity value. Unfortunately current simulations from the experiments indicate that the accepted cross section is relatively small and only a few 1000 events can be expected per fb^{-1} . The different simulation results indicate that the backgrounds can be suppressed sufficiently without increasing the experimental systematics too much. The current simulation results indicate that small systematic errors of perhaps 1-2% might eventually be achievable⁵³ once a yearly luminosity of 5-10 fb^{-1} in ATLAS and CMS (2 fb^{-1} for LHCb) might be recorded. It remains to be seen if muons with transverse momenta well below 20 GeV can indeed be measured as accurately as muons with transverse momenta above 25 GeV.

⁵³It might be interesting to study the experience from similar measurements at the experimentally ideal conditions of LEP, where uncertainties above $\pm 3\%$ have been reported [205].

5.5.1 Which luminosity accuracy might be achievable and when

Of course the potential time dependent accuracy of the different luminosity methods can only be guessed today as such numbers depend obviously on the LHC machine performance during the coming years. For the purpose of this Section we are mainly interested in measurements at the 14 TeV center of mass energy and assume that the following “data samples” would define such “years”. Of course, it could be hoped that the luminosity and energy increase would go much faster resulting in “some” shorter LHC years. Thus we assume that the first 14 TeV year, currently expected to be 2010, will correspond to 0.1 fb^{-1} , followed by a 1 fb^{-1} year. During the third and fourth year ATLAS and CMS expect to collect about 5 fb^{-1} and 10 fb^{-1} while LHCb expects to collect roughly 2 fb^{-1} per year. We assume further that the special optics low luminosity data taking periods requiring perhaps a few weeks for TOTEM and similar for ALFA will take only place during the year when more than 1 fb^{-1} per year or more can be expected.

As a result, for the first two 14 TeV running years, realistic luminosity numbers could come from (1) the machine group and (2) from the indirect method using the inclusive production of Z events with leptonic decays.

As has been pointed out in Section 5.3.1 the method (1) would, without any additional efforts by the machine group, allow a first estimate with a $\pm 20\text{-}30\%$ luminosity accuracy. We assume however that, due to the delay of the real 14 TeV start to 2010, enough resources could be found that people within the machine group could carefully prepare for the necessary beam parameter measurements and that the experiments will do the corresponding efforts to correct such a machine luminosity number for real detector data taking one could hope for a 10% measurement for 2010 and a 5% accuracy for 2011.

In contrast, method (2) would by definition be an integrated part of any imaginable experimental LHC data taking period. In fact, if enough attention is put into the Z counting method, the data expected during 2010 running might already reach statistical errors of $\pm 2\%$ per 5 pb^{-1} periods. Thus perhaps about 10-20 such periods could be defined during the entire year and systematic errors for the lepton efficiency correction within the detector acceptance could reach similar $\pm 2\text{-}3\%$ accuracies. During the following years these errors might decrease further to 1% or better. Once the rate of any “stable” simple high rate final states and even trigger rates relative to the Z counting rate has been determined, such relative event rates can be used subsequently to track the “run” luminosity and even the real time luminosity with similar accuracy.

Theoretical limitations of the cross section knowledge, not expected to improve without LHC data taking, would limit the accuracy to about $\pm 5\%$. The expected detailed analysis of the 2010 rapidity distributions of W, Z and γ -jet events will allow some improvements for the years 2011 and beyond. We can thus expect that appropriate ratio measurements like the cross section ratio measurements of Z/W^\pm and W^-/W^+ will already reach systematic accuracies of $\pm 1\text{-}2\%$ during 2010 and 1% or better in the following years. Measurement of b physics, either in LHCb or in ATLAS and CMS might in any case prefer to perform luminosity independent measurements and relate any of the “new” measurements to some relatively well known and measurable B-hadron decays.

It is also worth pointing out that currently no other high Q^2 reaction has been envisioned, which might be measurable to a systematic precision of better than 5-10% and a luminosity of up to 1 fb^{-1} . In addition, most of the interesting high Q^2 electroweak final states will unfortunately even be limited for the first few LHC years to statistical accuracies to 5% or more.

The prospect for the other luminosity measurements start to become at earliest interesting only once a few 100 pb^{-1} can be recorded. Consequently one can expect to obtain a statistically interesting accuracy from the reaction $pp \rightarrow pp\mu\mu$ after 2010. Similar, it looks unlikely that low luminosity special optics run will be performed before 2011. Consequently one might hope that few % accurate total cross section numbers become available before the 2012 data taking period will start.

5.6 Summary and Outlook

A large variety of potentially interesting pp luminosity measurements, proposed during the past 10-15 years, are presented in this Section.

Realistically only the machine luminosity measurement and the counting of the Z production might

reach interesting accuracies of 5% before 2011. For all practical purposes it looks that both methods should be prepared in great detail before the data taking at 14 TeV collision energies will start in 2010.

We believe that a working group, consisting of interested members of the three pp collider experiments and interested theorists, should be formed to prepare the necessary Monte Carlo tools to make the best possible use of the soon expected W and Z data, not only for the pp luminosity normalization but even more for the detailed investigations of the parton parton luminosity determination and their use to predict other event rates for diboson production processes and high mass Drell-Yan events.

6 OUTLOOK: THE PDF4LHC INITIATIVE⁵⁴

This document demonstrates the vast amount of progress that has taken place in the last years on pinning down the PDFs of the proton, as well as the dramatic increase in awareness of the impact of PDFs on the physics program of LHC experiments. The HERALHC workshop has acted as a regular forum for working meetings between the experiments, PDF phenomenologists and theorists. In the course of this workshop, it was realized that the momentum on the PDF studies should be kept and perhaps even focused more on the LHC, in order to continue the discussions, investigations and further work towards improving our knowledge on the PDFs.

Clearly, LHC will need the best PDFs, especially for precision measurements, setting of limits in searches, and even for discoveries. Ideally the ATLAS and CMS (and LHCb and ALICE) analyses should follow a common procedure for using PDFs and their uncertainties in their key analyses. Such a common procedure, across the experiments, is being used in other contexts, such as significance estimates in searches. Also, changing frequently the PDFs in the software of the experiments, e.g. for cross-checks or the determination of error bands, is often non-trivial (e.g. due to the inter-connection with parameter choices for underlying event modeling, showering parameters and so on) and sometimes impractical if CPU intensive detector simulations are involved. LHC studies therefore will need both good central values for the PDFs to start with, and a good estimate of the associated uncertainties.

This has triggered the so called PDF4LHC initiative. PDF4LHC offers a discussion forum for PDF studies and information exchange between all stake-holders in the field: the PDF global fitter groups, such as CTEQ and MSTW; the current experiments, such as the HERA and Tevatron ones; QCD theorists and the LHC experimental community. The PDF4LHC initiative started in 2008. More details and links to the meetings so far can be found on the PDF4LHC web site [214].

The mission statement of PDF4LHC is:

- Getting the best PDFs, including the PDF uncertainties, based on the present data.
- Devise strategies to use future LHC data to improve the PDFs.

All this needs a close collaboration between theorists and those that are preparing to make the measurements. In order to reach the first goal, the PDF4LHC forum aims to stimulate discussions and trigger further comparison exercises across the PDF community, in order to select one or a limited number of possible strategies that can be adapted to determine and use PDFs. For the second goal, PDF4LHC should also be a forum for discussions on how to include measurements from the LHC to constrain PDFs: what should be measured at LHC, and correspondingly calculated in theory. Such measurements include W and Z production and asymmetries, di-jet production, hard prompt photons, Drell-Yan production, bottom and top quark production, Z -shape fits and Z +jets measurements. One expects that some of these channels can already be studied with first data, hence we need to prepare for that well in advance.

The following issues are part of the program for in depth discussions via topical workshops, some of which took place already in 2008 [214].

- Data to be included in the PDFs. Would we get better results with a selection of data to be used? New data will become available such as $F_L(x, Q^2)$, and combined data from H1/ZEUS. Can we extract more from the data?
- Determination of PDF uncertainties, including the statistical treatment of the data.
- Theoretical uncertainties and regions/processes where they matter: higher-order corrections; heavy flavour treatment; low- x (and high- x) resummation; other PDFs like unintegrated PDFs (and GPDs).
- PDFs for usage Monte Carlo generators.

One can expect that the LHC experiments most likely will be using for most of their studies the PDF sets and errors that are delivered by either one of the CTEQ or MSTW family. Hence it is important that the lessons learned from exercises on studies of the systematics on PDFs will be adapted by these main global PDF providers. PDF4LHC aims to advice the experiments in the use for PDFs for the LHC, based on the discussions, results and future consensus at the forum. The experience and results from HERAPDFs, and PDFs from other groups, like the Neural Net or Alekhin ones are extremely valuable in this discussion and will

⁵⁴Contributing author: A. de Roeck

serve as crucial input in studies to demonstrate how well we actually know the parton distributions. Several important benchmark exercises have been already performed and are reported in section 3 of this report.

A special case are the PDFs for Monte Carlo generators. For experiments it is important that generated events be kinematically distributed close to the distribution of the real data, such that the simulated and reconstructed Monte Carlo events can be used in a straightforward way to calculate efficiencies for e.g. experimental cuts in an analysis. In case the initially generated distribution does not resemble the data close enough, the Monte Carlo samples need to be reweighted, with all its possible drawbacks. Since calculations based on LO Matrix Elements and LO PDFs are known not to describe the data well, and NLO Matrix Element based generators to date have so far only a restricted number of processes implemented, studies are ongoing on so called “improved LO” PDFs, which try to cure some of the LO PDF drawbacks. Examples are given in [215]. This is yet another part of the discussions in the PDF4LHC forum

In short, it is crucial that the work started here continues, with discussions and studies on PDFs and their uncertainties, the impact of the upcoming data on future PDF determinations and more, all with special focus on the needs for the LHC. The PDF4LHC initiative will offer a framework to do all this.

ACKNOWLEDGEMENTS

This work was supported in part by the following grants and agencies: the European network HEPTOOLS under contract MRTN-CT-2006-035505; ANR-05-JCJC-0046-01 (France) PRIN-2006 (Italy); MEC FIS2004-05639-C02-01; (Spain) and the Scottish Universities Physics Alliance (UK).

References

- [1] Dittmar, M. and others, *Parton distributions: Summary report for the HERA - LHC workshop*. Preprint hep-ph/0511119, 2005.
- [2] Larin, S. A. and van Ritbergen, T. and Vermaseren, J. A. M., Nucl. Phys. **B427**, 41 (1994).
- [3] Larin, S. A. and Nogueira, Paulo and van Ritbergen, T. and Vermaseren, J. A. M., Nucl. Phys. **B492**, 338 (1997).
- [4] Retey, A. and Vermaseren, J. A. M., Nucl. Phys. **B604**, 281 (2001).
- [5] Moch, S. and Vermaseren, J. A. M. and Vogt, A., Nucl. Phys. **B688**, 101 (2004).
- [6] Vogt, A. and Moch, S. and Vermaseren, J. A. M., Nucl. Phys. **B691**, 129 (2004).
- [7] Moch, S. and Vermaseren, J. A. M. and Vogt, A., Phys. Lett. **B606**, 123 (2005).
- [8] Vermaseren, J. A. M. and Vogt, A. and Moch, S., Nucl. Phys. **B724**, 3 (2005).
- [9] Vogt, Andreas and Moch, Sven and Vermaseren, Jos, Nucl. Phys. Proc. Suppl. **160**, 44 (2006).
- [10] Moch, S. and Rogal, M., Nucl. Phys. **B782**, 51 (2007).
- [11] Moch, S. and Rogal, M. and Vogt, A., Nucl. Phys. **B790**, 317 (2008).
- [12] Vogt, A. and Moch, S. and Rogal, M. and Vermaseren, J. A. M., Nucl. Phys. Proc. Suppl. **183**, 155 (2008).
- [13] Moch, S. and Rogal, M. and Vogt, A. and Vermaseren, J.A.M. In preparation.
- [14] Yao, W. -M. and others, J. Phys. **G33**, 1 (2006).

- [15] Yang, Un-Ki and others, Phys. Rev. Lett. **86**, 2742 (2001).
- [16] Tzanov, M. and others, Phys. Rev. **D74**, 012008 (2006).
- [17] Onengut, G. and others, Phys. Lett. **B632**, 65 (2006).
- [18] Adloff, C. and others, Eur. Phys. J. **C30**, 1 (2003).
- [19] Chekanov, S. and others, Eur. Phys. J. **C32**, 1 (2003).
- [20] Aktas, A. and others, Phys. Lett. **B634**, 173 (2006).
- [21] Chekanov, S. and others, Phys. Lett. **B637**, 210 (2006).
- [22] Mangano, Michelangelo L. and others, *Physics at the front-end of a neutrino factory: A quantitative appraisal*. Preprint hep-ph/0105155, 2001.
- [23] Dainton, J. B. and Klein, M. and Newman, P. and Perez, E. and Willeke, F., JINST **1**, P10001 (2006).
- [24] Zeller, G. P. and others, Phys. Rev. Lett. **88**, 091802 (2002).
- [25] Aktas, A. and others, Phys. Lett. **B632**, 35 (2006).
- [26] Davidson, S. and Forte, S. and Gambino, P. and Rius, N. and Strumia, A., JHEP **02**, 037 (2002).
- [27] McFarland, Kevin S. and Moch, Sven-Olaf, *Conventional physics explanations for the NuTeV $\sin^2(\theta(W))$* . Preprint hep-ph/0306052, 2003.
- [28] Dobrescu, Bogdan A. and Ellis, R. Keith, Phys. Rev. **D69**, 114014 (2004).
- [29] Kretzer, Stefan and others, Phys. Rev. Lett. **93**, 041802 (2004).
- [30] Buras, Andrzej J., Rev. Mod. Phys. **52**, 199 (1980).
- [31] Gorishnii, S. G. and Larin, S. A. and Surguladze, L. R. and Tkachov, F. V., Comput. Phys. Commun. **55**, 381 (1989).
- [32] Larin, S. A. and Tkachov, F. V. and Vermaseren, J. A. M. NIKHEF-H-91-18.
- [33] Broadhurst, David J. and Kataev, A. L. and Maxwell, C. J., Phys. Lett. **B590**, 76 (2004).
- [34] Van Neerven, W. L. and Vogt, A., Nucl. Phys. **B603**, 42 (2001).
- [35] Paschos, E. A. and Wolfenstein, L., Phys. Rev. **D7**, 91 (1973).
- [36] Moch, S. and Vermaseren, J. A. M. and Vogt, A., Nucl. Phys. **B726**, 317 (2005).
- [37] Catani, Stefano and de Florian, Daniel and Rodrigo, German and Vogelsang, Werner, Phys. Rev. Lett. **93**, 152003 (2004).
- [38] Lai, H. L. and others, JHEP **04**, 089 (2007).
- [39] Thorne, R. S. and Martin, A. D. and Stirling, W. J. and Watt, G., *Parton Distributions for the LHC*. Preprint 0706.0456, 2007.
- [40] Vogt, Andreas (2007). arXiv:0707.4106.
- [41] Fadin, Victor S. and Kuraev, E. A. and Lipatov, L. N., Phys. Lett. **B60**, 50 (1975).
- [42] Balitsky, I. I. and Lipatov, L. N., Sov. J. Nucl. Phys. **28**, 822 (1978).
- [43] Fadin, Victor S. and Lipatov, L. N., Phys. Lett. **B429**, 127 (1998).

- [44] Camici, G. and Ciafaloni, M., Phys. Lett. **B412**, 396 (1997).
- [45] Ciafaloni, Marcello and Camici, Gianni, Phys. Lett. **B430**, 349 (1998).
- [46] Marzani, Simone and Ball, Richard D. and Falgari, Pietro and Forte, Stefano, Nucl. Phys. **B783**, 143 (2007).
- [47] Ciafaloni, M. and Colferai, D. and Colferai, D. and Salam, G. P. and Stasto, A. M., Phys. Lett. **B576**, 143 (2003).
- [48] Ciafaloni, M. and Colferai, D. and Salam, G. P. and Stasto, A. M., Phys. Rev. **D68**, 114003 (2003).
- [49] Catani, S. and Ciafaloni, M. and Hautmann, F., Nucl. Phys. **B366**, 135 (1991).
- [50] Catani, S. and Hautmann, F., Nucl. Phys. **B427**, 475 (1994).
- [51] Bialas, A. and Navelet, H. and Peschanski, Robert B., Nucl. Phys. **B603**, 218 (2001).
- [52] White, C. D. and Peschanski, Robert B. and Thorne, R. S., Phys. Lett. **B639**, 652 (2006).
- [53] Altarelli, Guido and Ball, Richard D. and Forte, Stefano, Nucl. Phys. **B575**, 313 (2000).
- [54] Altarelli, Guido and Ball, Richard D. and Forte, Stefano, Nucl. Phys. **B621**, 359 (2002).
- [55] Altarelli, Guido and Ball, Richard D. and Forte, Stefano, Nucl. Phys. **B674**, 459 (2003).
- [56] Altarelli, Guido and Ball, Richard D. and Forte, Stefano, Nucl. Phys. **B742**, 1 (2006).
- [57] Ball, Richard D. and Forte, Stefano, Nucl. Phys. **B742**, 158 (2006).
- [58] Ball, Richard D., Nucl. Phys. **B796**, 137 (2008).
- [59] Altarelli, Guido and Ball, Richard D. and Forte, Stefano, Nucl. Phys. **B799**, 199 (2008).
- [60] Altarelli, Guido and Ball, Richard D. and Forte, Stefano, *Structure Function Resummation in small-x QCD*. Preprint 0802.0968, 2007.
- [61] Salam, G. P., JHEP **07**, 019 (1998).
- [62] Ciafaloni, M. and Colferai, D., Phys. Lett. **B452**, 372 (1999).
- [63] Ciafaloni, M. and Colferai, D. and Salam, G. P., Phys. Rev. **D60**, 114036 (1999).
- [64] Ciafaloni, Marcello and Colferai, Dimitri and Salam, Gavin P., JHEP **07**, 054 (2000).
- [65] Ciafaloni, M. and Colferai, D., JHEP **09**, 069 (2005).
- [66] Ciafaloni, M. and Colferai, D. and Salam, G. P. and Stasto, A. M., Phys. Lett. **B635**, 320 (2006).
- [67] Ciafaloni, M. and Colferai, D. and Salam, G. P. and Stasto, A. M., JHEP **08**, 046 (2007).
- [68] Thorne, Robert S., Phys. Rev. **D60**, 054031 (1999).
- [69] Thorne, R. S., Nucl. Phys. Proc. Suppl. **79**, 210 (1999).
- [70] Thorne, Robert S., Phys. Lett. **B474**, 372 (2000).
- [71] Thorne, Robert S., Phys. Rev. **D64**, 074005 (2001).
- [72] White, C. D. and Thorne, R. S., Phys. Rev. **D74**, 014002 (2006).
- [73] White, C. D. and Thorne, R. S., Phys. Rev. **D75**, 034005 (2007).

- [74] Ball, Richard D. and Forte, Stefano, Phys. Lett. **B465**, 271 (1999).
- [75] Altarelli, Guido and Ball, Richard D. and Forte, Stefano, Nucl. Phys. **B599**, 383 (2001).
- [76] Altarelli, Guido and Ball, Richard D. and Forte, Stefano, *An improved splitting function for small x evolution*. Preprint hep-ph/0310016, 2003.
- [77] Altarelli, Guido and Ball, Richard D. and Forte, Stefano, Nucl. Phys. Proc. Suppl. **135**, 163 (2004).
- [78] Ball, Richard D. and Forte, Stefano, Phys. Lett. **B405**, 317 (1997).
- [79] Lipatov, L., Sov. Phys. JETP **5**, 5 (1986).
- [80] Ball, R. D. and Ellis, R. Keith, JHEP **05**, 053 (2001).
- [81] Andersson, Bo and Gustafson, G. and Kharraziha, H. and Samuelsson, J., Z. Phys. **C71**, 613 (1996).
- [82] Kwiecinski, J. and Martin, Alan D. and Sutton, P. J., Z. Phys. **C71**, 585 (1996).
- [83] Kwiecinski, J. and Martin, Alan D. and Stasto, A. M., Phys. Rev. **D56**, 3991 (1997).
- [84] Collins, John C. and Kwiecinski, J., Nucl. Phys. **B316**, 307 (1989).
- [85] White, C. D. and Thorne, R. S., Eur. Phys. J. **C45**, 179 (2006).
- [86] Abbott, B. and others, Phys. Rev. Lett. **86**, 1707 (2001).
- [87] Affolder, T. and others, Phys. Rev. **D64**, 032001 (2001).
- [88] Adloff, C. and others, Eur. Phys. J. **C19**, 269 (2001).
- [89] Adloff, C. and others, Eur. Phys. J. **C21**, 33 (2001).
- [90] Breitweg, J. and others, Eur. Phys. J. **C7**, 609 (1999).
- [91] Chekanov, S. and others, Eur. Phys. J. **C21**, 443 (2001).
- [92] Martin, A. D. and Stirling, W. J. and Thorne, R. S., Phys. Lett. **B635**, 305 (2006).
- [93] Thorne, R. S., Phys. Rev. **D73**, 054019 (2006).
- [94] Aaron, F. D. and others, Phys. Lett. **B665**, 139 (2008).
- [95] Martin, A. D. and Stirling, W. J. and Thorne, R. S. and Watt, G., Phys. Lett. **B652**, 292 (2007).
- [96] Ciafaloni, Marcello, Phys. Lett. **B356**, 74 (1995).
- [97] Diemoz, M. and Ferroni, F. and Longo, E. and Martinelli, G., Z. Phys. **C39**, 21 (1988).
- [98] Ball, Richard D. and Forte, Stefano, Phys. Lett. **B359**, 362 (1995).
- [99] R. P. Feynman, *Photon-Hadron Interactions*. Benjamin, New York, 1972.
- [100] Bjorken, J.D., Lecture Notes in Physics, **56**, Springer, Berlin (1976).
- [101] Kuraev, E.A. and Lipatov, L.N. and Fadin, V.S., Sov. Phys. JETP **45**, 199 (1977).
- [102] V. N. Gribov and L. N. Lipatov, Sov. J. Nucl. Phys. **15**, 438 (1972).
- [103] V. N. Gribov and L. N. Lipatov, Sov. J. Nucl. Phys. **15**, 675 (1972).
- [104] G. Altarelli and G. Parisi, Nucl. Phys. **B 126**, 298 (1977).

- [105] Yu. L. Dokshitzer, Sov. Phys. JETP **46**, 641 (1977).
- [106] Gribov, L.V. and Levin, E.M. and Ryskin, M.G., Phys. Rept. **100**, 1 (1983).
- [107] Mueller, A.H., Nucl. Phys. **B558**, 285 (1999).
- [108] Iancu, E. and Venugopalan, R., *The color glass condensate and high energy scattering in QCD*. Preprint hep-ph/0303204, 2003.
- [109] Balitsky, I., Nucl. Phys. **B463**, 99 (1996).
- [110] Kovchegov, Yu.V., Phys. Rev. **D61**, 074018 (2000).
- [111] Stasto, A. M. and Golec-Biernat, Krzysztof J. and Kwiecinski, J., Phys. Rev. Lett. **86**, 596 (2001).
- [112] Munier, S. and Peschanski, R., Phys. Rev. **D69**, 034008 (2004).
- [113] Gelis, F. and Peschanski, Robert B. and Soyez, G. and Schoeffel, L., Phys. Lett. **B647**, 376 (2007).
- [114] Breitweg, J. and others, Phys. Lett. **B487**, 273 (2000).
- [115] Chekanov, S. and others, Phys. Rev. **D70**, 052001 (2004).
- [116] Arneodo, M. and others, Nucl. Phys. **B483**, 3 (1997).
- [117] Adams, M. R. and others, Phys. Rev. **D54**, 3006 (1996).
- [118] Beuf, G. and Peschanski, R. and Royon, C. and Salek, D., *Systematic Analysis of Scaling Properties in Deep Inelastic Scattering*. Preprint arXiv:0803.2186 [hep-ph], 2008.
- [119] Aaron, F. D. and others, Phys. Lett. **B659**, 796 (2008).
- [120] Aktas, A. and others, Eur. Phys. J. **C44**, 1 (2005).
- [121] Aktas, A. and others, Eur. Phys. J. **C48**, 715 (2006).
- [122] Chekanov, S. and others, Nucl. Phys. **B713**, 3 (2005).
- [123] Chekanov, S. and others, Eur. Phys. J. **C38**, 43 (2004).
- [124] Chekanov, S. and others, Nucl. Phys. **B718**, 3 (2005).
- [125] Aktas, A. and others, Eur. Phys. J. **C46**, 585 (2006).
- [126] Adloff, C. and others, Eur. Phys. J. **C13**, 371 (2000).
- [127] Adloff, C. and others, Z. Phys. **C72**, 593 (1996).
- [128] Adloff, C. and others, Phys. Lett. **B528**, 199 (2002).
- [129] Breitweg, J. and others, Phys. Lett. **B407**, 402 (1997).
- [130] Aubert, J. J. and others, Nucl. Phys. **B213**, 31 (1983).
- [131] Nadolsky, Pavel M. and others, Phys. Rev. **D78**, 013004 (2008).
- [132] Martin, A. D. and Roberts, R. G. and Stirling, W. J. and Thorne, R. S., Phys. Lett. **B604**, 61 (2004).
- [133] Gluck, M. and Reya, E. and Vogt, A., Eur. Phys. J. **C5**, 461 (1998).
- [134] Beuf, G., Royon, C. and Salek, D., to appear.
- [135] Iancu, E. and Itakura, K. and McLerran, L., Nucl. Phys. **A708**, 327 (2002).

- [136] Mueller, A. H. and Triantafyllopoulos, D. N., Nucl. Phys. **B640**, 331 (2002).
- [137] Gardi, E. and Kuokkanen, J. and Rummukainen, K. and Weigert, H., Nucl. Phys. **A784**, 282 (2007).
- [138] Albacete, Javier L. and Kovchegov, Yuri V., Phys. Rev. **D75**, 125021 (2007).
- [139] Beuf, G., *An alternative scaling solution for high-energy qcd saturation with running coupling*. Preprint arXiv:0803.2167 [hep-ph], 2008.
- [140] Kwiecinski, J. and Stasto, A. M., Phys. Rev. **D66**, 014013 (2002).
- [141] Caola, F. and Forte, S., Phys. Rev. Lett. **101**, 022001 (2008).
- [142] Del Debbio, Luigi and Forte, Stefano and Latorre, Jose I. and Piccione, Andrea and Rojo, Joan, JHEP **03**, 080 (2005).
- [143] Bartels, J. and Golec-Biernat, Krzysztof J. and Kowalski, H., Phys. Rev. **D66**, 014001 (2002).
- [144] J. Bartels, K. Golec-Biernat and L. Motyka, *in preparation*.
- [145] L. Motyka, *Higher twists from the saturation model*.
Talk at the 4th HERA and the LHC workshop, CERN, 26–30 May 2008,
<http://indico.cern.ch/conferenceDisplay.py?confId=27458>.
- [146] Bartels, Jochen and Golec-Biernat, Krzysztof J. and Peters, Krisztian, Eur. Phys. J. **C17**, 121 (2000).
- [147] Ellis, R. Keith and Furmanski, W. and Petronzio, R., Nucl. Phys. **B212**, 29 (1983).
- [148] Bukhvostov, A. P. and Frolov, G. V. and Lipatov, L. N. and Kuraev, E. A., Nucl. Phys. **B258**, 601 (1985).
- [149] Bartels, Jochen and Ryskin, M. G., Z. Phys. **C60**, 751 (1993).
- [150] Bartels, Jochen and Ryskin, M. G., Z. Phys. **C62**, 425 (1994).
- [151] Golec-Biernat, Krzysztof J. and Wusthoff, M., Phys. Rev. **D59**, 014017 (1999).
- [152] Golec-Biernat, Krzysztof J. and Wusthoff, M., Phys. Rev. **D60**, 114023 (1999).
- [153] Giele, Walter T. and Keller, Stephane, Phys. Rev. **D58**, 094023 (1998).
- [154] Giele, Walter T. and Keller, Stephane A. and Kosower, David A. (2001).
- [155] Ball, Richard D. and others, Nucl. Phys. **B809**, 1 (2009).
- [156] Watt, G. and Martin, A. D. and Stirling, W. J. and Thorne, R. S., *Recent Progress in Global PDF Analysis*. Preprint 0806.4890, 2008.
- [157] Adloff, C. and others, Eur. Phys. J. **C13**, 609 (2000).
- [158] Giele, W. and others, *The QCD/SM working group: Summary report*. Preprint hep-ph/0204316, 2002.
- [159] Arneodo, M. and others, Nucl. Phys. **B487**, 3 (1997).
- [160] Benvenuti, A. C. and others, Phys. Lett. **B223**, 485 (1989).
- [161] Badelek, B. and Kwiecinski, J., Phys. Rev. **D50**, 4 (1994).
- [162] Vargas Trevino, Andrea del Rocio, *Measurement of the inclusive e p scattering cross section at low Q**2 and x at HERA*. Prepared for 15th International Workshop on Deep-Inelastic Scattering and Related Subjects (DIS2007), Munich, Germany, 16-20 Apr 2007.

- [163] M. Botje, *Qcdnum16.12*. Available from <http://www.nikhef.nl/h24/qcdnum/>.
- [164] Martin, A. D. and Roberts, R. G. and Stirling, W. J. and Thorne, R. S., *Eur. Phys. J.* **C28**, 455 (2003).
- [165] Forte, Stefano and Garrido, Lluís and Latorre, Jose I. and Piccione, Andrea, *JHEP* **05**, 062 (2002).
- [166] Del Debbio, Luigi and Forte, Stefano and Latorre, Jose I. and Piccione, Andrea and Rojo, Joan, *JHEP* **03**, 039 (2007).
- [167] Amsler, C. and others, *Phys. Lett.* **B667**, 1 (2008).
- [168] A.D. Martin et al, *Eur. Phys.J C* **23**, 73 (2002).
- [169] J. Pumplin, H. L. Lai and W. K. Tung, *Phys. Rev.* **D 75**, 054029 (2007).
- [170] ZEUS Coll., S. Chekanov et al., *Eur. Phys. J. C* **42**, 1 (2005).
- [171] A.M. Cooper-Sarkar, *Phys. Rev D* **67**, 012007 (2003).
- [172] ZEUS and H1 Collaborations, *Combination of h1 and zeus deep inelastic e+- p scattering cross sections*. Preprint ZEUS-prel-07-036, H1prelim-07-007.
- [173] C. Pascaud and F. Zomer, *Qcd analysis from the proton structure function f2 measurement: Issues on fitting, statistical and systematic errors*. Preprint LAL-95-05, 1995.
- [174] C. Callan and D. Gross, *Phys. Rev. Lett.* **22**, 156 (1969).
- [175] A. Zee, F. Wilczek and S. B. Treiman, *Phys. Rev.* **D 10**, 2881 (1974);
G. Altarelli and G. Martinelli, *Phys. Lett.* **B 76**, 89 (1978).
- [176] L. N. Lipatov, *Sov. J. Nucl. Phys.* **20**, 94 (1975).
- [177] ZEUS Coll., S. Chekanov et al., in *EPS 2003 conference, Aachen*. 2003.
- [178] H1 Coll., C. Adloff et al., *Phys. Lett.* **B 393**, 452 (1997).
- [179] A. Vargas Trevino, *Measurement of the Inclusive ep Scattering Cross Section at low Q² and x at HERA*, in *Proceedings of the 15th International Workshop on Deep-Inelastic Scattering*. 2007.
- [180] T. Lastovicka, *Eur. Phys. J. C* **24**, 529 (2002).
- [181] H1 Coll., F. D. Aaron et al., *Phys. Lett.* **B 665**, 139 (2008).
- [182] A. D. Martin, W. J. Stirling, R. S. Thorne and G. Watt, *Phys. Lett.* **B 652**, 292 (2007).
- [183] Up to Date Performance of the ATLAS, CMS and LHCb Detectors and further detailed references can be found on the corresponding homepages <http://atlas.web.cern.ch/Atlas/index.html>,
<http://cmsinfo.cern.ch/Welcome.html/> and <http://lhcb.web.cern.ch/lhcb/>.
- [184] W. Herr and B. Muratori, *Concept of luminosity*. Proceedings CAS2003,
<http://doc.cern.ch/yellowrep/2006/p361.pdf>CERN-2006-002 p. 361.
- [185] H. Burkhardt and P. Grafstrom, *Absolute luminosity from machine parameters*. 2007.
CERN-LHC-PROJECT-Report-1019 and <http://cdsweb.cern.ch/record/1056691>.
- [186] Budnev, V. M. and Ginzburg, I. F. and Meledin, G. V. and Serbo, V. G., *Nucl. Phys.* **B63**, 519 (1973).
- [187] Khoze, Valery A. and Martin, Alan D. and Orava, R. and Ryskin, M. G., *Eur. Phys. J.* **C19**, 313 (2001).
- [188] Acosta, Darin E. and others, *Phys. Rev. Lett.* **94**, 091803 (2005).

- [189] Bellavance, Angela M., *W/Z production cross sections and asymmetries at $E(CM) = 2\text{-TeV}$* . Preprint hep-ex/0506025, 2005.
- [190] M. Dittmar, F. Pauss and D. Zurcher, Phys. Rev. **D56**, 7284 (1997).
- [191] Pinfeld, J., *Plans for the very forward region of ATLAS: The lucid luminosity monitor*. Prepared for 9th ICATPP Conference on Astroparticle, Particle, Space Physics, Detectors and Medical Physics Applications, Villa Erba, Como, Italy, 17-21 Oct 2005.
- [192] Anelli, G. and others, JINST **3**, S08007 (2008).
- [193] LHCb Technical Proposal, CERN-LHCC-98-004.
- [194] LHCb Technical Design Report 9 *LHCb Reoptimized Detector*, CERN-LHCC-2003-030.
- [195] Besson, N. and Boonekamp, M. and Klinkby, E. and Petersen, T. and Mehlhase, S., Eur. Phys. J. **C57**, 627 (2008).
- [196] See CMS Collaboration CMS PAS EWK-08-005 for Electrons and CMS PAS 2007/002 for Muons.
- [197] See LHCb Technical Design Report 10, *LHCb Trigger System*, CERN-LHCC-2003-031.
- [198] H. Schmickler, *How to measure beam intensity ?*
<http://indico.cern.ch/getFile.py/access?contribId=s1t18&resId=1&materialId=1&confId=a053945Talk>
given to Atlas 27 June 2005.
- [199] S. Van der Meer, *Calibration of the effective beam height in the isr.*
<http://doc.cern.ch/archive/electronic/kek-scan//196800064.pdf>CERN-ISR-PO-.
- [200] K. Potter, *Luminosity measurements and calculations*. CAS 1992, CERN yellow report,
<http://doc.cern.ch/yellowrep/1994/94-01/p117.pdf>. 117 ff.
- [201] G. Carboni *et al.*, Nucl. Phys. **B254**, 697 (1985).
- [202] Ferro-Luzzi, M., Nucl. Instrum. Meth. **A553**, 388 (2005).
- [203] The CMS Approach using Specialized High Rate Detectors is Described in the Talk of V.Halyo during the HERA-LHC Workshop “standard candles”.
- [204] The Presentations of the “standard candle” session during the HERA LHC Workshop in May 2008 can be found at:
http://indico.cern.ch/conferenceOtherViews.py?view=cdsagenda_olist&confId=27458#18..
- [205] Achard, P. and others, Phys. Lett. **B585**, 53 (2004).
- [206] Shamov, A. G. and Telnov, Valery I., Nucl. Instrum. Meth. **A494**, 51 (2002).
- [207] More Details about the LHCb Approach using $pp \rightarrow pp^{+-}$, are given in the talk of J. Anderson at the HERA-LHC Workshop “standard candles”.
- [208] C Anastasiou, L. J. Dixon, K. Melnikov, and F. Petriello, Phys. Rev. **D69**, 094008 (2004).
- [209] N. E. Adam, V. Halyo, S. A. Yost, JHEP **05** (2008).
- [210] N. E. Adam, V. Halyo, S. Yost W. Zhu, JHEP **09**, 13 (2008).
- [211] LHCb Technical Design Report 10, *LHCb Trigger System*, CERN-LHCC-2003-031.
- [212] More details about the LHCb approach using $\sigma_Z \cdot Br(Z \rightarrow \mu^+ \mu^-)$, are given in the talk by J. Anderson at the HERA-LHC Workshop “standard candles”..

- [213] McNulty, R., *Potential PDF sensitivity at LHCb*. Preprint 0810.2550, 2008.
- [214] The web page of the PDF4LHC forum can be found at <http://www.hep.ucl.ac.uk/pdf4lh/>.
- [215] Sherstnev, A. and Thorne, R. S., *Different PDF approximations useful for LO Monte Carlo generators*. Preprint 0807.2132, 2008.